The Role and Usage of Libration Point Orbits in the Earth – Moon System

Elisa Maria Alessi

ADVERTIMENT. La consulta d'aquesta tesi queda condicionada a l'acceptació de les següents condicions d'ús: La difusió d'aquesta tesi per mitjà del servei TDX (www.tesisenxarxa.net) ha estat autoritzada pels titulars dels drets de propietat intel·lectual únicament per a usos privats emmarcats en activitats d'investigació i docència. No s'autoritza la seva reproducció amb finalitats de lucre ni la seva difusió i posada a disposició des d'un lloc aliè al servei TDX. No s'autoritza la presentació del seu contingut en una finestra o marc aliè a TDX (framing). Aquesta reserva de drets afecta tant al resum de presentació de la tesi com als seus continguts. En la utilització o cita de parts de la tesi és obligat indicar el nom de la persona autora.

ADVERTENCIA. La consulta de esta tesis queda condicionada a la aceptación de las siguientes condiciones de uso: La difusión de esta tesis por medio del servicio TDR (www.tesisenred.net) ha sido autorizada por los titulares de los derechos de propiedad intelectual únicamente para usos privados enmarcados en actividades de investigación y docencia. No se autoriza su reproducción con finalidades de lucro ni su difusión y puesta a disposición desde un sitio ajeno al servicio TDR. No se autoriza la presentación de su contenido en una ventana o marco ajeno a TDR (framing). Esta reserva de derechos afecta tanto al resumen de presentación de la tesis como a sus contenidos. En la utilización o cita de partes de la tesis es obligado indicar el nombre de la persona autora.

WARNING. On having consulted this thesis you're accepting the following use conditions: Spreading this thesis by the TDX (www.tesisenxarxa.net) service has been authorized by the titular of the intellectual property rights only for private uses placed in investigation and teaching activities. Reproduction with lucrative aims is not authorized neither its spreading and availability from a site foreign to the TDX service. Introducing its content in a window or frame foreign to the TDX service is not authorized (framing). This rights affect to the presentation summary of the thesis as well as to its contents. In the using or citation of parts of the thesis it's obliged to indicate the name of the author.

The Role and Usage of Libration Point Orbits in the Earth – Moon System

Elisa Maria Alessi

Departament de Matemàtica Aplicada i Anàlisi
Universitat de Barcelona

Programa de doctorat de Matemàtiques
Bienni 2005–2007

Memòria presentada per aspirar
al grau de Doctor en Matemàtiques
per la Universitat de Barcelona

Certifiquem que la present memòria
ha estat realitzada per Elisa Maria Alessi
i dirigida per nosaltres.

Barcelona, 7 de juliol de 2010

Gerard Gómez i Muntané

Josep Joaquim Masdemont i Soler

CONTENTS

Abstract

In this dissertation we apply the Circular Restricted Three – Body Problem to the Earth – Moon system both for astrodynamical and astronomical purposes. We take advantage of the hyperbolic invariant manifolds associated with the central invariant manifold of the collinear equilibrium point either L_1 and L_2 to construct transfers from either Moon and Earth to a nominal libration point orbit and to study some tracks leading to collisional events on the Moon. Also, we develop an effective methodology for the refinement of such trajectories into a more realistic vector field and we show the consequences of omitting the Sun. Throughout the work, we exploit the tools of Dynamical Systems Theory and optimal control strategies.

Resum

L'objectiu d'aquest treball és mostrar la utilitat de l'explotació del Problema Circular Restringit dels Tres Cossos (CR3BP) pel sistema Terra – Lluna. Aquest sistema dinàmic considera el moviment d'una partícula amb massa negligible sota l'atracció gravitatòria de Terra i Lluna i pot ser usat pel disseny de missions espacials a la nova era d'exploració lunar, així com per simular el comportament d'asteroides i cometes que s'apropen a la Terra. Les eines de la Teoria dels Sistemes Dinàmics serveixen per identificar els objectes invariants que existeixen dins de l'aproximació definida pel CR3BP i entendre'n la seva funció segons el tipus d'aplicació considerada.

Els cinc punts d'equilibri, o de libració, del CR3BP que apareixen al sistema de referència giratori, juguen un paper fonamental: la força gravitatòria i les degudes al sistema no inercial es compensen de tal manera que una partícula situada en aquests punts pot romandre aturada, almenys en teoria, per un temps infinit. Ens centrarem en dos punts de libració col·lineals, L_1 i L_2, que estan situats sobre l'eix que uneix els primàris (Terra i Lluna) prop del més petit (Lluna). El seu comportament és inestable i qualsevol petita pertorbació és capaç d'allunyar una partícula del punt d'equilibri en un temps molt curt.

Per raons tant teòriques com pràctiques, també convé tenir en compte les varietats invariants centrals i hiperbòliques que hi ha a l'entorn de L_1 i L_2. La varietat invariant central està ocupada per diversos tipus d'òrbites periòdiques i quasi-periòdiques, que poden ser concebudes com solucions d'estacionament per a un vehicle espacial. Qualsevol d'aquestes òrbites té associada una varietat estable i una d'inestable, que es corresponen amb la component sella associada al punt d'equilibri, i serveixen com a canals per arribar lluny o prop de les òrbites centrals per $t \geq 0$. Farem ús de la dinàmica associada a aquestes varietats per a la construcció de transferències des de la Terra i la Lluna a una òrbita de libració (LPO) i per investigar alguns camins que podrien guiar asteroides que impacten amb la Lluna.

En el primer capítol de la tesi, expliquem les propietats bàsiques del CR3BP i com calcular les òrbites periòdiques i quasi-periòdiques, juntament amb les seves corresponents varietats invariants hiperbòliques. A més de l'aproximació lineal, usarem abastament desenvolupaments en sèrie de Lindstedt–Poincaré, que produeixen solucions amb un alt nivell de precisió. La geometria de les varietats invariants estable i inestable és crucial per a les nostres aplicacions, especialment per a la part astronòmica del treball. També mostrarem com les varietats invariants hiperbòliques associades a les òrbites periòdiques de Lyapunov plana i vertical delimiten les fronteres d'energia per a una partícula que es mou dins de la varietat invariant hiperbòlica associada a tota la varietat invariant

central de L_1 o L_2.

Al mateix capítol, s'introdueixen dos sistemes dinàmics més elaborats: el Problema Restringit Bicircular dels Quatre Cossos (BR4BP) i el Problema Restringit de n Cossos (RnBP). Els usarem per analitzar l'efecte del Sol i d'altres planetes en les trajectòries que verifiquen les equacions del CR3BP.

Després d'aquest capítol introductori, la tesi es divideix en dues parts: en la primera s'estudien diferents tipus de transferències que una nau espacial pot realitzar i a l'altra les òrbites que poden produir la formació de cràters d'impacte a la Lluna.

Pel que fa a la primera qüestió, quaranta anys després del primer pas d'un home a la Lluna, actualment som testimonis d'un debat, més viu que mai, sobre un possible retorn. No només la NASA, sinò també la India, la Xina i el Japó han dissenyat missions no tripulades, que molt recentment han acabat de fer (o estan a punt de fer-ho) observacions al voltant de la Lluna a la recerca d'aigua, de provar noves tecnologies i d'obtenir una caracterització detallada dels satèl·lits pensant en una instal·lació humana en el futur. A més, les noves companyies de turisme espacial estan planejant estendre la seva potencialitat, oferint viatges lunars.

En aquest context, l'entorn de L_1, situat entre la Terra i la Lluna, sembla ser el lloc més apropiat per posar una estació espacial, que pot servir, per exemple, per obres de construcció i reparació d'una base lunar o de satèl·lits que li donguin servei. D'altra banda, L_2 seria útil per observar i/o controlar la cara oculta de la Lluna.

En el passat, diversos autors han proposat missions basades en LPOs del sistema Terra – Lluna. Les referències es remunten als anys 60, amb les obres de Colombo (1961), Farquhar (1966) i Conley (1968), i arriben fins al dia d'avui (veure, per exemple, Lo, Ross (2001); Carpenter et al. (2004); Hill et al. (2005); Howell, Ozimek (2007)). No obstant això, fins ara encara no s'ha fet cap explotació pràctica, tot i que tant les solucions Keplerianes clàssiques com les de baix impuls són del tot operatives.

De tota manera, les òrbites que anem a estudiar també poden ser útils per altres tipus d'exploracions del Sistema Solar, que actualment també desperten molt d'interès, com ara les relacionades amb l'exploració de Mart o dels asteroides. En particular, una estació espacial al sistema Terra – Lluna podria ser molt adequada (Lo, Ross, 2001) per ampliar les finestres de llançament de les transferències interplanetàries, que normalment són molt estretes. D'altra banda, metodologies similars a les desenvolupades en la memòria es poden aplicar a diferents sistemes satèl·lit-planeta, com ara, les llunes galileanes de Júpiter.

En el capítol 2 s'utilitzen les varietats invariants estable i inestable, associades amb òrbites halo i de Lissajous al voltant dels punts d'equilibri L_1/L_2, per tal de connectar la superfície de la Lluna amb aquestes LPOs. Veurem que, gràcies a la dinàmica natural del problema, es poden usar aquestes transferències sense gairebé cap esforç energètic addicional.

En el capítol 3 s'estudia un tipus de transferència inversa a la considerada en el capítol anterior: ara partirem d'una òrbita nominal al voltant de la Terra per arribar a una LPO al voltant de L_1 o L_2. Aquesta situació és una mica més complicada perquè requereix dues maniobres, una per sortir de l'òrbita terrestre i una altra per inserir-se en la varietat invariant estable associada amb la LPO considerada. Mentre que el cost de la primera maniobra sols es pot reduir a partir d'altures molt grans, el cost de la segona varia, per les transferències a L_1, en funció de la distància entre la Terra i la varietat, mentre que per L_2 depèn del temps que s'ha de passar a la varietat.

En el capítol 4 ens preguntem com les solucions de referència calculades d'acord amb l'aproximació CR3BP poden canviar quan s'afegeixen diferents forces al model dinàmic. Descriurem dos possibles enfocaments que poden aplicar-se per fer front a aquest problema, destacant els seus punts forts i febles. En particular, definirem una estratègia de control òptim pel refinament de les òrbites i es posarà a prova la seva eficàcia en comparació amb un procediment de tir múltiple. D'entrada, no s'estableix cap concidió de continuïtat com a lligam per l'optimització. Mitjançant un procediment de correcció diferencial s'estableix la continuïtat en posicions, mentre que les discontinuïtats en velocitat es minimitzen mitjançant una funció de cost adequada. Els resultats obtinguts mostren que també al marc Terra – Lluna el CR3BP dóna solucions properes a les que s'utilitzaran en la realitat, tot i que el CR3BP omet la influència del Sol.

A la segona part de la tesi (capítol 5), investiguem la col·lisió d'asteroides amb la Lluna. Aquest fenòmen té lloc contínuament a tots els planetes rocosos i els satèl·lits del Sistema Solar, com es pot deduir dels cràters que han modelat les seves superfícies. A la web es poden trobar imatges fantàstiques que ilustren aquest fenòmen.

Hi ha molta literatura dedicada al procés de formació de cràters, ja que proporciona informació sobre la cronologia del cos objectiu, sobre els asteroides i, per tant, sobre l'evolució del Sistema Solar, no només en termes dinàmics, sinó també en termes astronòmics i geològics. El nostre objectiu és lluny de derivar una comprensió completa d'aquest tipus d'esdeveniments, però estem interessats en el desenvolupament d'una metodologia diferent que pot ajudar en aquesta recerca.

Considerem el paper exercit per les trajectòries de baixa energia en la creació de cràters lunars d'impacte, preguntant-nos si, per a certs rangs d'energies, produeixen una distribució específica de col·lisions sobre la superfície lunar.

Simulem el comportament de les trajectòries de trànsit situades a l'interior del tub dinàmic estable que s'acosta a l'entorn de L_2. Com que el bombardeig més intens a la Lluna va passar entre 4 i 3.8 Ganys, analitzarem diversos valors per la distància Terra – Lluna. A més, veurem si l'elecció de la distribució de les condicions inicials afecta al resultat final.

Veurem que, si per les inclinacions inicials respecte al pla orbital Terra – Lluna no seleccionem cap interval especial, la major part dels impactes tenen lloc en el rang de longituds $(80°W, 180°W)$, i la densitat de probabilitat més alta es concentra en l'àpex lunar, és a dir, a l'entorn de $(90°W, 0°)$.

Si sumem la força gravitatòria exercida pel Sol sobre la partícula a les de la Terra i la Lluna, detectem una disminució en la quantitat total de col·lisions, variant el percentatge segons la posició relativa del Sol en l'època inicial.

Finalment, a les conclusions es fa un resum del resultats obtinguts i s'esbossen algunes idees futures.

Preface

The objective of this work is to show the effectiveness of the exploitation of the Circular Restricted Three – Body Problem (CR3BP) in the Earth – Moon framework. Such dynamical model considers the motion of a massless particle under the gravitational attraction of Earth and Moon and can be used either to design missions in the new era of lunar exploration and simulate the behavior of Solar System minor bodies that get close to the Earth. The tools of the Dynamical Systems Theory help to identify the invariant objects which exist within the CR3BP approximation and to understand their function according to the applications we have in mind.

A fundamental role is played by the five equilibrium, or libration, points that appear in the rotating reference system: there the gravitational force and the ones due to the non-inertial frame compensate each other in such a way that the small body can stand, at least theoretically, for an infinite long time. We will focus on two, L_1 and L_2, collinear libration points, which are those lying on the axis joining the primaries and whose behavior is unstable. This means that any negligible perturbation is capable of bringing the particle far away the equilibrium point in a very short time.

For practical and theoretical reasons, it is worth to take into account the central and hyperbolic invariant manifolds, which exist in the neighborhood of either L_1 and L_2. Various types of periodic and quasi-periodic orbits, that can be conceived as station locations for a spacecraft, occupy the central invariant manifold. A stable and an unstable invariant manifold are associated with any of these orbits: they arise from the saddle component associated with the equilibrium point and serve as channels to get far or close to the central orbits for $t \geq 0$. We will make use of the corresponding dynamics to construct transfers from either Earth and Moon to a libration point orbit (LPO) and to investigate some paths that might guide asteroids impacting onto the Moon.

In the first chapter of the dissertation, we will explain the basics properties of the CR3BP and how to compute periodic and quasi-periodic orbits along with their associated hyperbolic invariant manifolds. Apart from a linear approximation, we will exploit Lindstedt–Poincaré series expansions, which provide initial conditions characterized by a high accuracy. The geometry of the stable and the unstable invariant manifolds is crucial for our applications, especially for the astronomical part of the work. We will also show how the hyperbolic invariant manifolds associated with planar and vertical Lyapunov periodic orbits act as energy boundaries for a particle which moves inside the hyperbolic invariant manifolds associated with the whole central invariant manifold of either L_1 or L_2.

In the same chapter, two more elaborate dynamical systems are introduced, the Bicircular Restricted Four – Body Problem (BR4BP) and the Restricted n – Body Problem (RnBP). We will take advantage of them to analyze the effect of the Sun and other planets on the trajectories satisfying the CR3BP equations of motion.

After this introductory chapter, the dissertation is divided in two main blocks: one concerning transfers that can be achieved by a spacecraft and the other regarding orbits that can yield the formation of impact craters on the surface of the Moon.

With respect to the former issue, forty years after the first step by a man on the Moon we are witnesses of a debate, active more than ever, on a possible return. Not just NASA, but also India, China and Japan have designed unmanned missions that very recently have completed (or are about to) observations around the Moon, looking for water, testing new technology and obtaining a detailed characterization of the satellite in view of a future human installation. Besides, the space tourism companies are planning to extend their potentiality by offering lunar trips.

In this context, the neighborhood of L_1, located between the two primaries, seems to be the most appropriate place to put a space hub, serving for instance as a construction and repair facility. On the other hand, L_2 would be profitable to monitor the lunar farside.

In the past, several authors have proposed missions based on LPOs in the Earth – Moon system, dating back to the 60's with the works of Colombo (1961), Farquhar (1966) and Conley (1968) up to the present day (see, for instance, Lo, Ross (2001); Carpenter et al. (2004); Hill et al. (2005); Howell, Ozimek (2007)). However, none practical exploitation has been seen so far, being either low-thrust and classical Keplerian solutions operational.

Anyway, the orbits we will investigate would be also useful if we consider other types of Solar System explorations that are now drawing much attention, e.g. in relation to Mars or a minor body. In particular, a Earth – Moon space station could be suitable if we mean to extend the usually narrow launch window (Lo, Ross, 2001) required for such interplanetary transfers. Moreover, similar methodologies to those developed here can be applied to different planet-satellite systems, as example in the Jupiter framework.

In Chapter 2, we will use the stable and the unstable invariant manifolds associated with either halo and Lissajous orbits around the L_1/L_2 equilibrium points in order to connect the surface of the Moon with such LPOs. We will see that almost no effort should be put to follow these transfers thanks to the natural dynamics we consider.

In Chapter 3, we will study the counter-case, that is, how to depart from a nominal orbit around the Earth and arrive to a LPO either around L_1 or L_2. This situation is slightly more complicated because it requires two maneuvers, one to leave the Low Earth Orbit and another to insert into the stable invariant manifold associated with the given LPO. While the first can be reduced only starting from high altitudes, the cost of the second one varies depending on the distance existing between the Earth and the manifold for L_1 transfers, on the time to be spent on the manifold for L_2.

In Chapter 4, we will wonder how the above reference solutions and further ones can change whenever different forces are added to the dynamical model. We will describe two possible approaches that can be implemented to face this problem, highlighting their strong and weak specific points. In particular, we will define an optimal control strategy for the refinement of orbits and we will test its efficacy when compared with a multiple shooting procedure. The requirement of continuity is not set as a constraint for the optimization, rather is accomplished in position by a differential correction procedure and in velocity by defining an appropriate cost function. The results demonstrate that also in the Earth – Moon framework the CR3BP gives solutions which are quite close to the ones to be used in reality, though it omits the presence of the Sun.

In the second part of the work (Chapter 5) we will cope with the collision of asteroids onto the Moon. Such phenomenon takes place continuously on all the rocky planets and satellites populating the Solar System, as it can be inferred from the craters that moulded their surface. If one is interested, marvelous images are available on the web.

There exists a huge literature devoted to the cratering process, because it provides information on the chronology of the target body, on the impacting asteroids and thus on the Solar System evolution, not only in dynamical terms but also in astronomical and geological terms. Our aim is far from deriving a complete comprehension of this kind of events, but we are interested in supplying a different methodology that can aid in this way.

We will address the problem of the role played by low-energy trajectories in the creation of lunar impact craters, asking whether they produce a specific distribution of collisions, for instance on the farside of the Moon, when considering a particular range of energies.

We will simulate the behavior of transit trajectories lying inside the dynamical stable tube which approaches the neighborhood of L_2. Since the most intense bombardment on the Moon happened between 4 and 3.8 Gy ago, we will analyze several values for the Earth – Moon distance. Also, we will see if the choice of the dissemination of initial conditions can affect the final outcome.

It turns out that the most of the impacts occurs in the longitude range of $(80^\circ W, 180^\circ W)$ if we do not select any special interval of inclination with respect to the Earth – Moon orbital plane. The most likely case is focused on the apex of the lunar surface, that is, in the neighborhood of $(90^\circ W, 0^\circ)$.

If we sum up the gravitational force exerted by the Sun on the particle to the ones of Earth and Moon, we detect a decrease in the total amount of collisions, whose percentage varies according to the position of the Sun at the initial epoch.

Finally, in the Conclusions we will resume all the results achieved and outline some future directions.

DYNAMICAL MODELS AND INVARIANT MANIFOLDS

1

1.1 Introduction

The work we are going to present is established on the Circular Restricted Three – Body Problem (CR3BP). This dynamical model treats the motion of a pointless body with negligible mass that is affected by the gravitational forces exerted by two punctiform masses, Earth and Moon in our case.

It is well-known that the CR3BP, in a proper reference system, admits five equilibrium points and that central and hyperbolic invariant manifolds originate from those three which lie on the axis joining the two primaries. Both the astrodynamical and astronomical applications we will examine make an extensive usage of these invariant objects and thus they deserve here a detailed description. We will introduce their mathematical derivation, their behavior and the numerical tools we adopt for their computation.

On the other hand, we are aware that the influence of the Sun plays a significant role on the dynamics which takes place in the Earth – Moon framework. This is why we will review the outcome obtained with the CR3BP model by assuming more complicated vector fields.

In particular, the impact trajectories that can be responsible of the formation of part of the Moon's craters (see Chapter 5) are also investigated with the Bicircular Restricted Four – Body Problem (BR4BP). The main difference between the CR3BP and the BR4BP is that in the latter neither equilibrium points nor first integrals exist. Actually, it does not represent a realistic model of forces, in the sense that Earth, Moon and Sun do not follow the Newtonian law. Though it is a mathematical construction, the BR4BP is helpful to get an insight of the consequences that the presence of the Sun can take.

As we account only for gravitational forces and not for any other effect that can occur in the Solar System, the most comprehensive dynamical model we can adopt is the Restricted n – Body Problem (RnBP). In this case, the reference frame is inertial and we allow for all the planets, Moon and Sun to interact with the massless particle. In principle, we could also add the attractions furnished by other minor bodies, for instance the more massive asteroids, but for our purposes it is not needed. To make the orbits of the primaries as close as possible to the reality, we mutuate from the JPL ephemerides their position and velocity at each instant of time. We exploit the RnBP to refine (see Chapter 4) the transfers computed in Chapter 3. Two formulations are presented, one centered at the Solar System barycenter, the other at the Earth.

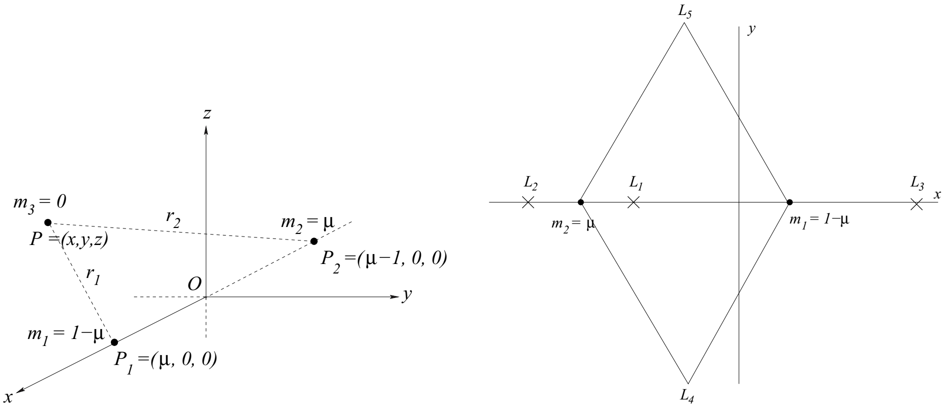

Figure 1.1: Left: the Circular Restricted Three-Body Problem in the synodical reference system with adimensional units. Right: the five equilibrium points associated with the problem.

1.2 The Circular Restricted Three – Body Problem

The Circular Restricted Three – Body Problem (Szebehely, 1967) studies the behavior of a particle P with infinitesimal mass m_3 moving under the gravitational attraction of two primaries P_1 and P_2, of masses m_1 and m_2, revolving around their center of mass on circular orbits.

To remove time from the equations of motion, it is convenient to introduce a synodical reference system $\{O, x, y, z\}$, which rotates around the $z-$axis with constant angular velocity ω equal to the mean motion n of the primaries. The origin of the reference frame is set at the barycenter of the system and the $x-$axis on the line joining the primaries, oriented in the direction of the largest primary. In this way we work with m_1 and m_2 fixed on the $x-$axis, as shown in Fig. 1.1.

The units are chosen to set the gravitational constant, the sum of the masses of the primaries, the distance between them and the modulus of the angular velocity of the rotating frame to be unitary. For the Earth – Moon system, the unit of distance equals 384400 km, the unit of velocity equals 1.02316 km/s and the dimensionless mass of the Moon is $\mu = \frac{m_2}{m_1+m_2} = 0.012150582$. With these reference system and units, the equations of motion can be written as

$$\begin{aligned}
\ddot{x} - 2\dot{y} &= \frac{\partial \Omega}{\partial x} = x - \frac{(1-\mu)}{r_1^3}(x-\mu) - \frac{\mu}{r_2^3}(x+1-\mu), \\
\ddot{y} + 2\dot{x} &= \frac{\partial \Omega}{\partial y} = y - \frac{(1-\mu)}{r_1^3}y - \frac{\mu}{r_2^3}y, \\
\ddot{z} &= \frac{\partial \Omega}{\partial z} = -\frac{(1-\mu)}{r_1^3}z - \frac{\mu}{r_2^3}z,
\end{aligned} \tag{1.1}$$

where

$$\Omega(x,y,z) = \frac{1}{2}(x^2+y^2) + \frac{1-\mu}{r_1} + \frac{\mu}{r_2} + \frac{1}{2}(1-\mu)\mu,$$

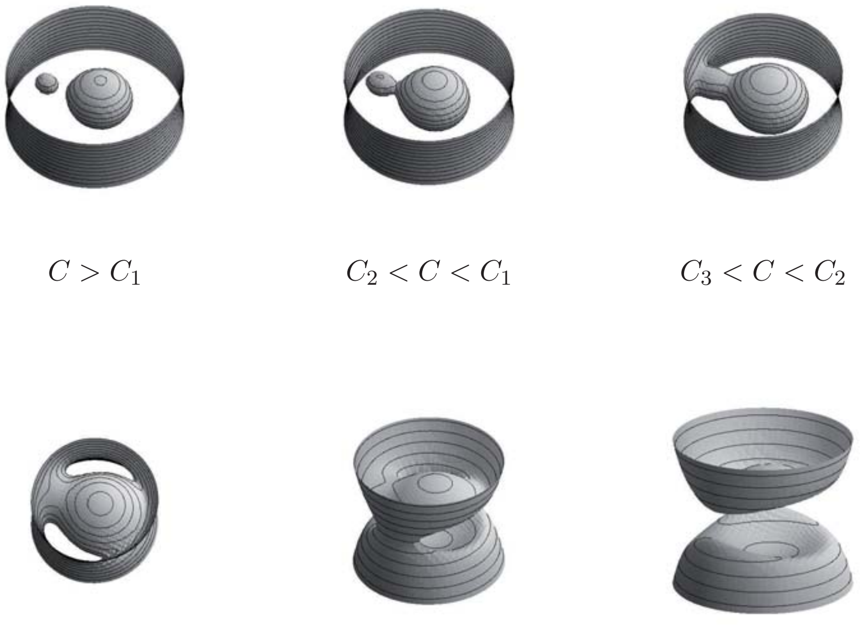

$C > C_1$ $C_2 < C < C_1$ $C_3 < C < C_2$

$C_4 < C < C_3$ $C < C_4$

Figure 1.2: Evolution of the zero-velocity surfaces with the Jacobi constant for $\mu > 0$. The case $C < C_4 = C_5$ is not displayed since the motion is allowed everywhere.

and $r_1 = [(x-\mu)^2 + y^2 + z^2]^{\frac{1}{2}}$ and $r_2 = [(x+1-\mu)^2 + y^2 + z^2]^{\frac{1}{2}}$ are the distances from P to P_1 and P_2, respectively.

System (1.1) has a first integral, the *Jacobi integral*, which is given by

$$2\Omega(x, y, z) - \left(\dot{x}^2 + \dot{y}^2 + \dot{z}^2\right) = C, \tag{1.2}$$

where C is the so called Jacobi constant.

The CR3BP admits a Hamiltonian formulation, in which the value of the Hamiltonian H is related to the one of the Jacobi constant by $C = -2H + \mu(1-\mu)$.

In the synodical reference system, there exist five equilibrium (or libration) points. Three of them, the *collinear* ones, are in the line joining the primaries and are usually denoted by L_1, L_2 and L_3. If x_{L_i} $(i = 1, 2, 3)$ denotes the abscissa of the three collinear points, we will assume that

$$x_{L_2} < \mu - 1 < x_{L_1} < \mu < x_{L_3}.$$

The other two equilibrium points, L_4 and L_5, the *triangular* ones, are in the plane of motion of the primaries and form an equilateral triangle with them. See Fig. 1.1.

If C_i $(i = 1, \ldots, 5)$ denotes the value of the Jacobi constant at the L_i equilibrium point, it holds that

$$C_1 > C_2 > C_3 > C_4 = C_5 = 3.$$

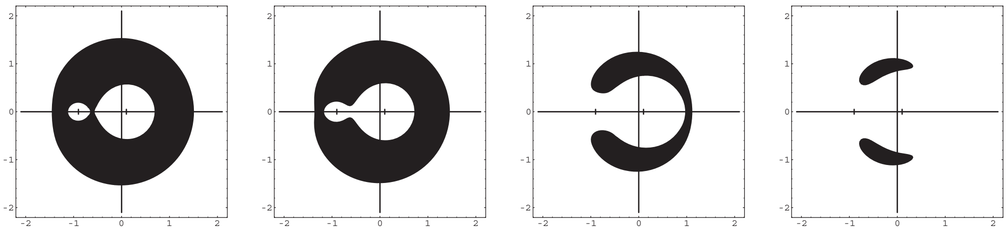

$C > C_1$ $\quad$ $C_2 < C < C_1$ $\quad$ $C_3 < C < C_2$ $\quad$ $C_4 < C < C_3$

Figure 1.3: Intersection of the zero-velocity surfaces with the $\{z = 0\}$ plane for $\mu > 0$. The motion is forbidden in the filled areas. The case $C < C_4 = C_5$ is not displayed since the motion is allowed everywhere. The tick marks on the horizontal axis show the position of the primaries: P_1 on the positive $x-$axis and P_2 on the negative $x-$axis.

Depending on the value of the Jacobi constant, it is possible to know where the particle can move in the configuration space. According to (1.2), the regions where the motion is forbidden are characterized by $2\Omega(x, y, z) - C < 0$ and their boundaries ($2\Omega(x, y, z) = C$) are the *zero-velocity surfaces.* For a given value of the mass parameter, there exist five different geometric configurations, four of them displayed in Figs. 1.2 and 1.3. The regions of allowed motion are also known as *Hill's regions.*

1.2.1 Dynamics around the Collinear Points

The collinear libration points behave, linearly, as the product of two centers by a saddle (Szebehely, 1967). To be precise, by performing a linearization around a given collinear point, we see that the motion in the vertical direction is uncoupled from the planar one and it is a harmonic oscillator with *vertical frequency* $\omega_v = \sqrt{c_2} > 0$, where

$$
\begin{aligned}
c_2 &= \frac{1}{\gamma_1^3}\left[\mu + (1-\mu)\frac{\gamma_1^3}{(1-\gamma_1)^3}\right], && \text{for } L_1,\\
c_2 &= \frac{1}{\gamma_2^3}\left[\mu + (1-\mu)\frac{\gamma_2^3}{(1+\gamma_2)^3}\right], && \text{for } L_2,\\
c_2 &= \frac{1}{\gamma_3^3}\left[(1-\mu) + \mu\frac{\gamma_3^3}{(1+\gamma_3)^3}\right], && \text{for } L_3,
\end{aligned}
$$

and γ_i $(i = 1, 2, 3)$ is the distance between L_i and the closest primary.

On the other hand, the planar motion is determined by the characteristic polynomial $p(\lambda)$ of the matrix

$$
J \cdot \mathrm{Hess}(H_2|_{z=p_z=0}) = \begin{pmatrix} 0 & 1 & 1 & 0 \\ -1 & 0 & 0 & 1 \\ 2c_2 & 0 & 0 & 1 \\ 0 & -c_2 & -1 & 0 \end{pmatrix}, \tag{1.3}
$$

where J is the canonical symplectic matrix and H_2 is the second order term of the Hamiltonian, expanded around L_i $(i = 1, 2, 3)$. An easy computation shows that

$$p(\lambda) = \lambda^4 + (2 - c_2)\lambda^2 + (1 + c_2 - 2c_2^2). \tag{1.4}$$

Introducing $\eta = \lambda^2$, the roots of $p(\lambda) = 0$ are given by

$$\begin{aligned} \eta_1 &= \frac{c_2 - 2 - \sqrt{9c_2^2 - 8c_2}}{2}, \\ \eta_2 &= \frac{c_2 - 2 + \sqrt{9c_2^2 - 8c_2}}{2}. \end{aligned} \tag{1.5}$$

So, according to the value of c_2, we have $\eta_1 < 0$ and $\eta_2 > 0$. We call $\omega_p = \sqrt{-\eta_1}$ the *planar frequency*.

This means that around a collinear point we deal with bounded orbits, which are due to the central part, and also with escape trajectories which depart exponentially from the neighborhood of the collinear point for $t \to \pm\infty$ and are due to the saddle component. The former kind of motion belongs to the *central invariant manifold* $\mathcal{W}^c(L_i)$, the latter to the *hyperbolic invariant manifolds* associated with the central invariant one. The hyperbolic manifolds consist, in particular, in one stable and one unstable, $\mathcal{W}^s(L_i)$ and $\mathcal{W}^u(L_i)$ respectively.

The Central Invariant Manifold

The center × center part generates a 4–dimensional center invariant manifold around each collinear equilibrium point, when considering all the energy levels. On a given energy level this is a 3–dimensional set filled with periodic and quasi-periodic solutions lying on invariant tori, plus some stochastic regions in between.

There exist families of periodic orbits which in limit have frequencies related to both centers: ω_p and ω_v. They are known as *planar Lyapunov family* and *vertical Lyapunov family* and their existence is ensured by the Lyapunov's center theorem, unless one of the frequencies is an integer multiple of the other (which only happens for a countable set of values of the mass ratio (Siegel, Moser, 1971)). See Fig. 1.4.

Halo orbits are 3–dimensional periodic orbits that show up at the first bifurcation of the planar Lyapunov family. In fact, there appear two families of halo orbits which are symmetrical with respect to the $\{z = 0\}$ plane. They are known as *north* and *south class* halo families or also *first class* and *second class* halo families. See Fig. 1.5.

Near the libration points we can also expect 2–dimensional tori, with basic frequencies that go to ω_p and ω_v when we approach the point. They are characterized by an harmonic motion in the $\{z = 0\}$ plane (the "in–plane component") and an uncoupled oscillation in $z-$direction (the "out–of–plane component") with different periods. See Fig. 1.9. The rigorous proof of the existence of these tori is more problematic. First, the basic frequencies at the collinear point can be too close to resonant. Furthermore, the frequencies change with their amplitudes and so, they go across resonances when the amplitudes are changed. This leads to a Cantor set of tori. The proof of the existence

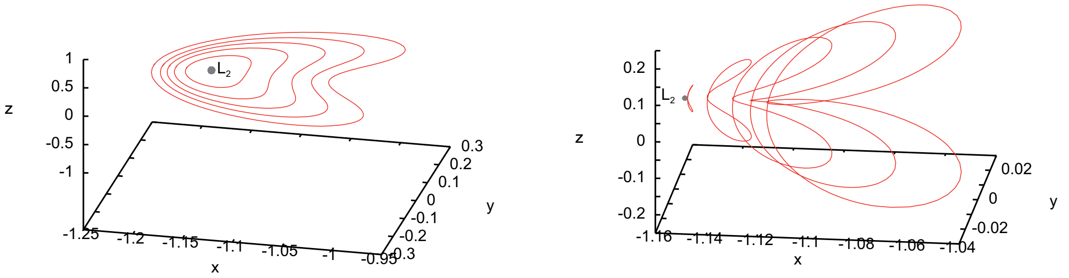

Figure 1.4: Examples of Lyapunov planar (left) and vertical (right) periodic orbits around the equilibrium point L_2 in the Earth – Moon system.

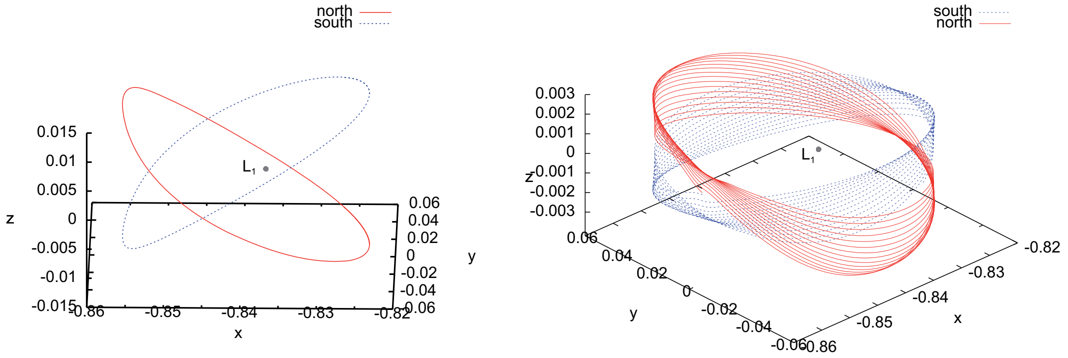

Figure 1.5: Examples of halo (left) and quasi-halo (right) orbits around the equilibrium point L_1 in the Earth – Moon system.

of these tori can be done following the lines of what is done in Jorba, Villanueva (1997) to show the persistence of low-dimensional tori under quasi-periodic perturbations.

There are also quasi-periodic solutions around the halo periodic orbits. They are known as *quasi-halo* orbits (Gómez, Masdemont, Simó, 1998) and one of their basic frequencies is the one of the halo orbit around which they move. See Fig. 1.5.

In Fig. 1.6, we represent the intersections of the different kinds of orbit with the $\{z = 0\}$ plane. For any energy level, the boundary of the plot is always a planar Lyapunov orbit and the fixed point in the center corresponds to the vertical one.

Apart from those just mentioned, there exist other families of orbits belonging to $\mathcal{W}^c(L_i)$, but Lyapunov, halo, Lissajous and quasi-halo are the most exploited ones. Throughout

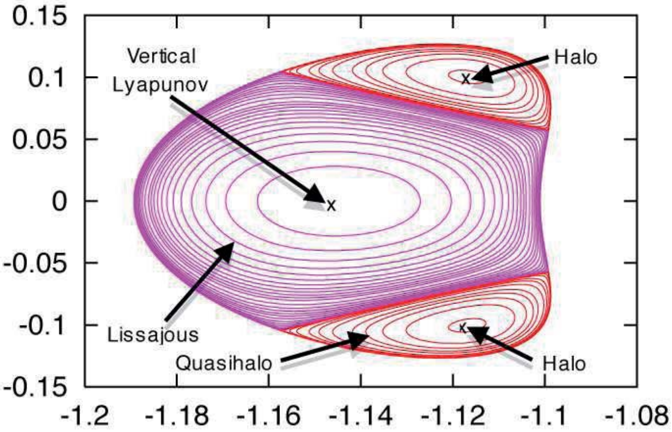

Figure 1.6: Poincaré section at $\{z = 0\}$ corresponding to the L_2 point of the Earth – Moon system for C =3.142003. In this (x, y) projection we can distinguish clearly different types of periodic and quasi-periodic orbits, all belonging to the central invariant manifold associated with L_2 and thus denoted as central orbits. See Gómez, Mondelo (2001).

this work, we refer to all these orbits as *central orbits.*

Figs. 1.7 and 1.8 show the evolution of the central manifolds of L_1 and L_2 according to the Jacobi constant (Gómez, Mondelo, 2001). For values of the Jacobi constant close to C_i $(i = 1, 2, 3)$ the central manifolds are only foliated by families of Lissajous orbits that connect the vertical Lyapunov periodic orbit with the planar one. For these values of the Jacobi constant, the motion is essentially quasi-periodic, except if the two frequencies of the Lissajous orbits are commensurable, in which case the motion is periodic. Decreasing the value of the Jacobi constant, we reach the energy level at which the halo orbits appear (they are represented by the two fixed points close to the boundaries of the plot). The value of the Jacobi constant at the bifurcation varies according to the mass ratio of the system and to the equilibrium point. Surrounding the fixed points associated with the halo orbits we have invariant curves related to quasi-periodic motion. These are the intersections of the quasi-halo orbits with the $\{z = 0\}$ plane. Decreasing further the Jacobi constant we detect several bifurcations of the halo orbits (by period triplication and doubling) as well as the invariant tori surrounding them.

The Hyperbolic Invariant Manifolds

Due to the saddle component of the linear approximation, the dynamics close to the L_1, L_2 and L_3 libration points is that of an unstable equilibrium. This means that each type of central orbit around a collinear point has a stable and an unstable invariant manifold. Each manifold has associated two branches, a positive and a negative one. They look like tubes (empty or solid) of asymptotic trajectories tending to, or departing

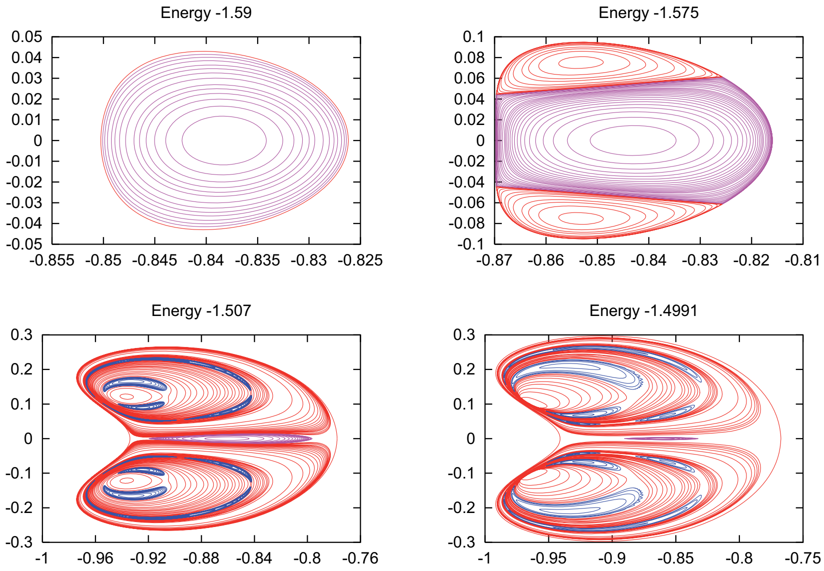

Figure 1.7: Energy slices of the $\{z = 0\}$ section, corresponding to the L_1 point of the Earth – Moon system. See Gómez, Mondelo (2001).

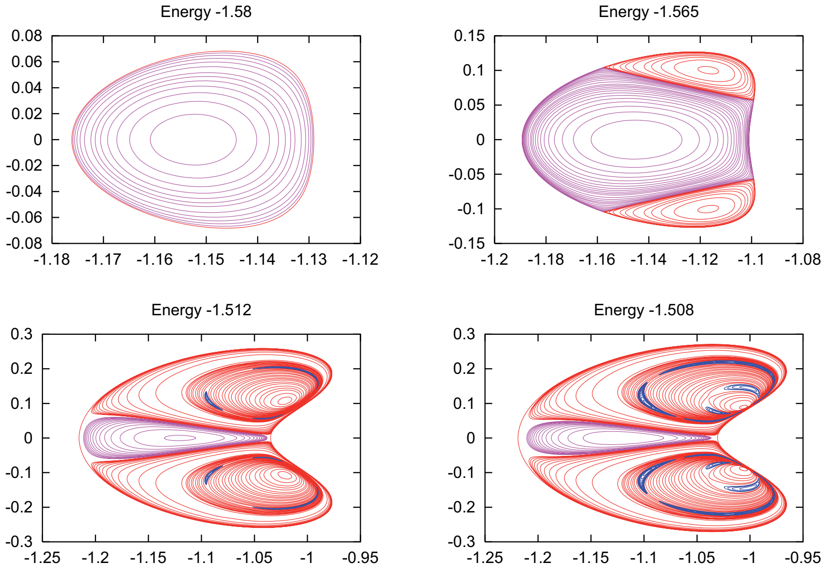

Figure 1.8: Energy slices of the $\{z = 0\}$ section, corresponding to the L_2 point of the Earth – Moon system. See Gómez, Mondelo (2001).

from, the corresponding orbit. These tubes have a key role in the study of the natural dynamics of the libration regions. When going forwards in time, the trajectories on the stable manifold approach exponentially the periodic/quasi-periodic orbit, while those on the unstable manifold depart exponentially. As a matter of fact (Conley, 1968; Llibre, Martínez, Simó, 1985; Gómez et al., 2004), these orbits separate two types of motion. The *transit* solutions are those orbits belonging to the interior of the manifold and passing from one region to another. The *non-transit* ones are those staying outside the tube and bouncing back to their departure region.

We refer to the stable/unstable invariant manifold associated with the central invariant manifold of a given equilibrium point as the union of the stable/unstable manifolds associated with each type of periodic and quasi-periodic orbits.

1.2.2 Invariant Manifolds Computation

The computation of the central and the hyperbolic objects can be done in different ways. Here, we describe how to compute hyperbolic manifolds associated with periodic orbits by means of a linear approximation and halo and Lissajous orbits, together with the corresponding stable and unstable manifolds, by a Lindstedt–Poincaré procedure. The reader interested in other approaches should refer to Masdemont (2005).

Numerical Linear Approximation

The linear approximation makes use of the eigenvectors, corresponding to the hyperbolic directions, of the monodromy matrix of a given periodic orbit.

Let $\mathbf{x}_0(t=0)$ be the initial condition of a $T-$periodic orbit, φ_t the flow at time t under the CR3BP vector field, $D\varphi_t$ its differential and $M := D\varphi_T(\mathbf{x}_0)$ the monodromy matrix. If the periodic orbit is hyperbolic, then there exist $\lambda_j,\ \lambda_j^{-1} \in \mathrm{Spec}(M)$ such that $\lambda_j \in \mathbb{R}/\{-1,1\}$. In this case, there exist a stable and an unstable manifold, which are tangent, respectively, to the λ_j and λ_j^{-1} eigendirections at $\mathbf{x}_0(0)$.

Let $\mathbf{v}_S(0)$ and $\mathbf{v}_U(0)$ be, respectively, the normalized stable and unstable eigenvector corresponding to the point $\mathbf{x}_0(0)$ on the periodic orbit considered, being the normalization performed in such a way that the position components of $\mathbf{v}_{S,U}(0)$ have modulus equal to 1. We recall that in the CR3BP case, just one hyperbolic eigenvector is sufficient to determine both branches of both manifolds, since the stable and the unstable directions are related by a symmetry relationship. More concretely, if $(v_1, v_2, v_3, v_4, v_5, v_6)$ is the eigenvector associated with λ_j, then $(v_1, -v_2, v_3, -v_4, v_5, -v_6)$ is the eigenvector associated with λ_j^{-1}.

The linear approximation for the initial conditions of the stable and the unstable manifold at $\mathbf{x}_0(0)$ is given, respectively, by

$$\begin{array}{rcl} \mathbf{x}_S(0) & = & \mathbf{x}_0(0) \pm \epsilon \mathbf{v}_S(0), \\ \mathbf{x}_U(0) & = & \mathbf{x}_0(0) \pm \epsilon \mathbf{v}_U(0), \end{array} \tag{1.6}$$

where ϵ is some small positive parameter. The value of ϵ fixes the size of the displacement we are performing from the periodic orbit to the hyperbolic manifold, if we use the above mentioned normalization for $\mathbf{v}_S(0)$ and $\mathbf{v}_U(0)$. Its value must be chosen in such a way to guarantee that $\mathbf{x}_0(0) \pm \epsilon \mathbf{v}_{S,U}(0)$ are still points where the linear and nonlinear manifolds are close. However, it cannot be too small to prevent from rounding errors. A typical value of $\epsilon = 10^{-4}$ (in the adimensional set of units) has been adopted in our computations. The sign of ϵ determines the branch of the manifold.

If $t \neq 0$, we can exploit the following relations:

$$\begin{aligned} \mathbf{x}_S(t) &= \varphi_t(\mathbf{x}_0(0)) \pm \epsilon D\varphi_t \cdot \mathbf{v}_S(0), \\ \mathbf{x}_U(t) &= \varphi_t(\mathbf{x}_0(0)) \pm \epsilon D\varphi_t \cdot \mathbf{v}_U(0), \end{aligned} \tag{1.7}$$

where the position components of $D\varphi_t \cdot \mathbf{v}_{S/U}(0)$ are normalized to 1.

The stable and unstable manifolds of the periodic orbits are 2–dimensional. Once a displacement ϵ has been selected, given a point $\mathbf{x}_0(0)$ on the periodic orbit, $\mathbf{x}_{S,U}(t)$, $t \in [0, T]$, provide initial conditions on the stable/unstable manifolds, which can be globalized by numerical integration. In this way, $\mathbf{x}_0(t)$, $t \in [0, T]$, can be thought as one of the parameters that generate the manifolds. It is usually called the *parameter along the orbit* or *phase*. The other parameter is the elapsed time for going, following the flow with increasing/decreasing t, from the initial condition to a certain point on the manifold. This time interval is usually called the *parameter along the flow*.

We remark that this parametrization depends on the choice of ϵ and on the way in which the stable/unstable direction is normalized. A small change in ϵ produces an effect equivalent to a small change in $\mathbf{x}_0(0)$, in the sense that with both changes we get the same orbits of the manifold. Only a small shift in the parameter along the flow will be observed. This is because the stable/unstable directions are transversal to the flow.

This procedure can be extended to the quasi-periodic orbits, see Simó (1998).

Semi-analytical Approximation

The Lindstedt–Poincaré method finds semi-analytical expressions for the invariant objects (orbits and manifolds) in terms of suitable amplitudes and phases by series expansions (Masdemont, 2005). This technique takes in consideration high order terms of the equations of motion and produces a formal series expansion of the solution of the equations of motion with high degree of accuracy. Although these expansions are in general divergent, some practical domains of convergence can be computed (see below).

Following Richardson (1980), the CR3BP equations of motion can be written as

$$\begin{aligned} \ddot{x} - 2\dot{y} - (1 + 2c_2)x &= \frac{\partial}{\partial x} \sum_{n \geq 3} c_n \rho^n P_n\Big(\frac{x}{\rho}\Big), \\ \ddot{y} + 2\dot{x} + (c_2 - 1)y &= \frac{\partial}{\partial y} \sum_{n \geq 3} c_n \rho^n P_n\Big(\frac{x}{\rho}\Big), \\ \ddot{z} + c_2 z &= \frac{\partial}{\partial z} \sum_{n \geq 3} c_n \rho^n P_n\Big(\frac{x}{\rho}\Big), \end{aligned} \tag{1.8}$$

where $\rho^2 = x^2 + y^2 + z^2$, P_n is the Legendre polynomial of order n and the c_n are suitable constants that only depend on the libration point and the mass ratio. Skipping the non-linear terms (which only appear on the right hand side of the equations) we find that the general solution of the linear system is

$$\begin{array}{rcl} x(t) & = & \alpha_1 \exp \lambda_0 t \ + \ \alpha_2 \exp(-\lambda_0 t) \ + \ \alpha_3 \cos(\omega_0 t + \phi_1), \\ y(t) & = & k_2 \alpha_1 \exp \lambda_0 t \ - \ k_2 \alpha_2 \exp(-\lambda_0 t) \ + \ k_1 \alpha_3 \sin(\omega_0 t + \phi_1), \\ z(t) & = & \alpha_4 \cos(\nu_0 t + \phi_2), \end{array} \tag{1.9}$$

where

$$\omega_0 = \omega_p, \quad \nu_0 = \omega_v, \quad \lambda_0 = \sqrt{\eta_2}, \quad k_1 = -\frac{\omega_0^2 + 1 + 2c_2}{2\omega_0}, \quad k_2 = \frac{\lambda_0^2 - 1 - 2c_2}{2\lambda_0},$$

and η_2 is the positive root of the characteristic polynomial of the linear system at the libration point (see Section 1.2.1).

The solution restricted to the central manifold (bounded orbits) is obtained setting $\alpha_1 = \alpha_2 = 0$. The values of α_3 and α_4 characterize the size of the orbit and are, respectively, the in–plane and the out–of–plane amplitudes, while ϕ_1 and ϕ_2 are the phases.

When considering the non-linear terms, the formal series solution is of the type

$$\begin{array}{rcl} x(t) & = & \sum \exp\left[(i-j)\theta_3\right]\left[x_{ijkm}^{pq} \cos(p\theta_1 + q\theta_2) + \bar{x}_{ijkm}^{pq} \sin(p\theta_1 + q\theta_2)\right] \alpha_1^i \alpha_2^j \alpha_3^k \alpha_4^m, \\ y(t) & = & \sum \exp\left[(i-j)\theta_3\right]\left[y_{ijkm}^{pq} \cos(p\theta_1 + q\theta_2) + \bar{y}_{ijkm}^{pq} \sin(p\theta_1 + q\theta_2)\right] \alpha_1^i \alpha_2^j \alpha_3^k \alpha_4^m, \\ z(t) & = & \sum \exp\left[(i-j)\theta_3\right]\left[z_{ijkm}^{pq} \cos(p\theta_1 + q\theta_2) + \bar{z}_{ijkm}^{pq} \sin(p\theta_1 + q\theta_2)\right] \alpha_1^i \alpha_2^j \alpha_3^k \alpha_4^m, \end{array} \tag{1.10}$$

where $\theta_1 = \omega t + \phi_1$, $\theta_2 = \nu t + \phi_2$ and $\theta_3 = \lambda t$ and

$$\omega = \sum \omega_{ijkm} \alpha_1^i \alpha_2^j \alpha_3^k \alpha_4^m, \qquad \nu = \sum \nu_{ijkm} \alpha_1^i \alpha_2^j \alpha_3^k \alpha_4^m, \qquad \lambda = \sum \lambda_{ijkm} \alpha_1^i \alpha_2^j \alpha_3^k \alpha_4^m,$$

and summations are extended over all $i, j, k, m \in \mathbb{N}$ and $p, q \in \mathbb{Z}$.

We notice that the Lindstedt–Poincaré expansion (1.10) corresponds to the solution of the Birkhoff normal form equations (Delshams, Masdemont, Roldán, 2008).

The Lindstedt–Poincaré procedure computes the coefficients x_{ijkm}^{pq}, y_{ijkm}^{pq}, z_{ijkm}^{pq}, ω_{ijkm}, ν_{ijkm} and λ_{ijkm} up to a finite order $N = i+j+k+m$. In this way, for a given equilibrium point and for a certain epoch t, we can compute the position and the velocity of the particle in terms of the four amplitudes and the two phases. Setting $\alpha_1 = \alpha_2 =0$ we obtain Lissajous orbits of amplitudes α_3 and α_4 and phases ϕ_1 and ϕ_2; setting $\alpha_1 =$, and $\alpha_2 \neq 0$ ($\alpha_2 =0$, $\alpha_1 \neq 0$) we get their stable (unstable) manifold.

Throughout this work, we refer to *square* Lissajous orbits as Lissajous orbits with equal in–plane and out–of–plane amplitudes, $\alpha_3 = \alpha_4$. In turn, this means that the $x-$amplitude is equal to the $z-$one (the $y-$ amplitude is usually 3 times larger). In Fig. 1.9, we show a square Lissajous orbit around L_1 and the (x, y) projection of some orbits of the positive branch of the associated stable invariant manifold.

In practice, the order N is defined as a pair (n_1, n_2). The sub-order $n_1 = i+j$ corresponds to the hyperbolic part whilst the sub-order $n_2 = k+m$ corresponds to the central part.

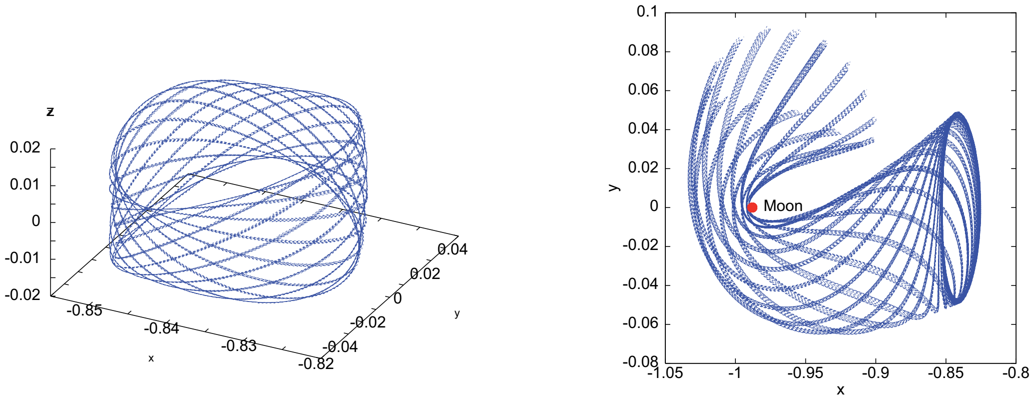

Figure 1.9: Left: Lissajous quasi-periodic orbit with $\alpha_3 = \alpha_4 = 0.09$ normalized units ($\approx$ 6000 km) around the point L_1 in the Earth – Moon system. Right: trajectories of the positive branch of the stable invariant manifold associated with this Lissajous orbit ((x, y) projection). We take 15 values of $\phi_1 \in [0, 2\pi]$ and 15 values of $\phi_2 \in [0, 2\pi]$.

This is useful since to compute the terms of order (n_1, n_2) only the terms of order $(\overline{n}_1, \overline{n}_2)$ with $\overline{n}_1 < n_1$ and $\overline{n}_2 < n_2$ are needed. This fact allows us to truncate the Lindstedt–Poincaré expansions at order (n_1, n_2) not necessarily with $n_1 = n_2$.

Halo orbits appear when the two frequencies are equal, that is, when the in–plane motion and the out–of–plane one have the same period. However, substituting $\omega_0 = \nu_0$ in the linear solution does not produce a solution of the linear part of (1.8). To this end, we must add a term like Δz (with $\Delta = c_2 - \omega_0^2$) to the third equation in (1.8) in order to obtain the same in–plane and out–of–plane frequency. When considering the non-linear part, we look for expansions of the solution analogous to (1.10), adding to the third differential equation the Δz term, with

$$\Delta = \sum \Delta_{ijkm} \alpha_1^i \alpha_2^j \alpha_3^k \alpha_4^m = 0. \tag{1.11}$$

As a consequence, the in–plane and out–of–plane amplitudes α_3 and α_4 are no longer independent.

In Fig. 1.10, we show the positive and the negative branch of the stable manifold of the halo orbit around the L_1 point with $\alpha_4 = 0.15$ normalized units ($\approx$ 8500 km).

On the Convergence of the Series

The Lindstedt–Poincaré procedure has the drawback to depend on the order of the expansion used. Because of this, we tested the library of routines, that implement the semi-analytical approach, in order to understand how much we could rely on it.

We compared the results obtained by the numerical integration and those given by formal series expansion to find the maximum time at which they coincide under a given tolerance (10^{-6}). This experiment was performed on halo and Lissajous orbits, by computing the

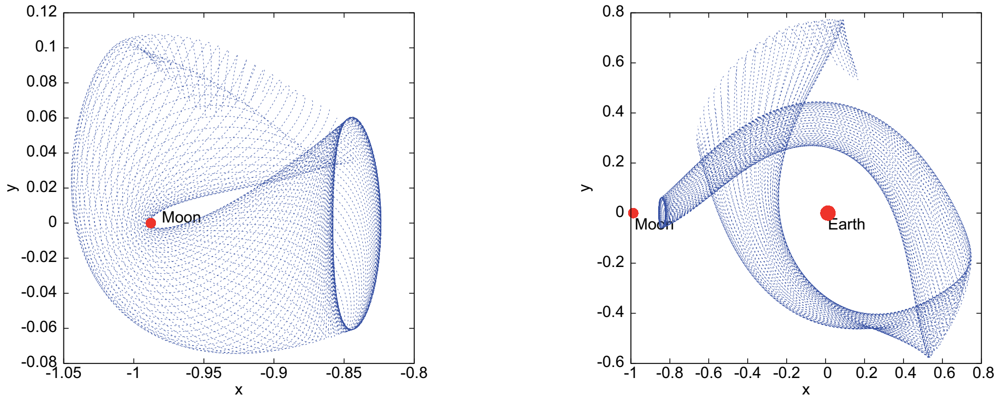

Figure 1.10: (x, y) projections of the positive (left) and the negative (right) branch of the stable manifold of the halo orbit around the L_1 point with $\alpha_4 = 0.15$ normalized units ($\approx$ 8500 km).

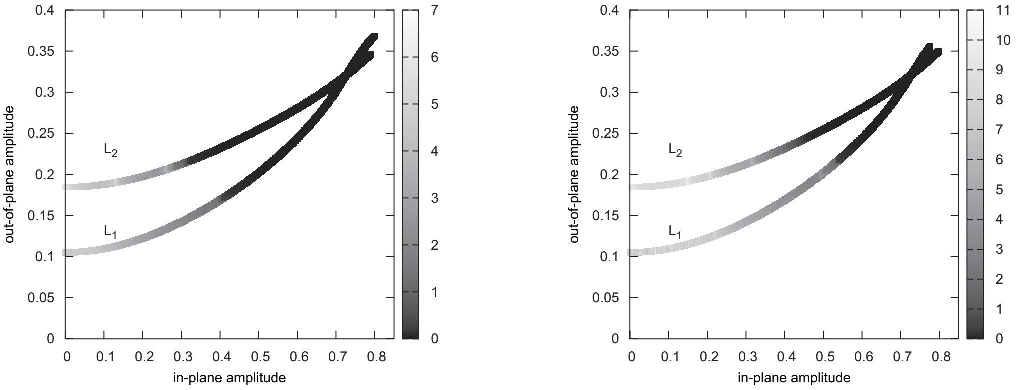

Figure 1.11: Test on the Lindstedt–Poincaré series expansion of the halo orbits in the Earth – Moon system. Left: order 15; right: order 25. The shade of gray of the points refers to the time of agreement (in terms of adimensional units) between the semi-analytical series expansion and the numerical integration. See explanation in the text.

difference in position and the difference in velocity of the two approximations. We considered the series expansion reliable if the time in modulus was greater than 1.5 adimensional units (about 6.5 days). We notice that this type of test cannot be done for an arbitrarily high interval of time, due to the high instability of the region under study. The results associated with the halo case are showed in Fig. 1.11: on the left, the expansion up to order 15, on the right up to order 25. In Fig. 1.12, we can see what happens for the Lissajous case with an order 25 series expansion. Both in the halo and in the Lissajous case, the smaller the value of the Jacobi constant, that is, greater the amplitude of the orbit, the smaller the time of agreement. We notice that around the L_1 point the range of satisfactory amplitudes is smaller when compared to the L_2 case. It is also worth to observe that for order 25 expansions, the maximum time of agreement for halo orbits is of about 11 adimensional units, for Lissajous orbits this value gets at most to 3.5 adimensional units.

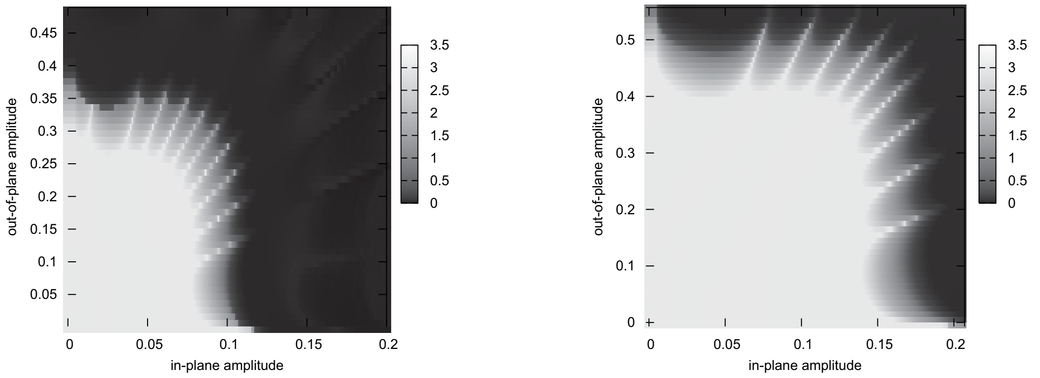

Figure 1.12: Test on the order 25 Lindstedt–Poincaré series expansion of the Lissajous orbits in the Earth – Moon system. On the left, around the L_1 point; on the right, around the L_2 point. The darker the shade of gray of the points the smaller the time of agreement (in terms of adimensional units) between the semi-analytical series expansion and the numerical integration. See explanation in the text.

We stress that all the tests above have been performed on the central part associated with the equilibrium points and that we consider the two phases ϕ_1 and ϕ_2 equal to 0. For further results concerning the hyperbolic components and other values of ϕ_i $(i = 1, 2)$, see Masdemont (2005).

1.2.3 Transit Orbits

As said before, transit orbits live inside the tubes represented by the hyperbolic invariant manifolds. In principle, one can compute these trajectories starting from a given kind of periodic or quasi-periodic orbit. However, it can be of interest to describe the behavior of transit trajectories associated with the whole stable/unstable invariant manifold corresponding to the central invariant manifold of a nominal collinear equilibrium point $\mathcal{W}^{s/u}(\mathcal{W}^c_{L_i})$ $(i = 1, 2, 3)$ for a certain value of the Jacobi constant.

To this end we develop an efficient way to represent the dynamics driven by $\mathcal{W}^{s/u}(\mathcal{W}^c_{L_i})$ $(i = 1, 2, 3)$ for each energy level, with no distinction on central orbits. This can be of utility also in case of high energy levels, where we have seen that the Lindstedt–Poincaré procedure is not able to produce accurate either Lissajous/halo orbits or the corresponding hyperbolic manifolds.

The main idea is to determine $\mathcal{W}^{s/u}(\mathcal{W}^c_{L_i})$ $(i = 1, 2, 3)$ using only the desired hyperbolic invariant manifolds of the planar and vertical periodic orbits, $\mathcal{W}^{s/u}(PL_{L_i})$ and $\mathcal{W}^{s/u}(VL_{L_i})$ $(i = 1, 2, 3)$, respectively. In particular, for a well-defined value of C and a given collinear point, the stable/unstable invariant manifold associated with the central invariant manifold is included in the product of the stable/unstable invariant manifold associated with the planar Lyapunov orbit and the stable/unstable invariant manifold corresponding to the vertical Lyapunov orbit, namely,

$$\mathcal{W}^{s/u}(\mathcal{W}^c_{L_i}) \subset \mathcal{W}^{s/u}(PL_{L_i}) \times \mathcal{W}^{s/u}(VL_{L_i}), \qquad i = 1, 2, 3. \tag{1.12}$$

Transit trajectories of the stable/unstable invariant manifold associated with any central orbit lie inside the above product. The meaning of such inclusion (1.12) will be explained in what follows with more details, taking as example $\mathcal{W}^s(\mathcal{W}^c_{L_2})$.

Geometric Behavior

For a fixed value of C, around a given equilibrium point there are one planar and one vertical Lyapunov periodic orbit plus several Lissajous orbits of different amplitudes and other types of periodic and quasi-periodic motions, whose existence depends on the energy level considered (Gómez, Mondelo, 2001).

Let us consider, for a well-defined energy level, the first crossing of the stable invariant manifold associated with different central orbits with the $\{x = 0\}$ plane (see Fig. 1.13). In the $(y, \dot{y})$ and $(z, \dot{z})$ projections, the hyperbolic manifold associated with the vertical Lyapunov periodic orbit gives rise to a single closed curve, the one associated with the planar Lyapunov periodic orbit generates, respectively, a single closed curve and a point at the origin. On the other hand, in both projections the hyperbolic manifold associated with a Lissajous orbit, which has dimension 3, produces an annular region, composed by infinitely many closed curves chained together. Clearly, this is because a periodic orbit is a $\mathbb{S}^1$ object, a Lissajous orbit is a $\mathbb{T}^2$ one. If we fix the value of one of the two phases characterizing a Lissajous orbit, say ϕ_1, and let the value of the other, say ϕ_2, to vary in $[0, 2\pi]$ we get one of the closed curves forming the annular region, as shown in Fig. 1.13 on the right.

Keeping constant the value of C, distinct Lissajous orbits are found by increasing the out–of–plane amplitude and decreasing the in–plane one or vice versa. The $(y, \dot{y})$ and $(z, \dot{z})$ projections corresponding to the hyperbolic manifolds associated with different Lissajous orbits with similar values of the amplitudes may cross each other, but they tend to stay one inside the other. Furthermore, the greater the out–of–plane amplitude of a nominal Lissajous orbit the closer the projections of the associated hyperbolic manifold to the projections associated with the vertical Lyapunov periodic orbit. In the limit case, when the Lissajous orbit takes vertical amplitude almost as big as that of the vertical Lyapunov periodic orbit, the two projections overlap. The same argument holds with

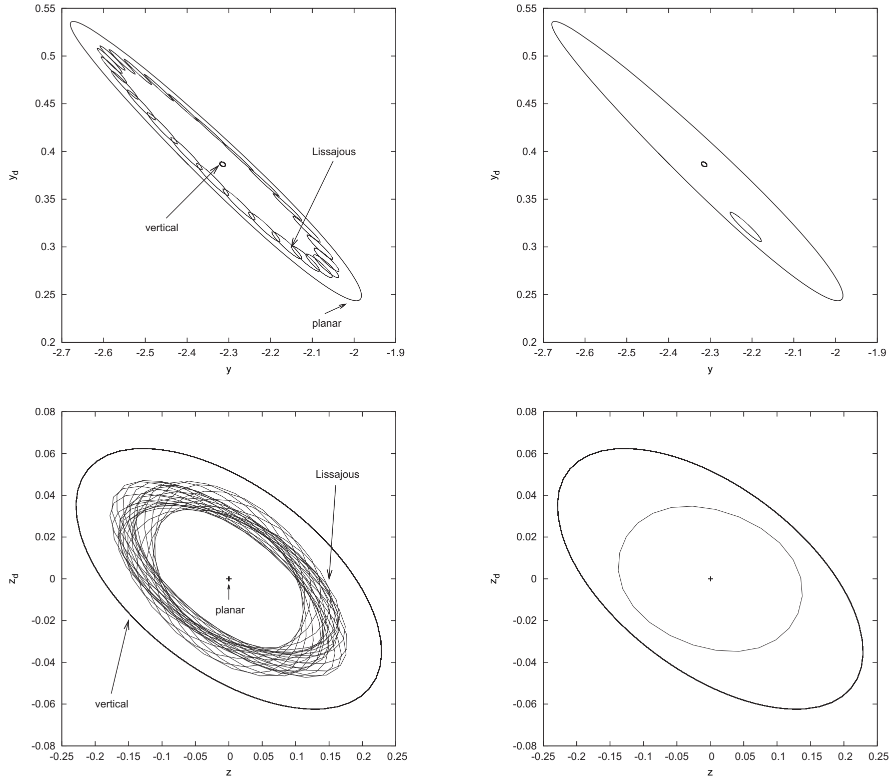

Figure 1.13: $(y, \dot{y})$ and $(z, \dot{z})$ projections of the first crossing with the $\{x = 0\}$ plane of the stable invariant manifold associated with different types of central orbits of energy C =3.163, around the L_2 point. On the top left, one can see that the projection corresponding to the manifold associated with the planar Lyapunov orbit is a single closed curve which contains the projections of all the other central orbits. On the bottom left, the projection corresponding to the manifold associated with the vertical Lyapunov orbit is again a single closed curve which contains all the other projections. On the right, we represent the same behavior, underlining that each closed curve constituting the projection of the hyperbolic manifold associated with the Lissajous orbit corresponds to a fixed value of one of the two phases.

respect to the planar Lyapunov periodic orbit when increasing the in–plane amplitude. This is shown in Fig. 1.14.

If we consider other sections or other types of central orbits apart from the Lissajous ones, the same qualitative behavior is found. In turn, the role of outer bound is played by the hyperbolic manifold associated with the planar Lyapunov periodic orbit in the $(y, \dot{y})$ projection, by the one associated with the vertical Lyapunov periodic orbit in the $(z, \dot{z})$ plane. This result is analogous to the well-known Poincaré map representation of the central manifold dynamics (see Fig. 1.6).

This explains how the hyperbolic manifolds associated with planar and vertical Lyapunov orbits act as energy boundaries for transit orbits lying inside $\mathcal{W}^{s/u}(\mathcal{W}^c_{L_i})$.

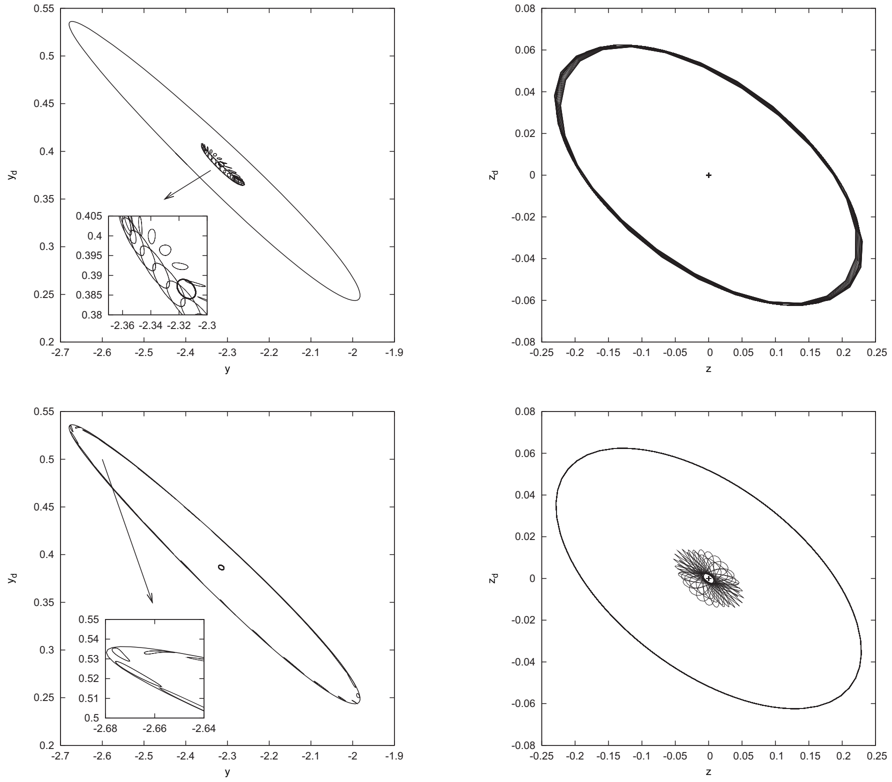

Figure 1.14: $(y, \dot{y})$ and $(z, \dot{z})$ projections of the first crossing with the $\{x = 0\}$ plane of the stable invariant manifold associated with different types of central orbits of energy C =3.163, around the L_2 point. On the top, the Lissajous orbit has a considerable out–of–plane amplitude (and a very small in–plane one) and thus the projections of the associated stable manifold tend to overlap with the ones associated with the vertical Lyapunov periodic orbit. On the bottom, the Lissajous orbit has a considerable in–plane amplitude (and a very small out–of–plane one) and thus the projections of the associated stable manifold tend to overlap with the ones associated with the planar Lyapunov periodic orbit.

1.3 The Bicircular Restricted Four – Body Problem

The Bicircular Restricted Four – Body Problem (Cronin, Richards, Russell, 1964) considers the infinitesimal mass P to be affected by the gravitational attractions of three primaries.

We introduce this model in order to include the effect of the Sun in the Earth – Moon system. Earth and Moon revolve in circular orbits around their common center of mass and, at the same time, this barycenter and the Sun move on circular orbits around the center of mass of the Earth – Moon – Sun system.

The usual framework to deal with is the synodical reference system with origin at the Earth – Moon barycenter: in this way Earth and Moon are fixed on the $x-$axis as before

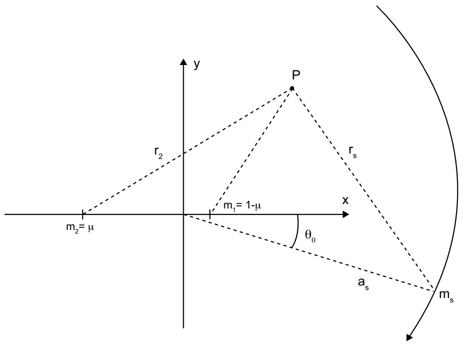

Figure 1.15: The Bicircular Restricted Four – Body Problem in the synodical reference system with adimensional units.

and the Sun is supposed turning clockwise around the origin. We notice that the three massive bodies are assumed to move in the same plane and that the model is not coherent in the sense that the motion of the primaries does not satisfy the Newton's equations.

Let us take adimensional units as in the CR3BP and let $m_S = 328900.5614$ be the mass of the Sun in such units, a_S be the distance between the Earth – Moon barycenter and the Sun, ω be the mean angular velocity of the Sun in synodical coordinates and θ_0 be the value associated with the rotation of the Sun with respect to the Earth – Moon barycenter at $t = 0$. See Fig. 1.15.

If $\theta = \omega t$, then the position of the Sun is described by

$$x_S = a_S \cos(\theta - \theta_0), \qquad y_S = -a_S \sin(\theta - \theta_0), \tag{1.13}$$

and the equations of motion for the particle P can be written as

$$\begin{aligned}
\ddot{x} - 2\dot{y} &= x - \frac{(1-\mu)}{r_1^3}(x-\mu) - \frac{\mu}{r_2^3}(x+1-\mu) - (x - x_S)\frac{m_S}{r_S^3} - \cos(\theta - \theta_0)\frac{m_S}{a_S^2}, \\
\ddot{y} + 2\dot{x} &= y - \frac{(1-\mu)}{r_1^3}y - \frac{\mu}{r_2^3}y - (y - y_S)\frac{m_S}{r_S^3} - \sin(\theta - \theta_0)\frac{m_S}{a_S^2}, \\
\ddot{z} &= -\frac{(1-\mu)}{r_1^3}z - \frac{\mu}{r_2^3}z - z\frac{m_S}{r_S^3},
\end{aligned} \tag{1.14}$$

where μ has the same meaning and value as the one introduced in Section 1.2 and $r_1 = [(x-\mu)^2 + y^2 + z^2]^{\frac{1}{2}}$, $r_2 = [(x+1-\mu)^2 + y^2 + z^2]^{\frac{1}{2}}$, $r_S = [(x-x_S)^2 + (y-y_S)^2 + z^2]^{\frac{1}{2}}$ are the distances from P to Earth, Moon and Sun, respectively.

We recall that this problem does not admit either first integrals or equilibrium points.

We note that in the case of a planet without a moon it is still possible to apply the BR4BP by considering two planets and the Sun. For instance, we can assume Sun and Mercury to move as in the CR3BP and Venus to move around their barycenter on a circular orbit lying on the same plane. For more details, refer to Gabern (2003).

1.4 The Restricted n – Body Problem

In the Restricted n – Body Problem framework, we assume the massless particle P to move under the gravitational influence of $n-1$ massive bodies. We consider the nine planets, Moon and Sun. The conventional formulation considers an equatorial reference system centered at the Solar System barycenter with physical units of distance, time and mass (AU, day and kg). In this work, the position and velocity for the massive bodies, say $\mathbf{X}_p \equiv (x_p, y_p, z_p, \dot{x}_p, \dot{y}_p, \dot{z}_p)$, at a given instant of time are furnished by the JPL ephemerides DE405, which range from JED 2305424.50 (December 9, 1599) to JED 2525008.50 (February 20, 2201). The equations of motion for the spacecraft can be written as

$$\begin{aligned} \ddot{x} &= -\sum_{p=1}^{11} G m_p \frac{(x - x_p)}{r_p^3}, \\ \ddot{y} &= -\sum_{p=1}^{11} G m_p \frac{(y - y_p)}{r_p^3}, \\ \ddot{z} &= -\sum_{p=1}^{11} G m_p \frac{(z - z_p)}{r_p^3}, \end{aligned} \tag{1.15}$$

where $r_p = \sqrt{(x - x_p)^2 + (y - y_p)^2 + (z - z_p)^2}$ is the distance between the planet p and the particle, G is the gravitational constant and m_p is the mass of the body p.

We recall that the JPL ephemerides DE405 (Standish, Williams) result from a least-squares adjustment of a previously existing ephemeris to a variety of observational measurements, followed by a numerical integration of the equations of motion which describe the physics of the Solar System. These fundamental ephemerides are the bases for computing the planetary and lunar positions and other related phenomena. The equations of motion used for the creation of DE405 include contributions from pointmass interactions among the Moon, planets, and Sun; general relativity; Newtonian perturbations of selected asteroids; action upon the figure of the Earth from the Moon and Sun; action upon the figure of the Moon from the Earth and Sun; libration of the Moon, modeled as a solid body with tidal and rotational distortion, including both elastic and dissipational effects; the effect upon the Moon's motion caused by tides raised upon the Earth by the Moon and Sun.

The internal reference system for such ephemerides, the so-called J2000, is a Cartesian frame, with origin at the Solar system barycenter, the $x-y$ plane is parallel to the mean Earth Equatorial plane, the $z-$axis is orthogonal to this plane, the $x-$axis points to the vernal point and the $y-$axis is selected to have a positive oriented reference system. All these references are taken at January 1st, 2000, at 12:00 UT.

Since we are going to focus our study in the Earth – Moon neighborhood, it might be convenient to evaluate the position and velocity of P with respect to the Earth. In other words, we attempt to avoid the cancellation problems which might occur when considering a trajectory far from the Solar System barycenter. To this end, we perform

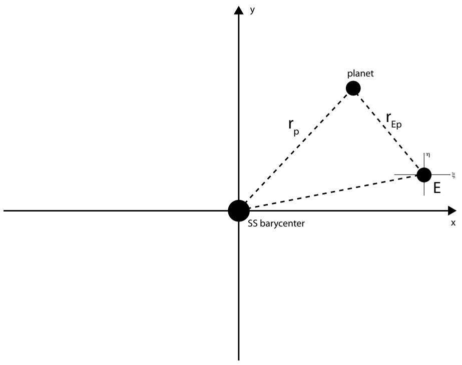

Figure 1.16: Change of coordinates performed in order to describe the behavior of the probe with respect to the Earth and not the Solar System barycenter.

the following change of coordinates:

$$\mathbf{\Xi} := \mathbf{X} - \mathbf{X}_E \equiv (x - x_E, y - y_E, z - z_E, \dot{x} - \dot{x}_E, \dot{y} - \dot{y}_E, \dot{z} - \dot{z}_E) =: (\xi, \eta, \zeta, \dot{\xi}, \dot{\eta}, \dot{\zeta}), \quad (1.16)$$

where $\mathbf{X}_E$ represents position and velocity of the Earth. See Fig. 1.16.
The vector field to be considered is now

$$\begin{aligned} \ddot{\xi} &= -\sum_{p=1}^{11} G m_p \frac{(x_E - x_p + \xi)}{r_{Ep}^3} - \ddot{x}_E, \\ \ddot{\eta} &= -\sum_{p=1}^{11} G m_p \frac{(y_E - y_p + \eta)}{r_{Ep}^3} - \ddot{y}_E, \\ \ddot{\zeta} &= -\sum_{p=1}^{11} G m_p \frac{(z_E - z_p + \zeta)}{r_{Ep}^3} - \ddot{z}_E, \end{aligned} \quad (1.17)$$

where $r_{Ep} = \sqrt{(x_E - x_p + \xi)^2 + (y_E - y_p + \eta)^2 + (z_E - z_p + \zeta)^2}$.

ASTRODYNAMICAL APPLICATIONS

RESCUE LUNAR ORBITS 2

2.1 Introduction

The problem we address in this chapter is the computation of trajectories that can connect the surface of the Moon and a libration point orbit (LPO). Within the framework of the CR3BP, the transfers lie on the hyperbolic invariant manifolds associated with the central invariant manifold of the collinear points L_1 and L_2.

We are motivated by the new interest that lunar missions have recently gained. In September 2007, the Japanese space agency (JAXA) launched the mission SELENE, designed to obtain scientific information about the lunar surface and environment and to develop the appropriate technology for a future lunar exploration. Other lunar missions have been successful in the latest years: in 2007 Chang'e 1 was launched by China, in 2008 Chandrayaan-1 by India and LRO and LCROSS by U.S. in 2009. Major objectives of such missions are a deeper understanding of the lunar origin and evolution, the study of the global dynamics of terrestrial plasmasphere and the return of humans to the Moon.

In this context, L_1 and L_2 LPOs could play an important role. Orbits around L_1 may stand for optimal rendezvous location between the Earth and the Moon, while LPOs around L_2 can either be used to observe the lunar farside or serve as intermediate step for interplanetary transfers. All these ideas have already been considered by Lo, Ross (2001) in relation to the lunar gateway station.

With respect to a manned installation on the Moon, it would aim at the creation of a new platform to observe the universe and explore the Solar System. Clearly, this would require usable resources in terms of material and water. A special attention is devoted to the polar regions of the Moon where continuous access to solar illumination may be possible. Besides, two impactors from the LCROSS mission corroborated the presence of water in some permanently shadowed areas of south polar craters and further confirmations on the existing amount are expected.

We recall that the Apollo missions were planned by adopting the so-called *lunar rendezvous scheme*. This is, a Keplerian equatorial orbit around the Moon from which the lunar module descends to the lunar surface. After having made the proper observations, it would rejoin the orbiting command module. At the present day, the scientific community is looking for different solutions that could guarantee low transfer time, great amount of allowed payload, total lunar surface access and affordable propellant consumption.

Keeping this in mind, we focus on halo and Lissajous orbits either around L_1 or L_2.

We examine the behavior of the corresponding stable invariant manifold if we look for rescue orbits that depart from the Moon, the behavior of the unstable one for trajectories landing on the Moon. We recall that a stable invariant manifold is composed by orbits which approach the periodic/quasi-periodic orbit forwards in time, so if they depart from the surface of the Moon is because they arrive there backwards in time after starting close to the reference periodic/quasi-periodic orbit. Vice versa, the unstable manifold gets to the Moon forwards in time.

We analyze how the trajectories on these invariant objects can leave/reach the Moon's surface, that is: the accessible regions on the Moon, the velocity and the angle of departure/arrival and the time required for the transfer. Special emphasis will be put on direct transfers, which land almost tangentially and depart almost orthogonally to the lunar surface.

Baoyin, McInnes (2006) studied an analogous problem, this is, how to go from the Moon to a planar L_1/L_2 Lyapunov periodic orbit in the framework of the Planar Circular Restricted Three – Body Problem. We note that the planar Lyapunov orbits correspond to Lissajous orbits with the vertical amplitude α_4 equal to zero. They focused their attention to lunar surface coverage, initial and arrival flight path angles, transfer time and initial velocity. They found out that a whole surface coverage can be obtained only at specific energy levels and that the smallest attainable orbit around L_1 can be reached in about 11 days (14 days for L_2).

2.2 Methodology

The design of trajectories that can depart from the surface of the Moon and arrive to the neighborhood either of L_1 or L_2 is established on the numerical globalization of the stable invariant manifold of a nominal LPO. For orbits landing on the Moon we take advantage of the corresponding unstable invariant manifold, instead. In both cases, we assume the Moon to be a sphere of radius $r_M = 1737.53$ km. The computation of halo and Lissajous families of orbits together with the associated $\mathcal{W}^{s/u}$ is done by means of an order 25 Lindstedt–Poincaré series expansion (see Section 1.2.2).

We implement a Poincaré map strategy by defining the Poincaré section as

$$S := r_2^2 - r_M^2 = 0, \tag{2.1}$$

where r_2 represents the distance from the minor primary to the particle.

Given an initial condition on the suitable branch of the hyperbolic manifold we are interested in, we propagate it backwards in time if we deal with $\mathcal{W}^s$, forwards otherwise. The numerical integration is performed by means of a 7-8 Runge-Kutta-Fehlberg method with local truncation error $\epsilon = 10^{-14}$.

The construction of the Poincaré map is done as follows. At each integration step we check if the value of S changes sign and in this case, we refine the point obtained using the Newton's method within a tolerance of $|S| = 10^{-12}$. This is, denoting by $\mathbf{X}^{(i)}$ the

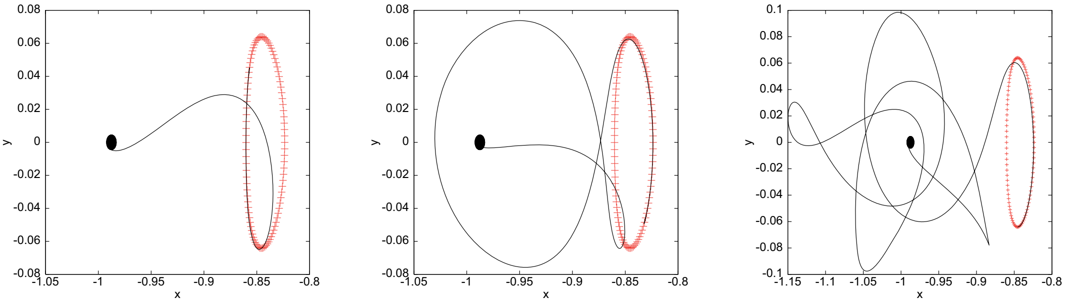

Figure 2.1: (x, y) projection of three trajectories of the stable invariant manifold associated with the L_1 halo orbit with $\alpha_4 = 0.2$ normalized units (≈ 11000 km) in the Earth – Moon system. From left to right, the trajectory reaches the Moon backwards in time without minima of the r_2 function, after one close encounter and after four loops around the Moon.

$i-$iteration of the procedure, we compute the sequence of points

$$\mathbf{X}^{(i+1)} = \mathbf{X}^{(i)} - \frac{S}{DS}, \qquad \text{where} \qquad DS = 2(x - \mu + 1)\dot{x} + 2y\dot{y} + 2z\dot{z}, \tag{2.2}$$

until the stopping condition is fulfilled.

Whenever we get a trajectory arriving to the Moon backwards/forwards, we compute the lunar latitude β and longitude λ corresponding to the point obtained, namely,

$$\beta \;=\; \tan^{-1}\left(\frac{z}{\sqrt{(x-\mu+1)^2 + y^2}}\right), \qquad \lambda \;=\; \tan^{-1}\left(\frac{y}{x-\mu+1}\right). \tag{2.3}$$

In our exploration $(\beta = 0°, \lambda = 0°)$ corresponds to the Moon's point which is the closest to the Earth.

In addition, we calculate the physical velocity of departure/arrival, the physical transfer time and the departure/arrival angle ϑ, defined as the angle between the velocity vector, $\mathbf{v}$, and the vector which is normal to the Moon's surface, ∇S, namely,

$$\cos\vartheta = \frac{\mathbf{v} \cdot \nabla S}{\|\mathbf{v}\| \; \|\nabla S\|}. \tag{2.4}$$

Of course, not all the orbits of a certain manifold can reach the surface of the Moon. To prevent from long time integrations we set some controls. If after 10 adimensional time units (about 43.5 days) the function S has not changed sign, we move to the next trajectory of the manifold to be explored. Increasing the final time we get some more collision orbits but, from a qualitative point of view, the results are almost identical.

The second control takes into account how many times the orbit has gone close to the Moon without getting to it. We are interested in almost direct transfers and we do not see operational advantages in trajectories winding around the Moon indefinitely. For this purpose we compute the number of minima of the r_2 function along the orbits. This is, how many times the function

$$\dot{r}_2 = \frac{(x-\mu+1)\dot{x} + y\dot{y} + z\dot{z}}{r_2}$$

changes sign and simultaneously

$$\ddot{r}_2 = \frac{\dot{x}^2 + \dot{y}^2 + \dot{z}^2 + (x-\mu+1)\ddot{x} + y\ddot{y} + z\ddot{z} - \dot{r}_2^2}{r_2} > 0.$$

If we get more than 5 minima, then we discard such trajectory and we proceed to explore the next initial condition on the manifold. Indeed, we have seen that in this case the orbit remains revolving around the Moon up to a considerably large time.

We remark that we discard the minima associated with the loops exhibited by the trajectories before leaving the neighborhood of the periodic/quasi-periodic orbit.

For illustration purposes, in Fig. 2.1 we display three trajectories of the stable invariant manifold of the L_1 halo orbit with $z-$amplitude $\alpha_4 = 0.2$ normalized units (≈ 11000 km). The one on the left reaches the Moon directly, the one in the middle after performing one loop around the Moon and the one on the right after performing four.

2.3 Numerical Results

We apply the above procedure using as reference L_1 and L_2 halo and Lissajous orbits. As already said, each hyperbolic invariant manifold has two branches and only one of them goes directly towards the Moon, depending on the sign of α_2 and α_1. For trajectories departing from the Moon having as target orbits around L_1, we take $\alpha_2 > 0$; if they are expected to arrive to L_2, $\alpha_2 < 0$. The same holds for α_1 if the orbits belong to the unstable invariant manifold and thus arrive to the Moon.

2.3.1 Halo Arrival/Departure

For halo orbits around the L_1 point we take values of the $z-$amplitude $\alpha_4 \in [0.01, 0.45]$ normalized units, that is, approximatively up to 23000 km (or, equivalently, the Jacobi constant ranges from 3.14100 to 3.18633). For L_2, we allow the z–amplitude to vary up to 0.35 normalized units, that is, approximatively 28000 km, or $C \in [3.14254, 3.16410]$. The exploration is carried out varying the $z-$amplitude at step equal to 10^{-3} normalized units in both cases. For the suitable branch of each manifold, we explore 5000 different orbits associated with values of the parameter along the orbit equally spaced in $[0, 2\pi]$.

In Figs. 2.2 and 2.3, we display the accessible departure regions on the Moon associated with I class halo orbits around the L_1 and L_2 equilibrium points. The orbits which give rise to such regions are trajectories of the stable invariant manifold that, starting at a given halo orbit (and integrating backwards in time), reach the lunar surface after having 0 (left) and up to 5 (right) close approaches with the Moon (minima of the r_2 function).

The departure regions corresponding to II class orbits are symmetric with respect to the $\{\beta = 0\}$ axis to the ones obtained for I class orbits, provided the same number of

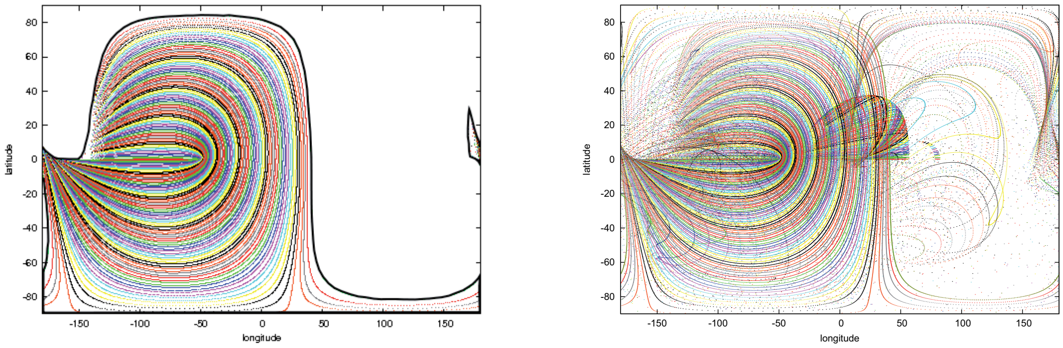

Figure 2.2: Longitude and latitude of the accessible departure zones of the Moon associated with I class halo orbits around the L_1 libration point. The two plots correspond to rescue orbits with 0 loops around the Moon before reaching the halo orbit (left) and with 5 or less loops (right). The range of amplitudes explored goes from $\alpha_4 = 0.01$ normalized units (≈ 500 km) to $\alpha_4 = 0.45$ normalized units (≈ 23000 km).

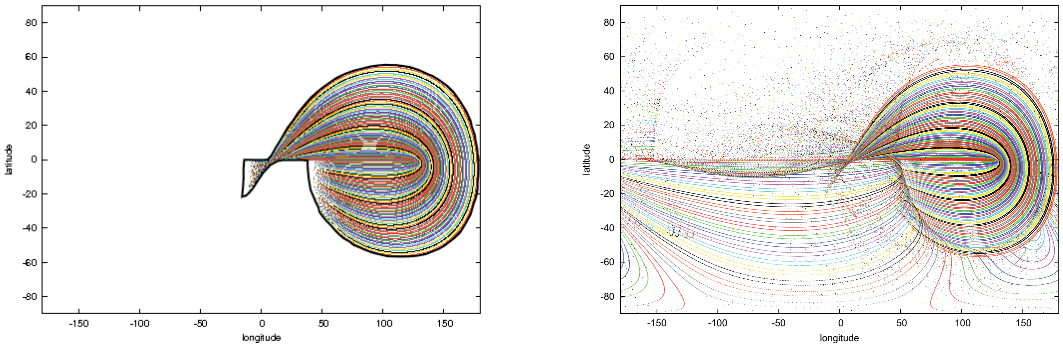

Figure 2.3: Longitude and latitude of the accessible departure zones of the Moon associated with I class halo orbits around the L_2 libration point. The two plots correspond to rescue orbits with 0 loops around the Moon before reaching the halo orbit (left) and with 5 or less loops (right). The range of amplitudes explored goes from $\alpha_4 = 0.01$ normalized units (≈ 1000 km) to $\alpha_4 = 0.35$ normalized units (≈ 28000 km).

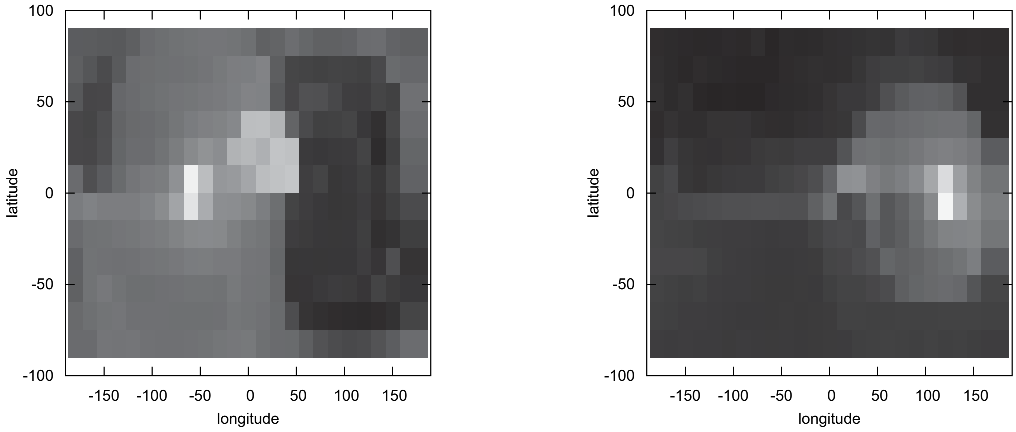

Figure 2.4: Density of opportunities of departure from the Moon's surface per unit of length of the arrival orbit and per unit of area element. The lighter the shade of gray the greater the chance. On the left, the L_1 case; on the right, the L_2 one.

minima. This is expected from the existing symmetry between northern and southern halo orbits with respect to the $\{z = 0\}$ plane.

In general, the patterns defining the accessible regions displayed in the figures are composed by different curves, each one associated with a halo orbit of a certain amplitude. Depending on the amount of close approaches to be performed, we can distinguish several families of longitude/latitude curves. For direct transfers, the curves in the middle of the pattern, that is, the shortest ones, are associated with halo orbits with the smallest amplitudes. On the other hand, for the L_1 case the curves covering almost the whole longitude's range are those with $\alpha_4 \geq 0.43$ normalized units (≈ 22000 km).

As it is clear from the plots corresponding to 0 minima, the regions on the lunar surface, from which we can reach a halo orbit without performing any loop around the Moon in between, cover (approximatively) only one half of the total surface. As we increase the number of allowed loops, the area of the region increases and by means of 3 or more loops the surface of the Moon is completely covered. In other words, if we allow at least 3 minima, one can reach the halo families departing from any point of the surface of the Moon.

However, we remark that the points of allowed departure are not uniformly distributed on the Moon's surface. There exist regions where we have more chances to take off joining the stable invariant manifold associated with a given halo orbit. This is illustrated in Fig. 2.4, where a lighter shade of gray corresponds to a greater probability of departure. For this representation, we considered the Moon's surface as a rectangle of dimensions $[-180°, 180°] \times [-90°, 90°]$ in terms of longitude and latitude and we discretize it in small squares of $15° = 180°/12$ of side. For each nominal halo orbit, independently

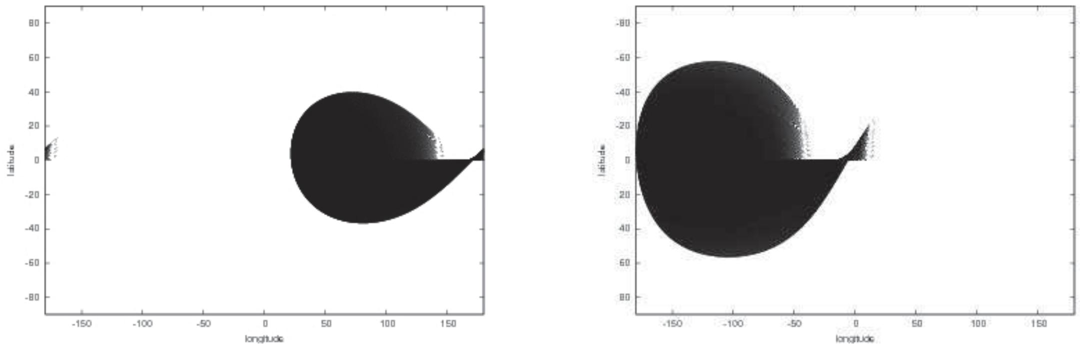

Figure 2.5: Longitude and latitude of the accessible arrival regions of the Moon associated with I class halo orbits considered around L_1 on the left, L_2 on the right. The two plots correspond to direct transfers.

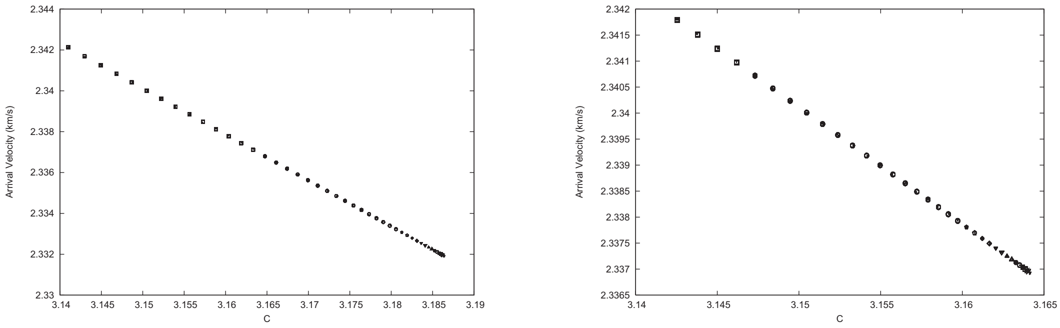

Figure 2.6: Modulus of the departure velocity (km/s) as a function of the Jacobi constant of the target halo orbit. On the left, the plot corresponds to the results obtained for the halo orbits considered around L_1; on the right, for the halo orbits around L_2.

of the number of minima needed, we compute the number of departures found in each of these squares and we weight this value taking into account the length of the arrival periodic orbit. Finally, the sum of the values obtained is divided by the total number of departures and by the area of the spherical square considered.

The above considerations are still valid if we talk about trajectories that lead to the Moon. In Fig. 2.5, we display the regions where we can land with direct transfers. Comparing Figs. 2.2 and 2.3 with Fig. 2.5, we note the symmetry already introduced in Section 1.2.2 occurring between the stable and the unstable invariant manifold.

Concerning the modulus of the velocity at the departure from the surface of the Moon, we note that in all the cases it is almost equal to the lunar escape velocity (about 2.375 km/s). This result follows from the conservation of the Jacobi integral, taking into account that all the orbits of the stable manifold of a certain halo orbit have the same value of the Jacobi constant as the halo orbit itself.

If $|\mathbf{v}|$ denotes the modulus of the velocity, the Jacobi integral can be written as

$$|\mathbf{v}|^2 = 2\Omega - C = (x^2+y^2) + 2\left(\frac{1-\mu}{r_1} + \frac{\mu}{r_2}\right) + (1-\mu)\,\mu - C. \tag{2.5}$$

When we move on the surface of the Moon, $r_2 = r_M$ is constant and, since x varies within $[\mu - 1 - r_M, \mu - 1 + r_M]$, the value of $r_1 = \sqrt{r_2^2 - 1 + 2\mu - 2x}$ goes from $r_M - 1$ to $r_M + 1$. If we compute the extrema of 2Ω we get that the variations of $|\mathbf{v}|$, for a fixed value of C, are of the order of 10^{-5} adimensional velocity units or, equivalently, of 10^{-2} m/s. As a consequence, the main change on the modulus of the departure velocity is due to the variation of the Jacobi constant along a given family of halo orbits.

In Fig. 2.6, we display how this modulus varies, as a function of the Jacobi constant, for the two families of halo orbits considered. As it can be seen from the plots, the maximum variations along the two families are of the order of 10 m/s.

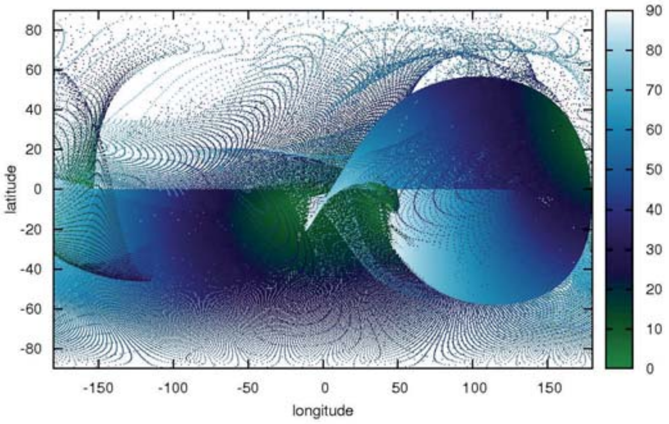

Figure 2.7: Longitude and latitude of departure as a function of the arrival angle. The arrival takes place on the I class halo family considered around L_2. Orthogonal departure is associated with 0°, tangential with 90°.

As mentioned before, we also compute the departure/arrival angle from the surface of the Moon. Because of the definition we assumed, it takes values between 0° (orthogonal departure/arrival) and 90° (tangent departure/arrival). If we consider direct and non-direct rescue trajectories and any halo orbit as target orbit, we find rescue trajectories with departure/arrival angles taking any value in $[0°, 90°]$ (see Fig. 2.7). In Fig. 2.8, we display the regions characterized by almost orthogonal departure, that is, from which we can leave with an angle less than 10°; in Fig. 2.9 the regions characterized by almost tangential landing. Indeed, we consider these two situations as the most natural to take off and land.

Furthermore, there exists a very large range of phases (more than one half of the full

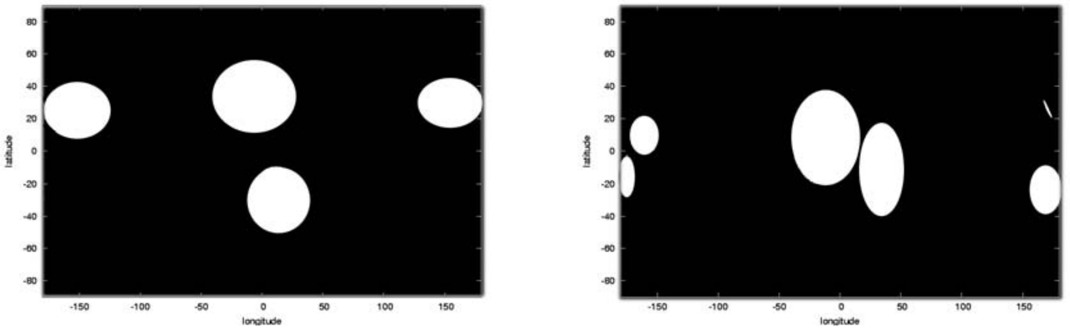

Figure 2.8: Regions of almost normal departure (the white ones) from the Moon to the halo family considered around L_1 (left) and L_2 (right). The two plots correspond to trajectories performing up to 3 loops around the Moon before reaching the halo orbit.

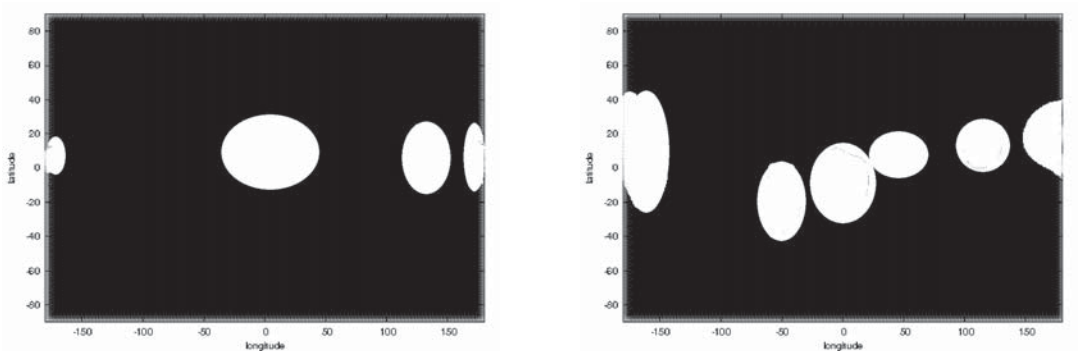

Figure 2.9: Regions of almost tangential arrival (the white ones) to the Moon from the halo family considered around L_1 (left) and L_2 (right). The two plots correspond to trajectories performing up to 3 loops around the Moon before reaching it.

range) which are not attained by rescue orbits. In Fig. 2.10 we show the behavior corresponding to direct landing on the Moon starting from a L_1 halo orbit. Increasing the number of loops the range of phases clearly increases, but not as much as to cover the whole interval $[0, 2\pi]$.

Concerning the transfer time, we recall first that a hyperbolic manifold is established on asymptotic trajectories. This means that to go from the Moon to a nominal libration point orbit (and vice versa) on such trajectories would take, in principle, an infinite time. More precisely, we consider the interval of time elapsed going from the initial conditions on the hyperbolic manifold, that is, about $70 - 90$ km from the given halo orbit, to the Moon's surface. In this way, both in the L_1 and in the L_2 case, direct orbits need approximately 10 days, while the non-direct ones need about 10 more days for each further loop.

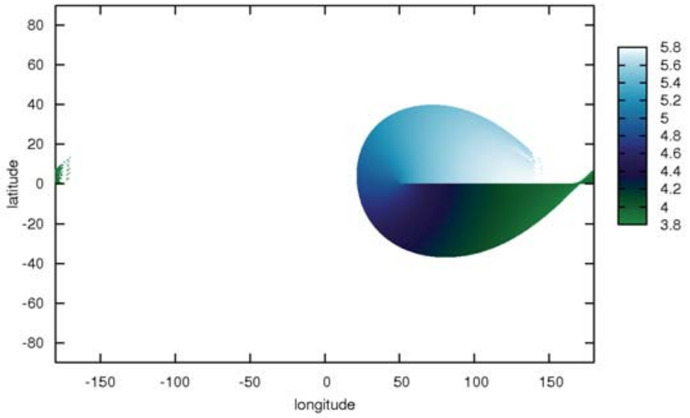

Figure 2.10: Longitude and latitude of landing as a function of the parameter along the periodic orbit. The departure takes place on the I class halo family around L_1.

2.3.2 Lissajous Arrival

To complete the study, we proceed to the numerical globalization of the stable invariant manifold associated with Lissajous orbits around L_1 and L_2. Looking to the crossing with the surface of the Moon we are able to determine the basic characteristics of the rescue transfer orbits. As in the previous case, we integrate backwards in time the trajectories on $\mathcal{W}^s$ starting close to the Lissajous orbit. If they reach the Moon, then we compute the longitude and the latitude of the intersection point, the velocity and the angle of arrival and the time of flight. Here, we skip the case associated with $\mathcal{W}^u$, as we have just understood the relationship existing between the two situations.

We stress that the main difference between this exploration and the one corresponding to the halo orbits is the amount of data to treat and the computational time. The reason is clear: in the halo case, for each equilibrium point and for a fixed energy level we have only two symmetric periodic orbits, now we have an infinite number of Lissajous orbits characterized by an in–plane and an out–of–plane amplitude, α_3 and α_4. In addition, for each pair of amplitudes we have two phases ϕ_1 and ϕ_2 to explore, in order to reach all the points of the orbit. To afford the consequent computational effort, we restrict the exploration to square Lissajous orbits ($\alpha_3 = \alpha_4$).

In particular, for L_1 we have $\alpha_3 = \alpha_4 \in [0.001, 0, 101]$ normalized units, that is, up to about 6500 km or $C \in [3.18598, 3.20034]$; for L_2 $\alpha_3 = \alpha_4 \in [0.001, 0, 171]$ normalized units, that is up to about 12000 km or $C \in [3.16356, 3.18416]$. These amplitudes are varied at step of 3×10^{-3}. Concerning ϕ_1 and ϕ_2, we pick up 300 equally spaced values in $[0, 2\pi]$ for both of them.

It is worth to recall that the hyperbolic invariant manifolds associated with halo orbits are 2–dimensional, so the corresponding intersection with the Moon's surface is a curve.

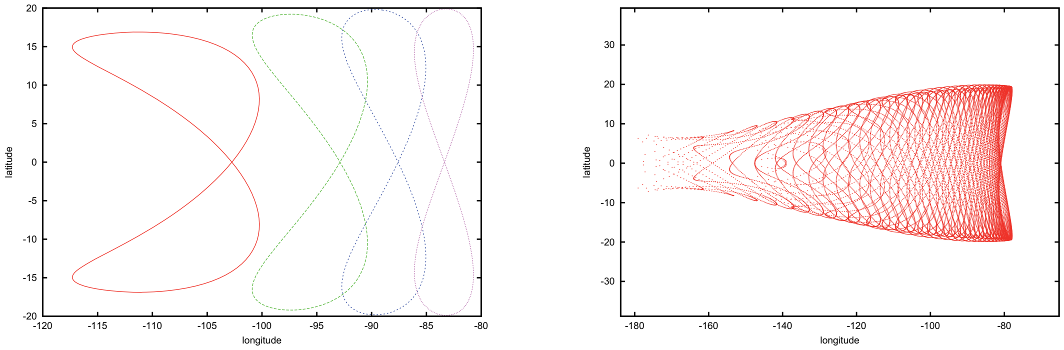

Figure 2.11: Departure region from the surface of the Moon associated with the square Lissajous orbit of amplitude equal to 0.09 normalized units ($\approx$ 6000 km) around the L_1 equilibrium point obtained from direct (without loops around the Moon) rescue orbits. See explanation in the text.

The hyperbolic invariant manifolds associated with Lissajous orbits are 3–dimensional, so their intersection with the surface of the Moon gives rise to 2–dimensional regions. For a given Lissajous orbit, that is, for fixed values of the amplitudes α_3 and α_4, its stable invariant manifold can be parametrised by the two phases ϕ_1, ϕ_2 and the time. Assume that this stable manifold reaches the Moon. If we fix one of the phases, say ϕ_1, and allow the other one to vary within $[0, 2\pi]$, the intersection with the surface of the Moon is a curve, which is closed if any value of ϕ_2 generates an orbit which gets the Moon's surface backwards in time. As we change the value of ϕ_1, the intersection curve changes both in shape and in position in the (λ, β) plane. Of course, it might happen that the intersection disappears for certain intervals of values of any of the phases. The envelope of all the intersection curves defines the boundary on the surface of the Moon of the 2–dimensional intersecting region associated with the stable invariant manifold of the Lissajous orbit.

In the left plot of Fig. 2.11, we show the intersection curves corresponding to toy-values of ϕ_1 for the stable invariant manifold associated with the square Lissajous orbit of amplitude equal to 0.09 normalized units ($\approx$ 6000 km) around the L_1 point. On the right, the whole region achieved by allowing ϕ_1 and ϕ_2 to vary in a continuous way in $[0, 2\pi]$. The curves are due to orbits that reach the Moon without performing any loop around it. The range of successful values for ϕ_1 is $(0.75, 2.1)$.

For the two kinds of Lissajous orbit that we consider as target, we find that most of the rescue can take place in a direct way if we aim at reaching the L_1 point, otherwise there exist more chances with two loops around the Moon. Moreover, the neighborhood of L_1 is attainable with any number of minima only departing from almost half of an equatorial strip of 40° in terms of latitude. In the L_2 case, the accessible region on the Moon is quite larger, though we do not have full coverage. This is shown in Fig. 2.12. Certainly, the reason of the two different behaviors resides on the wider range of amplitudes explored in the second case.

In Fig. 2.13, we display the allowed departure regions for direct trajectories, in the L_1

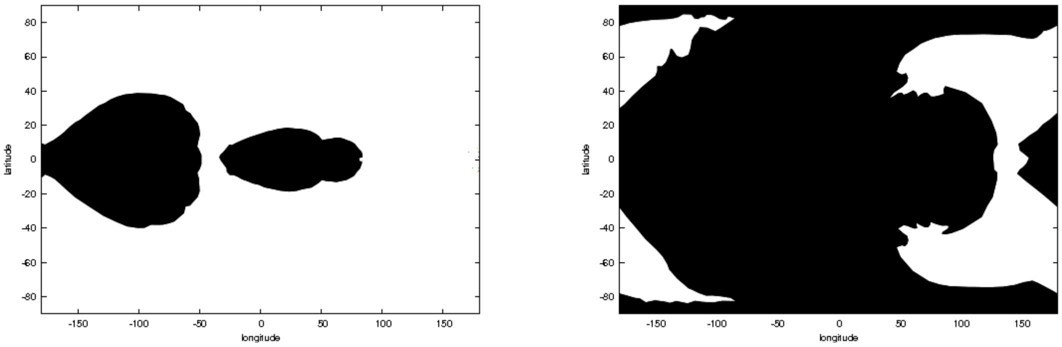

Figure 2.12: Regions (black) of allowed departure from the surface of the Moon, considering as target square Lissajous orbits and trajectories performing up to 5 loops around the Moon. On the left, the L_1 case; on the right, the L_2 one.

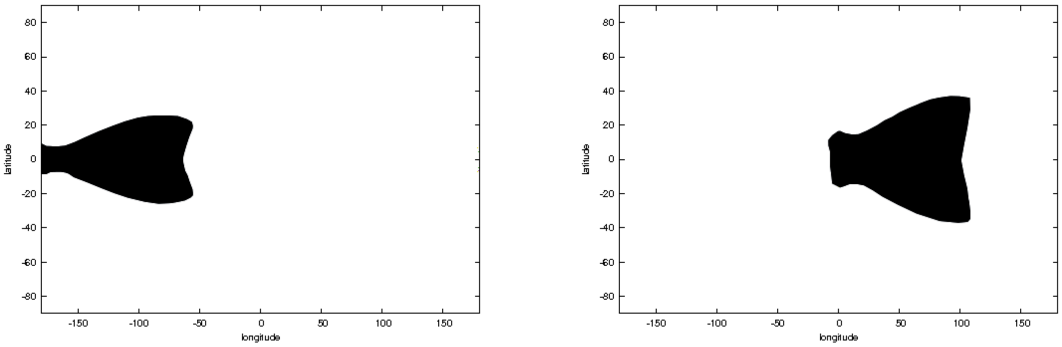

Figure 2.13: Regions (black) of allowed departure from the surface of the Moon, considering as target square Lissajous orbits around L_1 on the left, around L_2 on the right. We display here the case of direct rescue.

and in the L_2 case. Apart from the forbidden region, in the L_2 case we find a greater density of opportunities on the nearside of the Moon at equatorial latitudes.

As a further consideration, our simulation has revealed that the stable manifold arrives to the Moon only if the amplitudes $\alpha_3 = \alpha_4$ are big enough, this is: $\alpha_3 = \alpha_4 > 0.064$ (≈ 4000 km) for L_1 and $\alpha_3 = \alpha_4 > 0.075$ (≈ 5000 km) for L_2.

Concerning the phases, the greater the amplitude of the Lissajous the wider the interval of values ϕ_1 that give rise to rescue orbits.

By the same reasons described in the halo case, the departure velocity is almost the same for all the transfer orbits associated with a given Lissajous orbit and depends only on the value of the Jacobi constant. The behavior of the transfer time is quite analogous to that found for the halo orbits. The departure angle for direct rescue trajectories is represented in Fig. 2.14 as a function of the amplitudes $\alpha_3 = \alpha_4$ and one phase ϕ_1. Considering any number of loops, we do not find almost orthogonal departure in the L_1 case, while for L_2 the departure region characterized by an angle less than 10° is shown in Fig. 2.15.

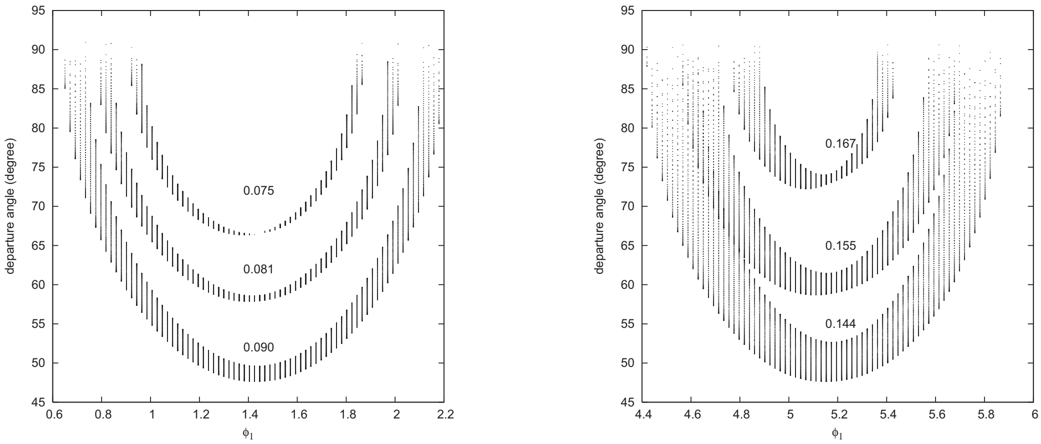

Figure 2.14: Departure angle for direct rescue trajectories in degrees as a function of the phase ϕ_1 (rad) and of the amplitude (normalized units) of the square Lissajous orbit. On the left, the L_1 case; on the right, the L_2 case.

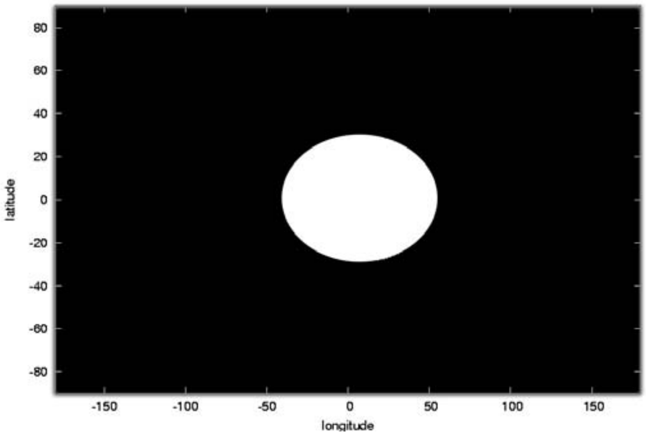

Figure 2.15: Region of almost normal departure (the white one) from the Moon to square Lissajous orbits around L_2. The plot corresponds to trajectories performing up to 5 loops around the Moon before reaching the quasi-periodic orbit.

2.4 Comments and Possible Developments

The dynamics corresponding to the hyperbolic invariant manifolds associated with the central invariant manifold of the collinear points L_1 and L_2 allows the design of rescue orbits from the surface of the Moon to a libration point orbit and vice versa, at least in the CR3BP model.

The results offer some distinctions depending on the type of LPO and of the transfer. In case of direct rescue orbits, there are large regions on the Moon's surface from which the landing and the take off is not possible, independently of the nominal LPO selected. For non-direct transfers, which are characterized by a longer transfer time, rescue can take place from much larger regions. In all the cases, the departure velocities are the lowest possible.

If we plan to set a lunar hub, it seems that the most suitable region is located at equatorial latitudes. Indeed, there $\mathcal{W}^u$ is able to provide tangential arrival and $\mathcal{W}^s$ orthogonal departure. However, we should allow for non-direct transfers in order to exploit the two dynamics, in the sense that the longitude-latitude coverage attained by the two manifolds overlaps only if the spacecraft can ring around the Moon at least once.

On the other hand, if indeed a relevant quantity of water ice will be confirmed at polar latitudes, we should refer to as great as possible amplitudes for the nominal LPO. This consideration holds especially if we are interested in Lissajous orbits, which represent a more flexible solution for a space station. Unfortunately, the order 25 Lindstedt–Poincaré semi-analytical approximation implemented does not permit to analyze the behavior corresponding to very large quasi-periodic orbits. Other techniques should be implemented, as example a Fourier parametrization (Gómez, Mondelo, 2001; Jorba, Ollé, 2004).

The main drawback of these rendezvous schemes might be the transfer time. A period of 10 days for a direct transfer is big compared with a standard Hohmann Earth – Moon connection. If we choose to perform one loop around the Moon, this value increases of about 10 days. It is something expected, due to the low-energy dynamics we are considering. An analogous time flow was already noticed by Baoyin, McInnes (2006).

TRANSFERS FROM A LOW EARTH ORBIT TO A LIBRATION POINT ORBIT

3

3.1 Introduction

As a natural continuation of the previous analysis, now we look for trajectories going from a nominal orbit around the Earth to a libration point orbit around either L_1 or L_2 of the Earth – Moon system. Our purpose is to provide a global picture of the dynamics driving these transfers, putting special emphasis on the role played by the geometry of the arrival orbits and the hyperbolic invariant manifolds. We will show that the distance existing between the Earth and the points on the manifold is crucial for a cheap connection.

As a matter of fact, in the Earth – Moon system the hyperbolic invariant manifolds associated with L_1/L_2 central orbits pass quite far from our planet, which means that the transfer can not take place using only these invariant structures. It is mandatory to design an additional leg that allows the spacecraft to join $\mathcal{W}^s$, which is the manifold we are interested in, as it approaches the neighborhood of L_1/L_2 forwards in time. At least two maneuvers are required: one to depart from the Low Earth Orbit (LEO) and one to insert either into the LPO or into one of the branches of its stable invariant manifold.

In this chapter we consider only square Lissajous orbits as target. While in the Sun – Earth framework the practical application of this central type of solutions is consolidated (just think about the recent Herschel and Planck missions), in the Earth – Moon reference system there is not any exploitation yet.

From our point of view, there exist several reasons to plan a mission based on Lissajous orbits. First of all, this 2-parameter family of solutions imposes less constraints to the mission designer than the widely used halo orbits, essentially because the in–plane and the out–of–plane amplitudes can be chosen independently one from the other. As a further advantage, the occultation avoidance problem can be solved in a non-expensive way: following Canalias, Cobos, Masdemont (2003) and Renk (2009) it is possible to skip out the exclusion zone by means of either a phase jump or synchronization. Finally, a methodology for transfers involving quasi-periodic orbits can be extended and applied to the periodic orbit case.

Other authors have considered the same problem with different methodologies. Rausch (2005) and Parker (2007) fixed as arrival locations halo orbits around the point L_1 in

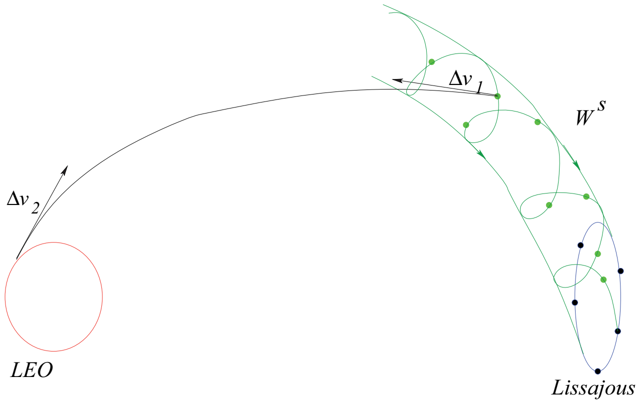

Figure 3.1: Sketch of the procedure implemented. In a backwards integration, we depart from a nominal Lissajous orbit and we get to a sphere around the Earth of given radius (LEO sphere).

the Earth – Moon system. The first author used a shooting technique to construct a continuous arc linking two given points in a fixed time of flight. Parker computed a 2-maneuvers connection by means of a Two – Body Problem (2BP) approximation refined including the gravitational effect of the Moon. Renk, Hechler (2008) exploited optimization techniques in order to transfer from a nominal LEO to a LPO (halo and Lissajous) either around L_1 or L_2. The trajectories computed follow the escape directions associated with the LPO and may perform a lunar fly-by. Gordon (2008) focused his work on LEO-LPO around the point L_2. In his approach, a differential correction procedure is used to meet some constraints at the departure and at the insertion either into a planar Lyapunov orbit or into a halo orbit.

3.2 2–Manoeuvres Transfers

As just mentioned, our aim is to establish a transfer to go from a given LEO to a nominal square Lissajous orbit either around L_1 or L_2 in the Earth – Moon system. We assume to be able to perform two maneuvers and to exploit one of the branches of the stable invariant manifold associated with the arrival orbit.

The procedure implemented can be sketched as follows (see Fig. 3.1).

1. We choose the arrival orbit, that is, the amplitude $\alpha_3 = \alpha_4$, and we compute the initial conditions on the proper branch of the corresponding stable invariant manifold by means of the order 25 Lindstedt–Poincaré series expansion (1.10). This is, we set $\alpha_2 \neq 0$ and determine the initial conditions associated with equally spaced values of the phases ϕ_1 and ϕ_2 both inside the range $[0, 2\pi]$.

2. We integrate each initial condition backwards in time up to a certain point (that will be specified later) defining $t = 0$ when the x component of the trajectory fulfills a given requirement (generally $x > x_{min}$, where x_{min} depends on the amplitude of

the Lissajous orbit). In this way, we intend to start our computation at a distance of about 100 km from the Lissajous quasi-periodic orbit.

3. Then we perform a first maneuver, say Δv_1, to change the energy of the particle and the direction of its motion. With Δv_1 we aim at reaching (backwards in time) a sphere of radius $R = R_{Earth} + h_{LEO}$ (LEO sphere), assuming $R_{Earth} = 6378.14$ km and h_{LEO} to be a given altitude for a set of LEOs.

4. If, after performing the first velocity correction Δv_1, we obtain a trajectory which reaches the LEO sphere, then a second maneuver is needed, say Δv_2. This is done assuming the velocity on the sphere, say v_c, to be constant and given by the 2BP approximation. In particular, $v_c = \sqrt{\mu_2/R}$ where $\mu_2 = 1-\mu$ is the mass parameter for the 2BP (recall that, due to the adimensional set of units adopted, the universal gravitational constant is unitary).

   Let $\mathbf{v}$ be the velocity of the spacecraft at the arrival to the LEO, then

   $$\Delta v_2 = \sqrt{||\mathbf{v}||^2 + v_c^2 - 2||\mathbf{v}||v_c \cos(0.5\pi - \vartheta)}. \tag{3.1}$$

   Here ϑ is the angle between v and the normal to the LEO sphere, say ∇G, where $G = (x-\mu)^2 + (y)^2 + (z)^2 - R^2$. It is computed as in (2.4).

5. For each initial condition considered on the stable invariant manifold, we look for the minimum $\Delta v_{tot} = \Delta v_1 + \Delta v_2$ which guarantees the connection. To this end, we implement a differential correction procedure with respect to Δv_1 in order to make Δv_2 minimum, that is, $\vartheta = 0.5\pi$, as stated by (3.1).

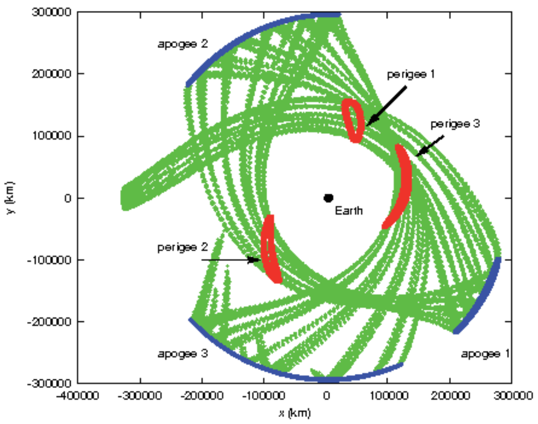

Figure 3.2: The negative branch of the stable invariant manifold associated with the square Lissajous orbit of $\alpha_3 = 0.09$ normalized units around the point L_1 in the Earth – Moon system. The central dot represents the Earth; the points labeled as perigee are the points on the manifold which correspond to a minimum of the distance to the Earth function; the points labeled as apogee are the ones which correspond to a maximum.

6. Finally, if we reach the LEO sphere, we compute the longitude β and the latitude λ corresponding to the point obtained, namely,

$$\beta = \arctan \frac{y}{x-\mu}, \qquad \lambda = \arctan \frac{z}{\sqrt{(x-\mu)^2+y^2}}.$$

   They give information on the inclination characterizing the LEOs that can be considered with our technique.

We remark that we can decide to apply Δv_1 at a certain epoch or at a certain distance from the Earth. In the second case, we refer as *perigee* and *apogee* the points at which the distance to the Earth function attains a minimum and a maximum, respectively (see Fig. 3.2). Also, we can achieve the transfer by inserting directly into the Lissajous orbit without using the stable invariant manifold. In this case, Δv_1 is applied to the initial conditions given by the Lindstedt–Poincaré expansion setting $\alpha_1 = \alpha_2 = 0$.

3.2.1 First Approximation

As a first approximation for Δv_1 we consider a Hohmann-like transfer between the ellipse which osculates the point chosen on the manifold and a co-planar circular orbit with radius R around the Earth.

Let us start by recalling how a point in the synodical reference system with origin at the Earth – Moon barycenter is seen in the sidereal coordinate system whose reference plane is the Earth – Moon orbital plane and origin is set at the Earth, this is, how to move from $(x^{syn}, y^{syn}, z^{syn}, \dot{x}^{syn}, \dot{y}^{syn}, \dot{z}^{syn})$ to $(x^{sid}, y^{sid}, z^{sid}, \dot{x}^{sid}, \dot{y}^{sid}, \dot{z}^{sid})$. In the CR3BP adimensional units, we have

$$\begin{pmatrix} x^{sid} \\ y^{sid} \\ z^{sid} \end{pmatrix} = \mathcal{R} \begin{pmatrix} x^{syn} - \mu \\ y^{syn} \\ z^{syn} \end{pmatrix}, \tag{3.2}$$

and

$$\begin{pmatrix} \dot{x}^{sid} \\ \dot{y}^{sid} \\ \dot{z}^{sid} \end{pmatrix} = \mathcal{R} \begin{pmatrix} \dot{x}^{syn} \\ \dot{y}^{syn} \\ \dot{z}^{syn} \end{pmatrix} + \dot{\mathcal{R}} \begin{pmatrix} x^{syn} - \mu \\ y^{syn} \\ z^{syn} \end{pmatrix}, \tag{3.3}$$

where

$$\mathcal{R} = \begin{pmatrix} \cos(t) & -\sin(t) & 0 \\ \sin(t) & \cos(t) & 0 \\ 0 & 0 & 1 \end{pmatrix},$$

and $\dot{\mathcal{R}}$ is the derivative of $\mathcal{R}$ with respect to t.

Given these equations, if we consider a certain point on the hyperbolic invariant manifold in synodical coordinates, we can always look at it as a point of the 2BP in sidereal coordinates and compute the corresponding orbital elements, provided a far enough

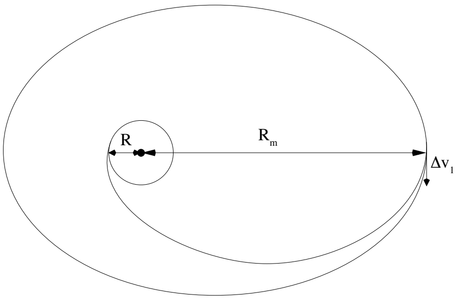

Figure 3.3: Hohmann-like transfer considered as initial guess for the differential procedure implemented.

distance from the primary we would like to neglect (the Moon in our case).

The maneuver to be computed in the inertial framework is given by

$$\Delta v_1 = \sqrt{2\frac{\mu_2}{R_m} - 2\frac{\mu_2}{R_m + R}} - \sqrt{2\frac{\mu_2}{R_m} - \frac{\mu_2}{a}}, \tag{3.4}$$

where R_m is the distance from the point on the manifold to the Earth and a is the semi-major axis of the osculating ellipse (see Fig. 3.3).

In particular, if $\mathbf{v}_{old}^{sid}$ is the inertial velocity corresponding to the point on the manifold, we apply to it a tangential maneuver Δv_1 which results in $\mathbf{v}_{new}^{sid}$, namely,

$$(\mathbf{v}_{new}^{sid})_i = (\mathbf{v}_{old}^{sid})_i + \Delta v_1 \frac{(\mathbf{v}_{old}^{sid})_i}{||\mathbf{v}_{old}^{sid}||}, \qquad i = 1, 2, 3. \tag{3.5}$$

The last step is to apply the inverse transformation of (3.3) in order to obtain from $\mathbf{v}_{new}^{sid}$ a first approximation for the velocity at the beginning of the transfer path in the CR3BP reference frame, say $\mathbf{v}_{new}^{syn}$.

In turn, the procedure can be summarized as

$$\mathbf{v}_{old}^{syn} \quad \xrightarrow{(3.3)} \quad \mathbf{v}_{old}^{sid} \quad \xrightarrow{\Delta v_1} \quad \mathbf{v}_{new}^{sid} \quad \xrightarrow{(3.3)^{-1}} \quad \mathbf{v}_{new}^{syn}.$$

We stress that while $\mathbf{v}_{new}^{sid}$ and $\mathbf{v}_{old}^{sid}$ are parallel, this is not true in general for $\mathbf{v}_{new}^{syn}$ and $\mathbf{v}_{old}^{syn}$. Indeed, by considering a rotating reference system we have to account for additional components due to the Coriolis force.

3.2.2 Differential Correction

The maneuver (3.1) is minimum if the following condition is satisfied at the LEO:

$$g := \mathbf{r}^{sid} \cdot \mathbf{v}^{sid} = \mathbf{v} \cdot \nabla G = 0. \tag{3.6}$$

Because of this, starting from the point on the manifold $(\mathbf{r}^{syn}, \mathbf{v}^{syn}_{new})$ we integrate the equations of motion of the CR3BP up to fulfill the requirement above. At this step, if the distance between the spacecraft and the Earth is not the desired one, we apply a differential correction procedure with respect to Δv_1.

Let $\mathbf{X}^{syn}_0 \equiv (\mathbf{r}^{syn}, \mathbf{v}^{syn}_{new})$ be the initial condition on the Hohmann-like trajectory and $\mathbf{X}^{syn}_f$ the point computed when $g = 0$. We implement the Newton's method in order to obtain also $G = 0$, namely,

$$\begin{aligned} \mathbf{DG} \cdot \mathbf{\Delta X}^{sid}_0 &= \left[\frac{\partial G}{\partial \mathbf{X}^{syn}_f} \cdot (\Phi + \mathbf{F} \cdot \mathbf{Dt}) \cdot \frac{\partial \mathbf{X}^{syn}_0}{\partial \mathbf{X}^{sid}_0}\right] \cdot \mathbf{\Delta X}^{sid}_0 \\ &= -G, \end{aligned} \tag{3.7}$$

where $\Phi = \frac{\partial \mathbf{X}^{syn}_f}{\partial \mathbf{X}^{syn}_0}$ is the variational matrix, $\mathbf{F} = \frac{\partial \mathbf{X}^{syn}_f}{\partial t_f}$ is the CR3BP vector field, $\mathbf{Dt} = \frac{\partial t_f}{\partial \mathbf{X}^{syn}_0} = -\frac{\mathbf{Dg} \cdot \Phi}{\mathbf{Dg} \cdot \mathbf{F}}$, $\mathbf{\Delta X}^{sid}_0$ is the correction we apply to the initial conditions in the sideral reference system and

$$\frac{\partial \mathbf{X}^{syn}_0}{\partial \mathbf{X}^{sid}_0} = \begin{pmatrix} 1 & 0 & 0 & 0 & 0 & 0 \\ 0 & 1 & 0 & 0 & 0 & 0 \\ 0 & 0 & 1 & 0 & 0 & 0 \\ 0 & 1 & 0 & 1 & 0 & 0 \\ -1 & 0 & 0 & 0 & 1 & 0 \\ 0 & 0 & 0 & 0 & 0 & 1 \end{pmatrix}. \tag{3.8}$$

Notice that, since the initial position on the manifold is fixed and because of (3.5), we need to change just the value of Δv_1.

3.3 Numerical Results

We implement the above procedure to reach Lissajous orbits around either the point L_1 and L_2. Due to the presence of the Moon in the latter situation, we deal with quite different results. In particular, we decide to analyze the branch of $\mathcal{W}^s(L_2)$ which does not approach directly the second primary and thus the behavior of the dynamical tube with respect to the Earth is not as relevant as in the former case.

We report the results corresponding to the two equilibria one independently from the other.

3.3.1 L_1 Lissajous Orbits

We begin by considering to depart from a LEO of altitude $h_{LEO} = 360$ km and to arrive to square Lissajous orbits of various sizes around the equilibrium point L_1. In particular, we take amplitudes $\alpha_3 = \alpha_4 = 0.01$, 0.03, 0.06 and 0.09 normalized units, which correspond to 600, 1700, 3500 and 6000 km, respectively. The negative branch of the stable invariant manifold associated with these quasi-periodic orbits is the most

Lissajous amplitude	**minimum d_{Earth}**	**maximum d_{Earth}**
600	120286.1	294330.0
1700	114278.9	295327.4
3500	105986.8	296946.1
6000	98279.1	298769.5

Table 3.1: Minimum and maximum altitude (km) with respect to the center of the Earth attained in 40 days by the negative branch of the stable invariant manifold associated with a square Lissajous orbit of given amplitude (km).

suitable to our purpose (compare Figs. 1.9 and 3.2). From Fig. 3.2 we see that the distance to the Earth function, say d_{Earth}, attains several local minima and maxima in the branch of the manifold considered. In the first exploration, we take these extrema as insertion locations, as they are expected to be also extrema of the total Δv cost. Later on, we study the possibility of injecting into any point on the manifold and also to vary the value of h_{LEO}. We notice that d_{Earth} is R_m introduced in (3.4).

Perigees and Apogees

To analyze the transfers associated with perigees and apogees, we take 100 values of ϕ_1 and 100 values of ϕ_2 obtaining 10000 initial conditions on the negative branch of $\mathcal{W}^s$. In Tab. 3.1 we show the minimum and maximum distance that this branch of the stable invariant manifold associated with a given square Lissajous orbit can attain in about 40

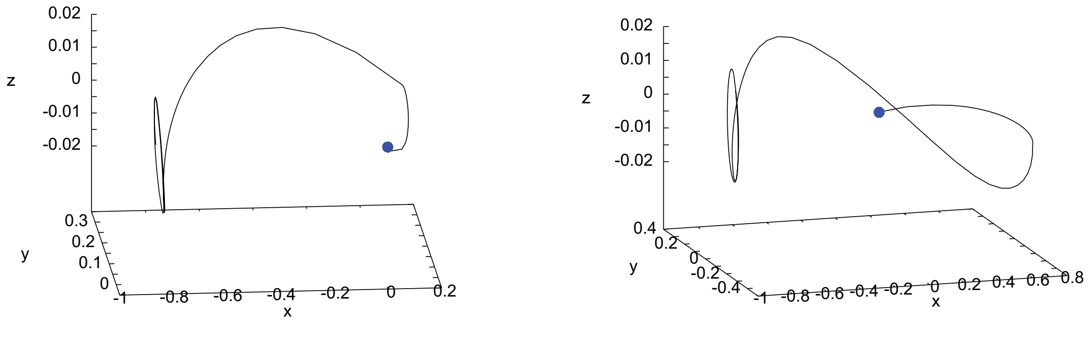

Figure 3.4: Examples of transfers obtained in the CR3BP synodical reference system with adimensional units. LEO of $h_{LEO} = 360$ km; arrival Lissajous orbit of amplitudes $\alpha_3 = \alpha_4 = 0.09$ normalized units (≈ 6000 km) around the point L_1 of the Earth – Moon system. Left: insertion into one of the perigees of the corresponding stable invariant manifold. Right: insertion into one of the apogees.

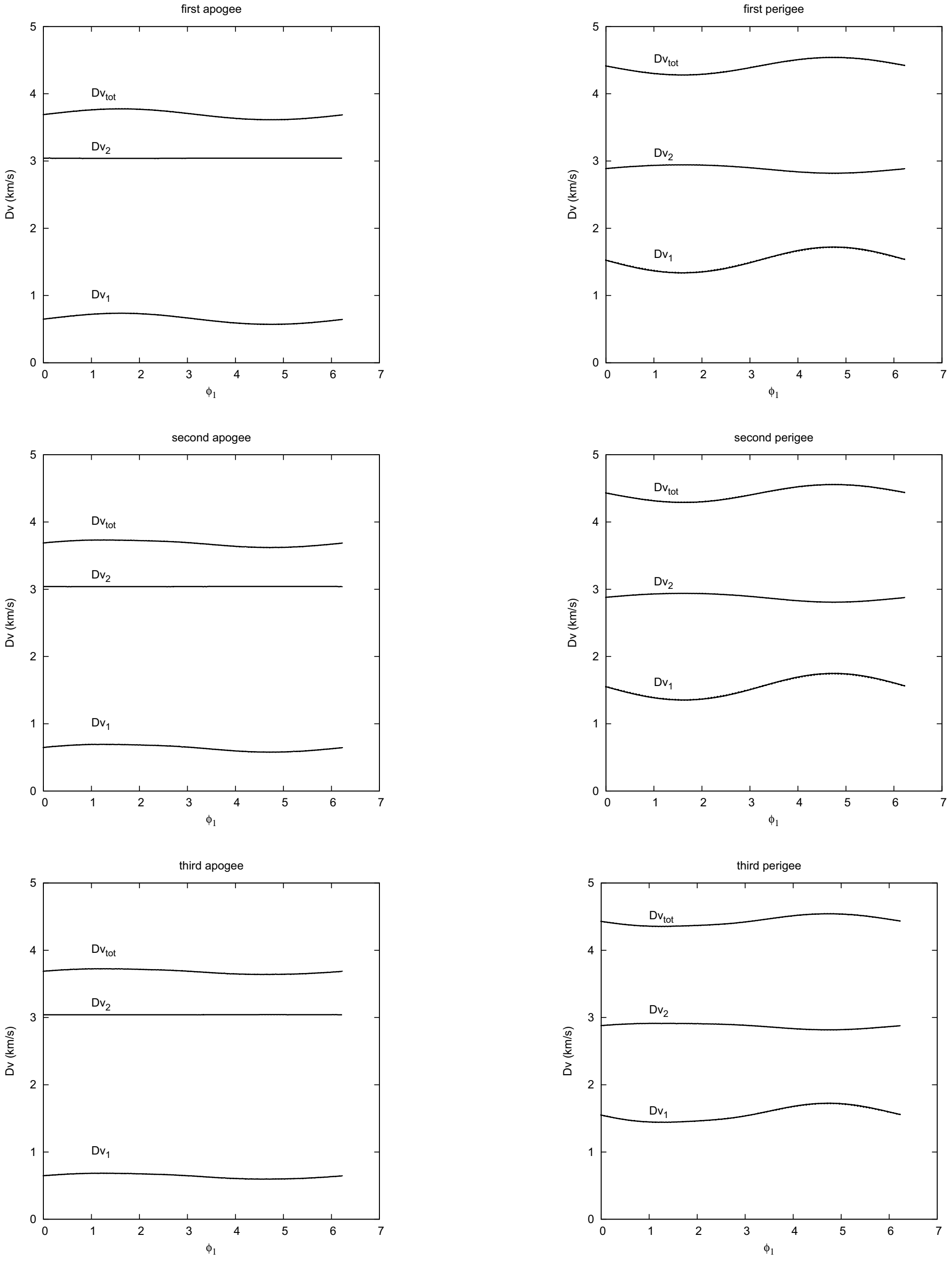

Figure 3.5: As a function of ϕ_1, the cost (km/s) of the first maneuver (lower curve), of the second one (central curve) and the total cost (upper curve) for transfers between LEOs of $h_{LEO} = 360$ km and the first three **apogees** (left) and **perigees** (right) of the negative branch of the stable invariant manifold associated with the square Lissajous orbit of $\alpha_3 = 0.09$ normalized units (≈ 6000 km) around the point L_1 in the Earth – Moon system.

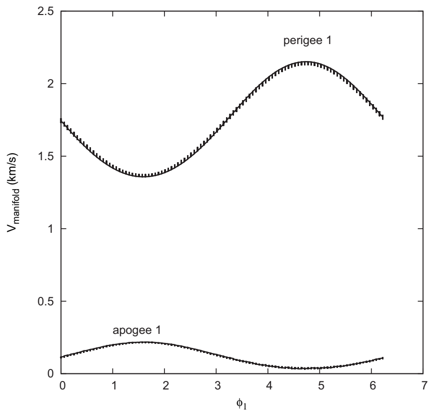

Figure 3.6: Modulus of the velocity (km/s) on the manifold as a function of ϕ_1. Here, we consider the first apogee and the first perigee associated with the negative branch of the stable invariant manifold corresponding to the square Lissajous orbit of $\alpha_3 = 0.09$ normalized units (≈ 6000 km) around the point L_1 in the Earth – Moon system.

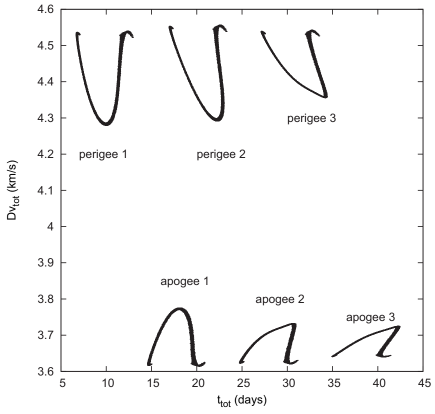

Figure 3.7: Total cost (km/s) of the transfer as a function of the total time (days), that is, the time spent on the manifold plus the time from the LEO to the manifold. The results are associated with apogees and perigees on the negative branch of the stable invariant manifold corresponding to the square Lissajous orbit of $\alpha_3 = 0.09$ normalized units ($\approx$ 6000 km) around the point L_1 in the Earth – Moon system.

days. In Fig. 3.4 we show two of the transfers obtained, one arriving to a perigee of $\mathcal{W}^s$ and one to an apogee.

From these simulations, it turns out that the most expensive maneuver takes place at the LEO (see Fig. 3.5). This is something expected if we think that we depart from the neighborhood of the Earth with a speed close to the velocity of escape of the Earth ($\approx$ 11.2 km/s) and the velocity on a LEO is constant ($\approx$ 7.7 km/s in the case considered).

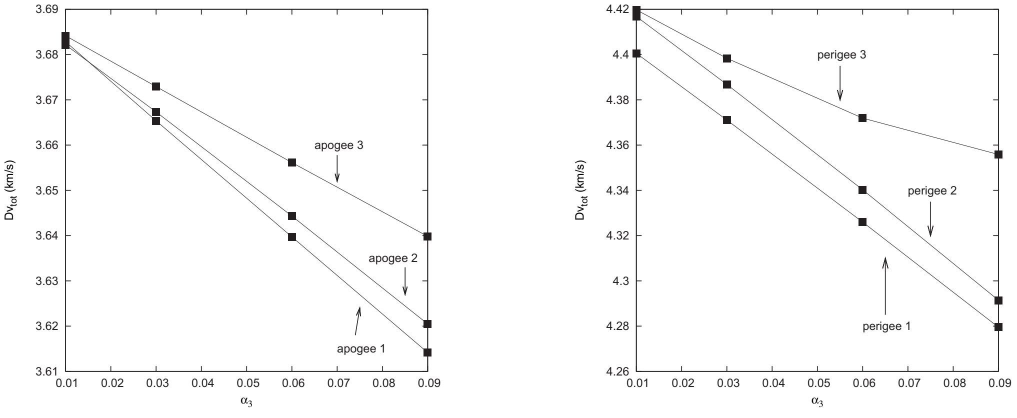

Figure 3.8: Transfer total cost (km/s) as a function of the size (normalized units) of the arrival Lissajous orbits around the point L_1 in the Earth – Moon system. Left: the apogee case; right: the perigee one.

Moreover, the apogees seem to be more convenient in order to obtain cheaper transfers in terms of total Δv. Looking to Fig. 3.5, we can realize that getting further from the Earth we save almost 0.7 km/s. A similar behavior can be appreciated when considering different maxima/minima. We notice that the modulus of the velocity on the manifold at the apogees is smaller than the one associated with perigees (see Fig. 3.6). In a 2BP framework, this means that in the first case we are close to the apogee of the osculating ellipse and to the perigee in the other one.

In Fig. 3.7 we display the total Δv cost as a function of the total transfer time, that is, the time spent on the manifold plus the time on the Hohmann-like leg. Going from the LEO to the manifold requires about 3 days if inserting into an apogee and about 1 day if inserting into a perigee.

If we consider arrival orbits of various amplitudes and different apogees/perigees, we obtain as minimum total cost the value showed in Tab. 3.2. In the same table, they are displayed the two maneuvers performed and the time corresponding to go from the LEO to the manifold. The best path computed corresponds to the first apogee of the stable manifold associated with the square Lissajous orbit of $\alpha_3 = 0.09$ normalized units ($\approx$ 6000 km): it takes about 3.4 days on the Hohmann-like leg and the total change in velocity is of about 3.6 km/s. As general finding, the larger the nominal orbit, the cheaper and longer the transfer. From Fig. 3.8, it can be inferred that the total cost of the transfer follows a behavior which is almost linear with respect to the size of the Lissajous arrival orbit.

In Tab. 3.3 we show the maximum inclinations with respect to the Earth – Moon orbital plane of the LEOs the whole procedure allows us to depart from. We notice that, while arriving to a perigee is possible only from a very narrow range, there exist many chances to reach an apogee. Moreover, the greater the amplitude of the target Lissajous orbit, the wider the interval of inclinations that can be considered.

$\alpha_3 = \alpha_4 = \mathbf{0.09}$ (6000 km)

arrival	$\mathbf{\Delta v_1}$	$\mathbf{\Delta v_2}$	$\mathbf{\Delta v_{tot}}$	**TOF**
apogee 1	0.5717	3.0425	3.6142	3.4292
apogee 2	0.5781	3.0424	3.6205	3.3901
apogee 3	0.5972	3.0425	3.6397	3.3912
perigee 1	1.3374	2.9421	4.2795	1.3931
perigee 2	1.3533	2.9381	4.2914	1.3544
perigee 3	1.4426	2.9132	4.3558	1.1638

$\alpha_3 = \alpha_4 = \mathbf{0.06}$ (3500 km)

arrival	$\mathbf{\Delta v_1}$	$\mathbf{\Delta v_2}$	$\mathbf{\Delta v_{tot}}$	**TOF**
apogee 1	0.5979	3.0417	3.6396	3.4001
apogee 2	0.6028	3.0415	3.6443	3.3549
apogee 3	0.6147	3.0414	3.6561	3.3479
perigee 1	1.4018	2.9242	4.3260	1.2417
perigee 2	1.4213	2.9189	4.3402	1.2032
perigee 3	1.4663	2.9056	4.3719	1.1125

$\alpha_3 = \alpha_4 = \mathbf{0.03}$ (1700 km)

arrival	$\mathbf{\Delta v_1}$	$\mathbf{\Delta v_2}$	$\mathbf{\Delta v_{tot}}$	**TOF**
apogee 1	0.6243	3.0411	3.6653	3.3721
apogee 2	0.6267	3.0406	3.6673	3.3228
apogee 3	0.6323	3.0405	3.6728	3.3158
perigee 1	1.4656	2.9054	4.3710	1.1108
perigee 2	1.4878	2.8989	4.3867	1.0719
perigee 3	1.5051	2.8933	4.3984	1.0393

$\alpha_3 = \alpha_4 = \mathbf{0.01}$ (600 km)

arrival	$\mathbf{\Delta v_1}$	$\mathbf{\Delta v_2}$	$\mathbf{\Delta v_{tot}}$	**TOF**
apogee 1	0.6421	3.0407	3.6828	3.3571
apogee 2	0.6420	3.0401	3.6821	3.3041
apogee 3	0.6440	3.0401	3.6841	3.3018
perigee 1	1.5083	2.8923	4.4006	1.0326
perigee 2	1.5317	2.8851	4.4168	0.9941
perigee 3	1.5365	2.8832	4.4197	0.9846

Table 3.2: Minimum total cost (km/s), maneuvers performed (km/s) and time of flight (days) on the Hohmann-like leg to go from LEOs of $h_{LEO} = 360$ km to the stable invariant manifold associated with different Lissajous orbits. From the top, $\alpha_3 = 0.09$, $\alpha_3 = 0.06$, $\alpha_3 = 0.03$, $\alpha_3 = 0.01$ normalized units around the point L_1 in the Earth – Moon system.

Lissajous amplitude	arrival	maximum i
600	apogee	3.37°
1700	apogee	12.70°
3500	apogee	47.23°
6000	apogee	69.61°
600	perigee	0.14°
1700	perigee	0.41°
3500	perigee	0.89°
6000	perigee	1.60°

Table 3.3: Maximum inclination (degree) with respect to Earth – Moon orbital plane of the LEOs, that can be considered with our procedure. The perigees and apogees taken as target belong to the negative branch of the stable invariant manifold associated with square Lissajous orbits of given amplitude (km).

Different Insertion Locations

With this outcome in mind we extend the results to the case where the Δv_1 maneuver is performed at any point along the manifold. To this end we take insertion points on the stable invariant manifold every $\Delta t = 0.01$ adimensional units (about 1 hour) up to $t = 9$ normalized units (about 40 days), starting from 20×20 initial conditions along the Lissajous orbit.

In a first step we look for the minimum Δv_{tot} corresponding to each instant of time. This is displayed in Fig. 3.9. The oscillations that appear in such curves are related to the distance, d_{Earth}, between the Earth and the point on the manifold which corresponds to a given value of time. For the biggest Lissajous orbit analyzed the cheapest transfer requires about 12 days of journey along the stable invariant manifold.

To perform a deeper analysis we fix the value of ϕ_1 obtaining the behavior showed in Fig. 3.10. We notice that while Δv_2, the maneuver at the LEO, is almost constant whenever we insert into the manifold, Δv_1 is driven by the Earth-manifold distance. In turn, Δv_1 controls the behavior of Δv_{tot} and maxima of Δv_1 are associated with minima of d_{Earth}. We observe that the cost of the first maneuver turns is minimum when the velocity of insertion into the manifold and the velocity associated with the manifold are aligned but with opposite directions.

If we fix both ϕ_1 and ϕ_2, that is, we examine the behavior of a given trajectory, we notice that the minimum Δv_{tot} over the whole time span takes place at an apogee. This is a further confirmation of the role played by d_{Earth}.

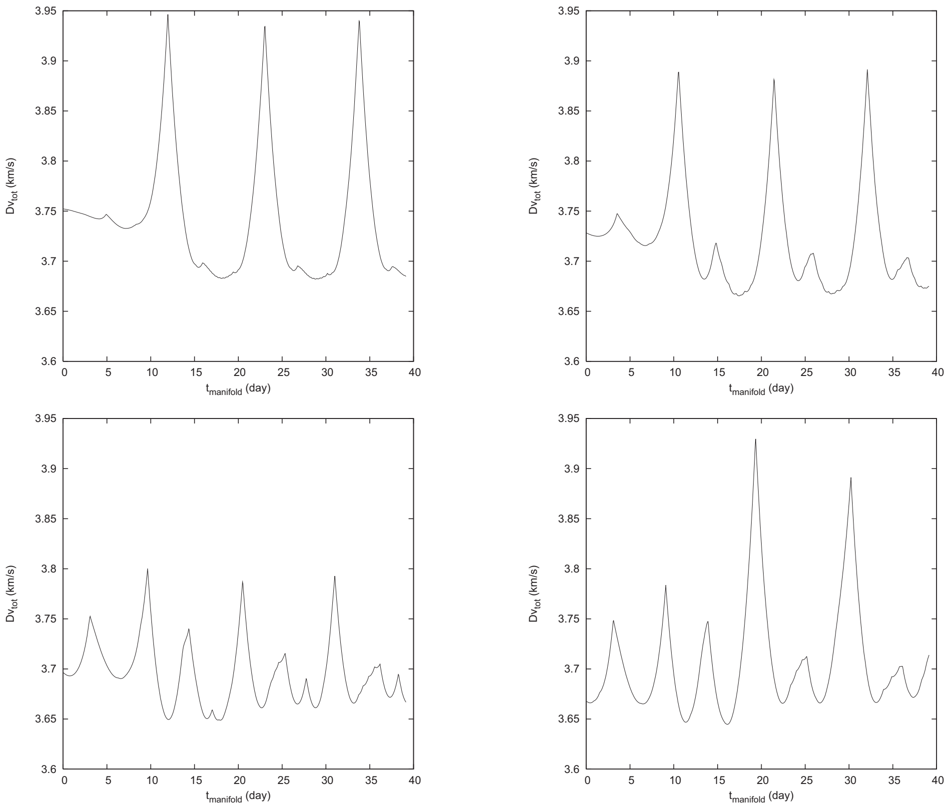

Figure 3.9: Minimum Δv_{tot} (km/s) found for each t (days) considered in the 20×20 mesh of points set. On the top left, Lissajous orbit of $\alpha_3 = 0.01$; on the top right, $\alpha_3 = 0.03$; on the bottom left, $\alpha_3 = 0.06$; on the bottom right, $\alpha_3 = 0.09$ normalized units.

Further Considerations

If we extend the simulations just explained to LEOs of different altitudes, we are able to reproduce the same outcome as above. The only thing we can notice is that the higher the altitude the smaller both maneuvers Δv_1 and Δv_2, as expected. This is showed in Fig. 3.11.

Finally, we construct transfers that do not exploit the stable invariant manifold, this is, the procedure is applied directly to the Lissajous nominal orbits. As it could also be deduced from Fig. 3.9, we cannot detect any improvement, apart from the total time of flight, which is now of about 4 days. The behavior of the total cost now varies according to the size of the Lissajous arrival orbit, but in general is higher than the one obtained at the apogees, apart from small ranges of (ϕ_1, ϕ_2).

The total outcome is coherent with the simulations done by Parker (2007). For fast transfers he observed that the smallest velocity corrections are associated with the points on the manifold which lay at the greatest distance with respect to the Earth. In other words, he found that the best transfers take place at the apogee of the branch of the

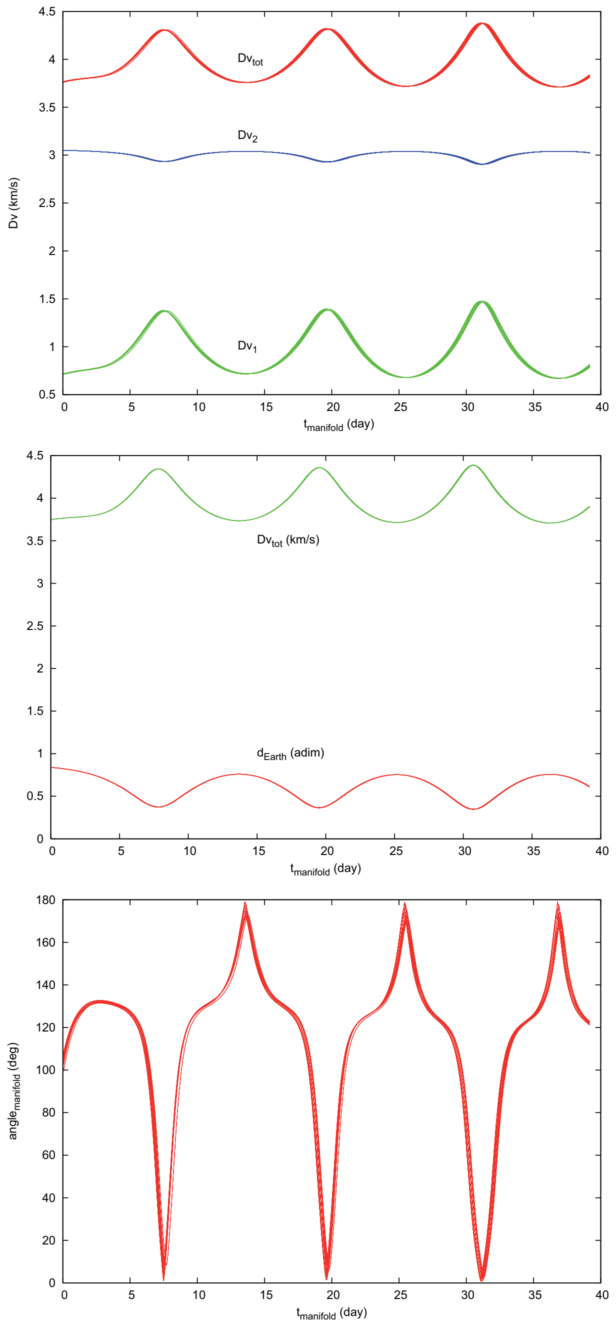

Figure 3.10: As a function of the value of time corresponding to the insertion into the manifold, the behavior of Δv_1, Δv_2 and Δv_{tot} (top), of Δv_{tot} and d_{Earth} (middle) and of the angle between the velocity on the manifold and the velocity of insertion into the manifold (bottom). We fix the value of ϕ_1 as $\phi_1 = 7\pi/10$ and we consider the negative branch of the stable invariant manifold corresponding to the square Lissajous orbit of $\alpha_3 = \alpha_4 = 0.09$ normalized units (≈ 6000 km) around the point L_1 in the Earth – Moon system.

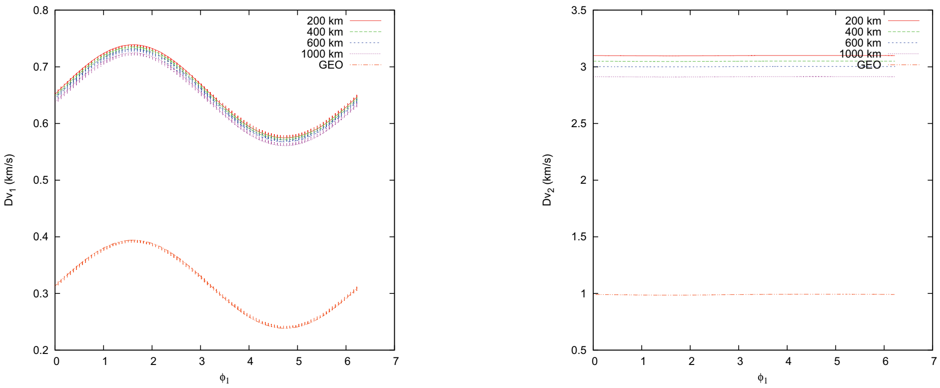

Figure 3.11: Behavior of Δv_1 and Δv_2 (km/s) as a function of ϕ_1 for departure LEOs of different altitudes with respect to the surface of the Earth and for a GEO. First apogee of the negative branch of the stable invariant manifold corresponding to the square Lissajous orbit of $\alpha_3 = 0.09$ normalized units (≈ 6000 km) around the point L_1 in the Earth – Moon system.

stable manifold of the chosen halo orbit. The cheapest value he got for the perigee scenario is a little lower than the ours (about 4.14 km/s for a fixed central orbit), while for the open-point scenario his least expensive cost (about 3.62 km/s) is almost the same as our 3.61 km/s. We recall that he computed even better connections by exploring a very wide range of amplitudes for the nominal halo orbit.

On the other hand, we have obtained better results than those of Rausch (2005) in what concerns the insertion into the manifold, but not with respect to the direct transfers to the L_1 orbits. Indeed, he found that the best connections arrive to the halo orbits, both in what refers to the time of flight and the cost of the maneuvers.

3.3.2 L_2 Lissajous Orbits

As the point L_2 stays beyond the Moon, there exist several manners in which our problem can be addressed. If we consider the inner branch of the stable invariant manifold, this is, the one which goes directly toward the Earth passing by the Moon, it would be possible to establish the transfer by means of heteroclinic connections and also by achieving lunar gravity assists. The first approach essentially reduces to the case treated before (see Fig. 3.12), apart from the maneuver (usually small (Canalias, Masdemont, 2006)) required to link manifolds coming from Lissajous orbits around different equilibrium points. Indeed, in case of a zero-cost heteroclinic connection a LEO-L_2 transfer will be as expensive as a LEO-L_1 one in terms of Δv_{tot}. With respect to the fly-by formulation, recent results can be found in Renk, Hechler (2008).

Here we analyze the efficiency of the methodology developed, for transfers joining a nominal LEO and the positive branch of the stable invariant manifold, which is the one moving away from the Earth – Moon neighborhood. In this case, the procedure of

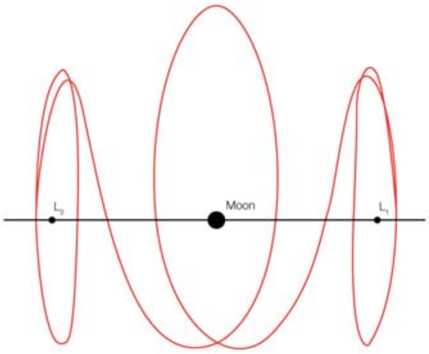

Figure 3.12: Heteroclinic connection between libration point orbits.

inserting into one of the local minima/maxima does not make sense and thus we proceed immediately to discretize the whole branch at 1 hour steps up to 140 days. The altitude of the LEOs considered is $h_{LEO} = 360$ km.

Around L_2, the Lindstedt–Poincaré series expansion allows us to consider greater arrival orbits than before. Our simulations are performed setting as amplitudes $\alpha_3 = 0.01$, 0.03, 0.06, 0.09, 0.12 and 0.15 normalized units, which correspond to 600, 2000, 4000, 6000, 8000 and 10000 km, respectively.

The general behavior detected is showed in Fig. 3.13. As the time to be spent on the manifold increases, the cost of the two maneuvers decreases, tending exponentially to a total cost of about 3.3 km/s. We remark that this value is lower than those computed by Renk, Hechler (2008), with a wide range of strategies. This remark holds whatever Lissajous amplitude we are considering.

If we want to compare our results with the work of Gordon (2008), we can state that the main advantage of the lunar fly-by approach is to decrease the time of flight in a considerable way. Indeed, skipping the Δv corresponding to the maneuver at the LEO (that cannot be avoided or reduced), and choosing a suitable point on the manifold, we obtain a cost as cheap as the one he found for the manifold insertion. However, our simulation does not reveal that this Δv depends on the z-amplitude of the arrival L_2 orbit.

Also in Fig. 3.13 we can notice that there exist some discontinuities. They are due to the presence of the Moon, which is encountered by some of the Hohmann-like legs built. This fact can be appreciated looking to Fig. 3.14 on the left, where it is clear the gap between trajectories.

With respect to the time of flight, a convenient Δv_{tot} always corresponds to a very long transfer, both in what refers to the time to be spent on the manifold and to the time required to link the LEO with the manifold. The latter can take values in the range [4 : 30] days for the Lissajous amplitudes explored.

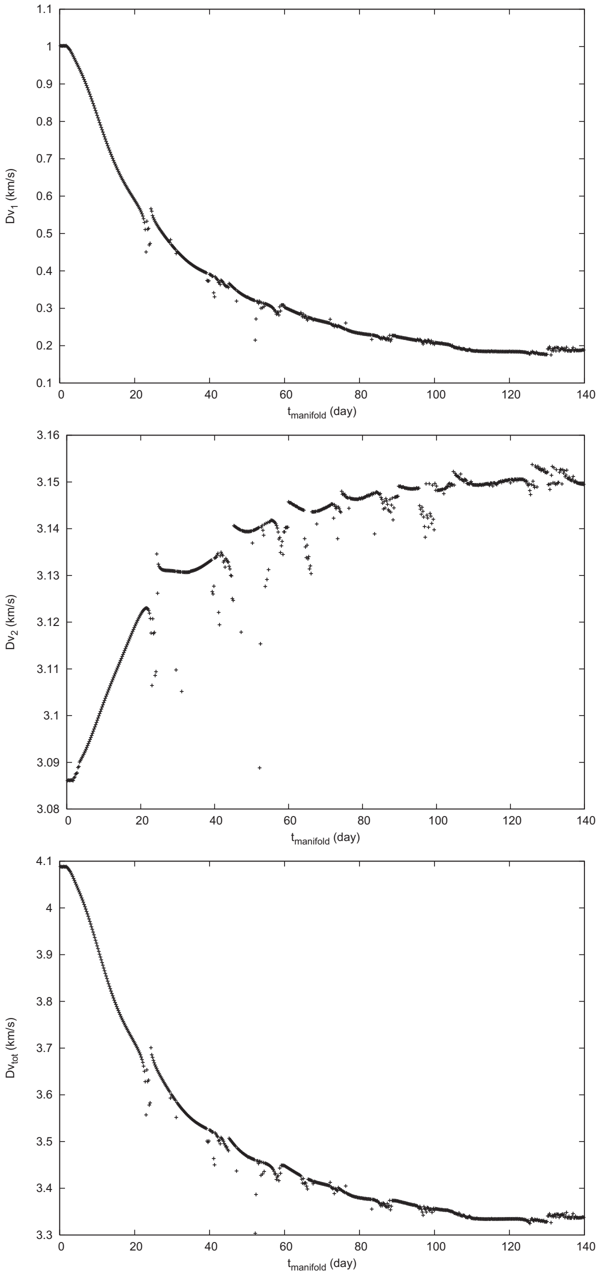

Figure 3.13: As a function of the time to be spent on the manifold, Δv_1, Δv_2 and Δv_{tot} required to connect a LEO of $h_{LEO} = 360$ km and the positive branch of the stable invariant manifold associated with the L_2 square Lissajous orbit of amplitude $\alpha_3 = 0.12$ normalized units (≈ 8000 km) in the Earth – Moon system.

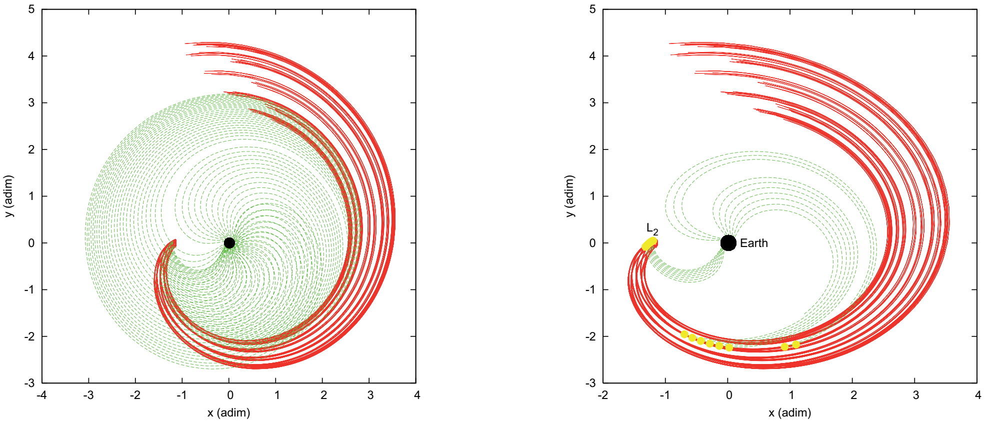

Figure 3.14: $x - y$ projection of some of the transfers computed. In red, the positive branch of the stable invariant manifold associated with the L_2 square Lissajous orbit of amplitude $\alpha_3 = 0.15$ normalized units ($\approx$ 10000 km) in the Earth – Moon system; in green the Hohmann-like legs. Right: just some legs inserting into the manifold at the yellow points.

3.4 Comments and Possible Developments

In turn, a LEO – LPO transfer requires at least two maneuvers: the most expensive one takes place at the LEO and the other is needed to insert either into the target arrival orbit or into its stable invariant manifold. The first maneuver can be made small if we start from a GEO instead of a LEO: indeed the cost can be diminished from about 3 to about 1 km/s.

In the L_1 situation the most advantageous connections take place when the fixed quasi-periodic orbit increases in size and it is worth to spend at least about 12 days on the corresponding stable invariant manifold to obtain cheaper velocity corrections. In particular, at the maxima of the distance function between the Earth and the manifold, we find the minima values for the total cost. This behavior can be explained in terms of the angle formed by the velocity of insertion into the manifold and the velocity which is proper of the manifold. When these velocities lay on the same line, but on opposite directions, the cost of the insertion maneuver is minimum.

Moreover, if the Lissajous orbit is large enough it can be convenient to transfer directly there, both in terms of fuel and time consumption.

In the L_2 case arrival orbits of different amplitudes share the same properties with respect to the total cost. We could obtain cheaper transfers than the ones associated with L_1, provided a long time of flight, which, of course, may not always be feasible from a practical point of view. To avoid this problem, we could take advantage of the Moon with the implementation of a strategy based on the negative branch of the stable invariant manifold and accounting also for a lunar fly-by.

It would be interesting to establish the technique on a bi-elliptic transfer, as d_{Earth} is quite high. Especially the case of a bi-elliptic transfer with apogee in the L_1 Sun – Earth libration region, like in low-energy transfers to the Moon. However, this choice would lead to a reduction in the less expensive part of the connection.

REFINEMENT OF ORBITS AS A CONSTRAINED OPTIMIZATION PROBLEM

4

4.1 Introduction

The transfers implemented previously are achieved within the approximation of the CR3BP, which gives results working in several situations, though it does not comprehend all the forces acting on a pointless particle moving in the Solar System. This lack might result in meaningful consequences especially in the Earth – Moon framework, where the influence of the Sun should not be neglected.

Having this in mind, in this chapter we wonder how a nominal trajectory satisfying a given simplified model can change when considering a different (but related) physical approximation. In particular, we are thinking on a general procedure allowing the refinement of orbits from the 2BP to the CR3BP, from the CR3BP to the BR4BP, from the CR3BP to the RnBP, etc..

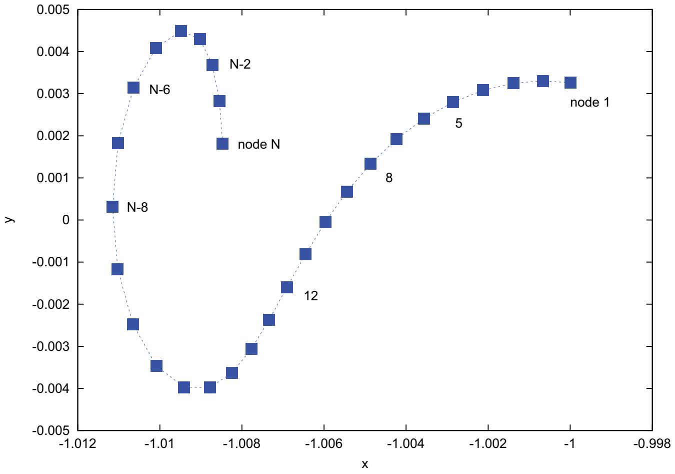

Figure 4.1: Initial guess for the refinement problem. The trajectory obtained by means of a given vector field is discretized in $N-1$ sub-arcs.

Such issue is addressed with two main approaches: a multiple shooting method and the definition of an *ad hoc* optimal control problem with direct transcription. The former procedure consists in fractionating the initial trajectory into a number of boundary value problems and adjusting the corresponding system of equations in order to avoid either ill conditioning or dynamical instability. The second method exploits optimization techniques to compute an orbit which verifies the desired equations of motion, some specific constraints and attains a minimum of a nominal objective function. In this case, the idea is to define a more adaptable tool, capable to accomplish different conditions depending on the problem and also to find trajectories that can be not natural in the sense that they can require maneuvers. Indeed, the objective function accounts for any discontinuity in velocity that might exist along the path.

For both methods, the following inputs have to be provided:

- a discretization in time of the trajectory computed by means of the reduced vector field. If we take N instants of time (see Fig. 4.1), we deal with $N-1$ sub-arcs and hence with N nodes of the type

  $$(t, \mathbf{X})_i \equiv (t_i, x_i, y_i, z_i, \dot{x}_i, \dot{y}_i, \dot{z}_i), \qquad i = 1, \ldots, N. \tag{4.1}$$

  We notice that the N nodes do not need to be equally spaced in time.

- the vector field the refined trajectory has to verify, namely,

  $$\dot{\mathbf{X}}_i = f(t_i, \mathbf{X}_i), \qquad f : \mathbb{R}^7 \to \mathbb{R}^6. \tag{4.2}$$

  In the notation adopted, $\varphi(t_i; t_{i-1}, \mathbf{X}_{i-1})$ will denote the image of $(t_{i-1}, \mathbf{X}_{i-1})$ under the flow associated with (4.2) at $t = t_i$.

The examples we will face assume as new model of forces the RnBP (see Section 1.4), which is not autonomous. We consider the refinement of Lissajous quasi-periodic orbits either in the Earth – Moon and in the Sun – Earth system, of transfers connecting a LEO with a Lissajous orbit in the Earth – Moon system (see Chapter 3) and of heteroclinic connections between two coupled CR3BP. In particular, we take as reference the trajectories computed by Canalias (2007), which link Sun – Earth LPOs with Earth – Moon LPOs, aiming at understanding their role in the phase space associated with a full model.

We will figure out that in the above situations a combined implementation of both procedures, the multiple shooting approach and the constrained optimization, is mandatory as we are not able to obtain satisfactory results using only one method.

Finally, we stress that the optimal control algorithm developed is quite general and robust, that is, it can be applied to other problems apart from those treated here. For instance, we can think about handling with trajectories established on low-thrust arcs and also with equations of motion which consider effects beyond the gravitational ones.

4.2 Multiple Shooting Method

The first approach we adopt for the refinement of orbits is the multiple shooting strategy. It looks for the solution of the following system of equations

$$F\begin{pmatrix}\mathbf{X}_1\\ \mathbf{X}_2\\ \dots\\ \mathbf{X}_N\end{pmatrix}=\begin{pmatrix}\varphi(t_2;t_1,\mathbf{X}_1)\\ \varphi(t_3;t_2,\mathbf{X}_2)\\ \dots\\ \varphi(t_N;t_{N-1},\mathbf{X}_{N-1})\end{pmatrix}-\begin{pmatrix}\mathbf{X}_2\\ \mathbf{X}_3\\ \dots\\ \mathbf{X}_N\end{pmatrix}=0. \tag{4.3}$$

The unknowns of the problem are $\mathbf{X}_i$ ($i = 1, \dots, N$), because the time variables t_i needed for the numerical integration are not modified during the process.

We note that system (4.3) contains $(N-1)\times 6$ equations with $6\times N$ unknowns. One option to overcome this under-determination is to add some additional conditions, for instance by fixing specific constraints either at $t = t_1$ and $t = t_N$, but depending on this choice and on the problem under study it may happen to converge to non-likely trajectories or encounter troubles due to ill conditioned matrices (Gómez et al., 2000a).

To prevent this from happening, we implement the Newton's method asking for the correction to be minimum. If $\mathbf{X}^{(j)} = (\mathbf{X}_1^{(j)}, \mathbf{X}_2^{(j)}, \dots \mathbf{X}_N^{(j)})$ denotes the $j-$iterate of the procedure and $\Delta\mathbf{X}^{(j)} = \mathbf{X}^{(j+1)} - \mathbf{X}^{(j)}$, then Newton's equations can be written as

$$DF(\mathbf{X}^{(j)})\cdot\Delta\mathbf{X}^{(j)} = -F(\mathbf{X}^{(j)}),$$

and we want to minimize $||\Delta\mathbf{X}^{(j)}||_2$.

Introducing the Lagrange function $\mathcal{L}(\Delta\mathbf{X},\mu)$ with vector multiplier μ, namely,

$$\mathcal{L}(\Delta\mathbf{X},\mu) = \Delta\mathbf{X}^T\Delta\mathbf{X} + \mu^T\cdot(F(\mathbf{X}) + DF(\mathbf{X})\cdot\Delta\mathbf{X}), \tag{4.4}$$

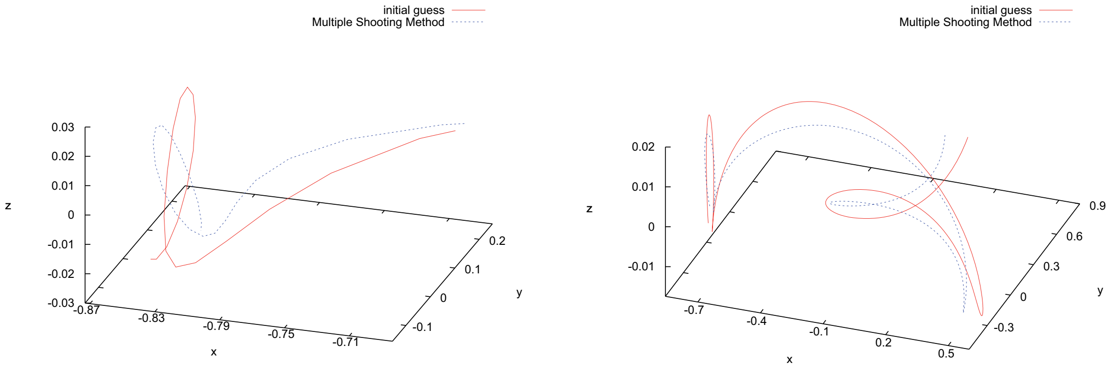

Figure 4.2: Two examples of refinement performed with the multiple shooting approach. They both belong to the Earth – Moon synodical reference system.

we get to

$$\Delta \mathbf{X}^{(j)} = -DF(\mathbf{X}^{(j)})^T \cdot [DF(\mathbf{X}^{(j)}) \cdot DF(\mathbf{X}^{(j)})^T]^{-1} \cdot F(\mathbf{X}^{(j)}). \tag{4.5}$$

It is convenient to perform a Cholesky factorization of $M \equiv DF(\mathbf{X}^{(j)}) \cdot DF(\mathbf{X}^{(j)})^T$ to solve the problem recursively and avoid the instability matters that can arise due to the bad conditioning of $DF(\mathbf{X})$.

For further details, refer to Gómez, Masdemont, Simó (1998). We only remark that there exists the possibility to assign a weight, say $\mathbf{w}_i \equiv (w_i^t, w_i^x, w_i^y, w_i^z, w_i^{\dot{x}}, w_i^{\dot{y}}, w_i^{\dot{z}})$ $(i = 1, \dots, N)$, to each node in order to create a sort of hierarchy: the greater the weight the more effort should be put to displace the corresponding node. As a matter of fact, the correction which is actually applied to a given variable is the one offered by (4.5), divided by the weight $\mathbf{w}_i$.

4.2.1 Tests

We have applied the above procedure to refine LEO – LPO transfers and heteroclinic connections between two coupled CR3BP. With various attempts, we have figured out that this is not the most appropriate tool for our situations. The main difficulties we have detected reside in the fact that to obtain convergence becomes much and much harder as the trajectory gets close to a major body, for instance the Earth. Also, the refined orbit often lies quite far from the original one. For some examples, see Fig. 4.2.

Clearly, a very important responsible of such drawbacks is the sensitivity characterizing the Earth – Moon system. Since nearby initial conditions can evolve easily in a very different manner, in order to preserve the shape and the usefulness of the initial transfers we must force the algorithm not to move significantly from the initial guess, by exploiting at least the functionality of the weights.

Unfortunately, this is not sufficient for our intentions, because we also need the option to consider boundary conditions or specific constraints. Moreover, this multiple shooting method tries to cancel out any discontinuity in velocity (and position) that can appear. Some kind of transfers are founded on maneuvers that can be reduced but not avoided, provided their utility to the final purpose of the designed orbit.

4.3 Optimal Control Problem

The second strategy used consists in an optimal control problem. In a nutshell, we look for some control functions such that the states $\mathbf{X}_i$ fulfill the physical properties we are interested in, and a given performance criterion is minimized (or maximized). We introduce such formulation because it has the advantage of setting some specific requirements when desired. These constraints can be equalities or inequalities and can involve the controls, the states, or both.

We refer to the direct transcription approach, that is, we discretize the dynamical variables in time, as stated by (4.1), and we define a finite dimensional non-linear programming problem. The variables are modified in order to optimize directly the nominal

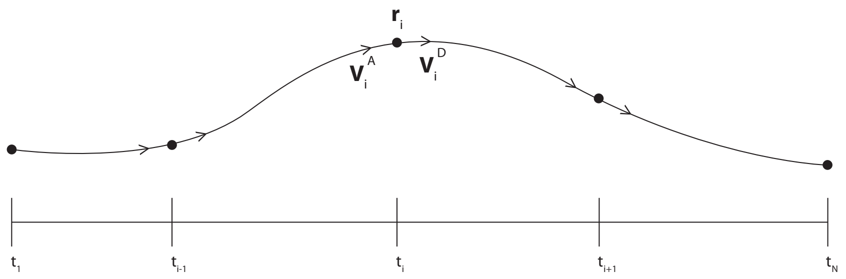

Figure 4.3: Each node is characterized by a value of time, position and two velocities. See more explanation in the text.

objective function, hence analytic expressions for the necessary conditions for optimality are not needed neither is an initial guess for the adjoint variables (or co-states) (see, for instance, Bryson, Ho (1975)).

In contrast with the previous methodology, now the time t represents a variable of the problem and two velocities (see Fig. 4.3) correspond to each node: a *departure* and an *arrival* one, defined as

$$\begin{aligned} \mathbf{v}_i^A &= \varphi(t_i; t_{i-1}, \mathbf{X}_{i-1})_{|\mathbf{v}}, \qquad & i = 1, \ldots, N, \\ \mathbf{v}_i^D &= (\dot{x}_i, \dot{y}_i, \dot{z}_i), \qquad & i = 1, \ldots, N, \end{aligned}$$

where $_{|\mathbf{v}}$ refers to the velocity components of the state. The first and the last node are 'special' nodes, in the sense that we choose the velocity of arrival for the first node $\mathbf{v}_1^A$, and the velocity of departure for the last one $\mathbf{v}_N^D$.

In the way we set the problem, only the variables representing time and position can be changed in order to minimize the objective function, which depends on the maneuvers, $\Delta\mathbf{v}_i = \mathbf{v}_i^A - \mathbf{v}_i^D$, required at each $i-$node for $i = 1, \ldots, N$. In fact, we look for N nodes $(t, \mathbf{X})_i$ $(i = 1, \ldots, N)$ meeting the following conditions:

1. to provide a trajectory which is continuous in position:

   $$\varphi(t_i; t_{i-1}, \mathbf{X}_{i-1})_{|\mathbf{r}} = (x_i, y_i, z_i) \equiv \mathbf{r}_i, \qquad i = 2, \ldots, N, \tag{4.6}$$

   where $_{|\mathbf{r}}$ refers to the position components of the state.

2. A well-defined objective function is at a local minimum in a given domain D of the phase space:

   $$min\ F_{obj}(\Delta\mathbf{v}_1, \ldots, \Delta\mathbf{v}_i, \ldots, \Delta\mathbf{v}_N) = \min_{(t,\mathbf{r})\in D} F_{obj}(t, \mathbf{r}), \tag{4.7}$$

   where $\Delta\mathbf{v}_1(t_1, \mathbf{r}_1, t_2, \mathbf{r}_2)$, $\Delta\mathbf{v}_N(t_{N-1}, \mathbf{r}_{N-1}, t_N, \mathbf{r}_N)$ and $\Delta\mathbf{v}_i(t_{i-1}, \mathbf{r}_{i-1}, t_i, \mathbf{r}_i, t_{i+1}, \mathbf{r}_{i+1})$ $(i = 2, \ldots, N-1)$.

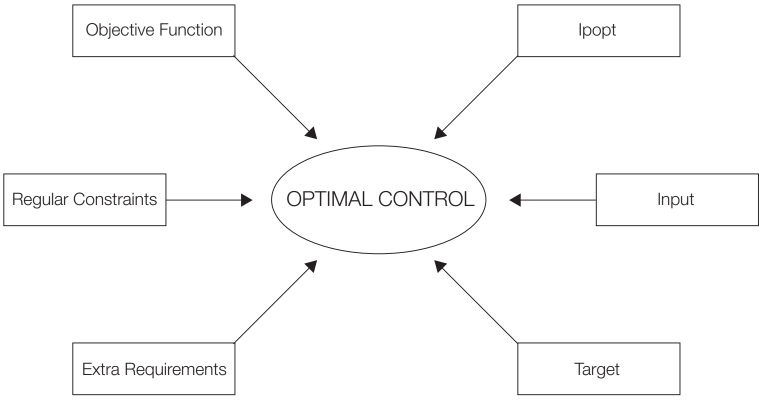

Figure 4.4: Main ingredients of the optimal control approach implemented.

3. Some linear and non-linear relationships are accomplished:

$$\mathbf{l} \leq \begin{pmatrix} t_i \\ \mathbf{X}_i \\ A(t,\mathbf{X})_i \\ g(t_i,\mathbf{X}_i) \end{pmatrix} \leq \mathbf{u}, \qquad i = 1, \ldots, N, \tag{4.8}$$

   where **l** and **u** are lower and upper bounds set, respectively, and **A** and **c** represent linear and non-linear constraints, respectively.

   In particular, (4.8) allows to define boundary conditions.

In turn, $\mathbf{v}_i^D$ are the controls we search out. In an ideal situation the trajectory computed is continuous also in velocity and thus $\Delta\mathbf{v}_i = 0$ $(i = 1, \ldots, N)$, but, as already mentioned, some maneuvers might be unavoidable depending on the circumstance.

To find the minimum of F_{obj} we take advantage of an optimizer, which is aided by a *target* procedure for satisfying the continuity in position. The whole algorithm is structured as a package made of several modules (see Fig. 4.4), which are described in the forthcoming sections.

4.3.1 General Algorithm

The fundamental aspects of the second refinement procedure can be sketched as follows.

- We take advantage of IPOPT (Interior Point Optimizer) (Wäcter, Biegler, 2004; Laird, Wäcter, 2006) which is based on a sequence of barrier problems, that are solved by means of a primal–dual interior point algorithm with a filter line–search. The underlying concept is that trial points are accepted if they improve the objective function or improve the constraint violation instead of a combination of those two measures defined by a merit function.

- IPOPT makes use of the gradient of F_{obj} and of any constraint required. These gradients form the row of the Jacobian matrix used in the optimization algorithm.
- Instead of setting as a constraint the requirement (4.6) we guarantee its fulfillment by implementing a differential correction (or target) procedure for each leg of the discretized initial guess trajectory (see Section 4.3.2). In this way, in the easiest situation IPOPT works only on the minimization of F_{obj}.
- The objective function is defined as the sum of the square of the maneuvers required at each node, that is,

  $$F_{obj} = \sum_{i=1}^{N} w_i ||\Delta \mathbf{v}_i||^2 = \sum_{i=1}^{N} w_i ||\mathbf{v}_i^A - \mathbf{v}_i^D||^2, \tag{4.9}$$

  where w_i represents a weight associated with the $i-$node, that can be a simple constant or a function depending on either the index i or the associated initial state. We borrow such useful tool from the multiple shooting method introduced before in order to control the size of the maneuvers. Here, w_i appears as a factor and not as a divisor, because we want to minimize F_{obj}. Again, a big w_i with respect to the other weights helps to obtain a smaller cost at the $i-$node.
- We provide some general restrictions (see Section 4.3.3) that can be imposed depending on the problem considered, in particular to bound the displacement either in time and position that can be applied to each node constituting the initial guess, and also $\Delta \mathbf{v}_i$ for any given $i = 1, \dots, N$. Apart from these, it is possible to add any specific requirement, by providing the corresponding definition and gradient.

Whenever IPOPT either reaches the maximum allowed number of iterations or encounters an acceptable solution, we check the value of $\Delta \mathbf{v}_i$ for any $i = 1, \dots, N$: if they do not fully agree with our requirement we restart the algorithm setting as initial guess the solution found, changing w_i and eventually also the nodes and the associated constraints. When an optimal refinement is obtained, we neglect the nodes at which $\Delta \mathbf{v}_i$ is lower than a given tolerance and we apply the optimization algorithm to a more realistic objective function, namely,

$$F_{obj} = \sum_{i=1}^{N} w_i ||\mathbf{v}_i^A - \mathbf{v}_i^D||. \tag{4.10}$$

In the unlucky case of unfeasibility matters, the procedure must be restarted with a different choice of discretization and constraints.

4.3.2 Target Procedure

To meet the condition of continuity in position (4.6) and to compute $\mathbf{v}_i^D$ $(i = 1, \dots, N-1)$ and $\mathbf{v}_i^A$ $(i = 2, \dots, N)$, we implement a target procedure. With this formulation, the velocity does not appear as a variable of the problem but it is computed by means of the Newton's method.

Starting from the time t_i and position $\mathbf{r}_i$ associated with the $i-$node $(i = 1, \ldots, N-1)$ and a suitable initial guess, we look for the closest $\mathbf{v}_i^D$ which ensures to reach $\mathbf{r}_{i+1}$ in a time equal to $t_{i+1} - t_i$. Once obtained convergence within a precision depending on the problem addressed, we get $\mathbf{v}_i^D$ and also $\mathbf{v}_{i+1}^A$.

Concretely, we aim at finding $\mathbf{v}_i^D$ such that

$$\varphi(t_{i+1}; t_i, \mathbf{r}_i, \mathbf{v}_i^D)_{|\mathbf{r}} = \mathbf{r}_{i+1}, \qquad i = 1, \ldots, N-1.$$

This is achieved by an iterative correction procedure, which provides $\mathbf{v}_i^D$ and $\mathbf{v}_{i+1}^A$. The initial guess is usually offered by the trajectory obtained by means of the simplified vector field.

Derivatives

As just said, the optimization process needs the differential of F_{obj} and of all the equations defining the constraints. The target procedure makes the optimizer to act only on (t_i, x_i, y_i, z_i) $(i = 1, \ldots, N)$ and thus the derivatives of F_{obj} and any function containing $\mathbf{v}_i^A$ and $\mathbf{v}_i^D$ $(i = 1, \ldots, N)$ are not explicit. Here, we explain how to cope with their computation.

Let us define $\Phi_{6\times 7}$ as[1]

$$\Phi_{6\times 7} = \left(\begin{array}{c|ccc|ccc} \frac{\partial \varphi_x}{\partial t} & \frac{\partial \varphi_x}{\partial x} & \frac{\partial \varphi_x}{\partial y} & \frac{\partial \varphi_x}{\partial x} & \frac{\partial \varphi_x}{\partial \dot{x}} & \frac{\partial \varphi_x}{\partial \dot{y}} & \frac{\partial \varphi_x}{\partial \dot{z}} \\ \frac{\partial \varphi_y}{\partial t} & \frac{\partial \varphi_y}{\partial x} & \frac{\partial \varphi_y}{\partial y} & \frac{\partial \varphi_y}{\partial x} & \frac{\partial \varphi_y}{\partial \dot{x}} & \frac{\partial \varphi_y}{\partial \dot{y}} & \frac{\partial \varphi_y}{\partial \dot{z}} \\ \frac{\partial \varphi_z}{\partial t} & \frac{\partial \varphi_z}{\partial x} & \frac{\partial \varphi_z}{\partial y} & \frac{\partial \varphi_z}{\partial x} & \frac{\partial \varphi_z}{\partial \dot{x}} & \frac{\partial \varphi_z}{\partial \dot{y}} & \frac{\partial \varphi_z}{\partial \dot{z}} \\ \hline \frac{\partial \varphi_{\dot{x}}}{\partial t} & \frac{\partial \varphi_{\dot{x}}}{\partial x} & \frac{\partial \varphi_{\dot{x}}}{\partial y} & \frac{\partial \varphi_{\dot{x}}}{\partial x} & \frac{\partial \varphi_{\dot{x}}}{\partial \dot{x}} & \frac{\partial \varphi_{\dot{x}}}{\partial \dot{y}} & \frac{\partial \varphi_{\dot{x}}}{\partial \dot{z}} \\ \frac{\partial \varphi_{\dot{y}}}{\partial t} & \frac{\partial \varphi_{\dot{y}}}{\partial x} & \frac{\partial \varphi_{\dot{y}}}{\partial y} & \frac{\partial \varphi_{\dot{y}}}{\partial x} & \frac{\partial \varphi_{\dot{y}}}{\partial \dot{x}} & \frac{\partial \varphi_{\dot{y}}}{\partial \dot{y}} & \frac{\partial \varphi_{\dot{y}}}{\partial \dot{z}} \\ \frac{\partial \varphi_{\dot{z}}}{\partial t} & \frac{\partial \varphi_{\dot{z}}}{\partial x} & \frac{\partial \varphi_{\dot{z}}}{\partial y} & \frac{\partial \varphi_{\dot{z}}}{\partial x} & \frac{\partial \varphi_{\dot{z}}}{\partial \dot{x}} & \frac{\partial \varphi_{\dot{z}}}{\partial \dot{y}} & \frac{\partial \varphi_{\dot{z}}}{\partial \dot{z}} \end{array} \right) \equiv \begin{pmatrix} \Lambda_{3\times 1} & A_{3\times 3} & B_{3\times 3} \\ \Gamma_{3\times 1} & C_{3\times 3} & D_{3\times 3} \end{pmatrix}. \tag{4.11}$$

Then, we can write the variations in position and velocity at the final time, $\Delta\mathbf{r}_{i+1}^A$ and $\Delta\mathbf{v}_{i+1}^A$, as a function of the variations in position and velocity at the initial time, $\Delta\mathbf{r}_i^D$ and $\Delta\mathbf{v}_i^D$, and also of the variations in the initial and final time, Δt_i^D and Δt_{i+1}^A in the following way

$$\begin{pmatrix} \Delta\mathbf{r}_{i+1}^A \\ \Delta\mathbf{v}_{i+1}^A \end{pmatrix} \approx \Phi \begin{pmatrix} \Delta t_i^D \\ \Delta\mathbf{r}_i^D + \Delta t_i^D \ \dot{\mathbf{r}}_i{}^D \\ \Delta\mathbf{v}_i^D + \Delta t_i^D \ \dot{\mathbf{v}}_i{}^D \end{pmatrix} + \begin{pmatrix} \Delta t_{i+1}^A \ \dot{\mathbf{r}}_{i+1}^A \\ \Delta t_{i+1}^A \ \dot{\mathbf{v}}_{i+1}^A \end{pmatrix}, \tag{4.12}$$

where $i = 1, \ldots, N-1$.

Starting from (4.12), the derivatives desired are found by setting successively equal to

---

[1] From now on, we simplify the notation in such a way that $\varphi_x \equiv \varphi(t_{i+1}; t_i, \mathbf{X}_i)_{|x}$.

0 the variations we are not interested in. This implies:

$$\begin{cases} \frac{\Delta \mathbf{v}_i^D}{\Delta \mathbf{r}_i^D} = -B^{-1}A, \\ \frac{\Delta \mathbf{v}_i^D}{\Delta \mathbf{r}_{i+1}^A} = B^{-1}, \\ \frac{\Delta \mathbf{v}_i^D}{\Delta \mathbf{t}_i^D} = -B^{-1}A\dot{\mathbf{r}}_i{}^D - \dot{\mathbf{v}}_i{}^D - B^{-1}\Lambda, \\ \frac{\Delta \mathbf{v}_i^D}{\Delta \mathbf{t}_{i+1}^A} = -B^{-1}\dot{\mathbf{r}}_{i+1}^A, \end{cases}$$

$$\begin{cases} \frac{\Delta \mathbf{v}_{i+1}^A}{\Delta \mathbf{r}_i^D} = C - DB^{-1}A, \\ \frac{\Delta \mathbf{v}_{i+1}^A}{\Delta \mathbf{r}_{i+1}^A} = DB^{-1}, \\ \frac{\Delta \mathbf{v}_{i+1}^A}{\Delta t_i^D} = \Gamma + C\dot{\mathbf{r}}_i{}^D + D\dot{\mathbf{v}}_i{}^D - D \cdot B^{-1}(\Lambda + A\dot{\mathbf{r}}_i{}^D + B\dot{\mathbf{v}}_i{}^D), \\ \frac{\Delta \mathbf{v}_{i+1}^A}{\Delta t_{i+1}^A} = -DB^{-1}\dot{\mathbf{r}}_{i+1}^A + \dot{\mathbf{v}}_{i+1}^A. \end{cases}$$

The optimization is forced to take into account the dynamics we want to see satisfied because of (4.12).

We notice that we need to integrate numerically from t_i to t_{i+1} ($i = 1, \ldots, N-1$) not only the equations of motion but also the variational equations with respect to position and time. In our development we adopt a 7-8 Runge-Kutta-Fehlberg method with local truncation error $\epsilon = 10^{-14}$. The variational equations associated with the RnBP model can be found in Appendix A.

4.3.3 Regular Constraints

The algorithm includes a set of regular constraints that can be imposed at each node. In particular, if ρ_i and τ_i are, respectively, the position and time associated with the $i-$node at the initial seed for $i = 1, \ldots, N$, then we can choose:

- not to move the position of the $i-$node more than a fixed amount R_i (see Fig. 4.5):

$$||\mathbf{r}_i - \rho_i||^2 < R_i^2;$$

- not to move the time associated with the $i-$node more than a fixed amount T_i:

$$(t_i - \tau_i)^2 < T_i^2;$$

- to bound the maneuver required at the $i-$node a certain amount ν_i:

$$||\mathbf{v}_i^A - \mathbf{v}_i^D||^2 < \nu_i^2.$$

Note that R_i, T_i and ν_i do not need to be the same for every i.

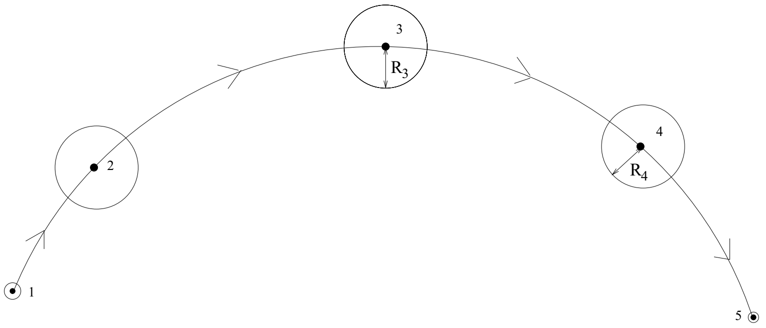

Figure 4.5: One of the regular constraint that can be set: to bound the displacement in position with respect to the initial guess.

4.3.4 Input

As it was stated beforehand, the inputs of the procedure are the following:

1. the initial guess for the trajectory;
2. the domain where the variables (t_i, x_i, y_i, z_i) $(i = 1, \ldots, N)$ vary;
3. the standard constraints to impose at each node;
4. $\mathbf{v}_1^A$ and $\mathbf{v}_N^D$;
5. the weight corresponding to each node;
6. the minimum and maximum tolerance allowed to the target procedure;
7. the implementation of a Lambert strategy (Simó, 1973) (whenever it can apply) for a more accurate initial guess if the target fails;
8. any extra requirement to be satisfied. If this is the case, it is mandatory to provide the corresponding function and its gradient with respect to all the nodes the optimizer can handle.

We underline that there exists the possibility to load some variables into the program, choosing not to optimize them. This option can help, for instance, in order to reduce the computational effort; to employ some nodes just in the target procedure; if we want to arrive to a given position at a well-defined epoch.

Also, $\mathbf{v}_1^A$ and $\mathbf{v}_N^D$ can be given as bare coordinates or as complicated functions.

All these data have to be written into specific given input files. The algorithm reads from there and creates the proper structures that will be used throughout the whole process. We note that we deal with object-oriented programming.

4.3.5 Extra Functions

We incorporate some extra features in the program, that can be useful according to the situation. In particular, we can

- transform between different reference systems;
- compute orbital elements;
- plot the trajectory at each iteration of the optimization;
- add/remove nodes;
- save/retrieve information at each iteration of the optimization (e.g. F_{obj});
- perform some accuracy tests at the end of the whole process.

4.4 Examples

To illustrate the application of the optimal control approach we consider three examples:

1. Earth – Moon and Sun – Earth Lissajous orbits;
2. heteroclinic Earth – Moon and Sun – Earth connections;
3. LEO – LPO transfers (see Chapter 3).

They all have been refined considering as new vector field the RnBP introduced in Section 1.4. The requirements we look for vary according to the example.

In general, it turns out that the accuracy of the initial guess, the values of the weights w_i and the extra constraints set are crucial ingredients to obtain the refinement of a nominal trajectory.

Besides, an optimizer is a quite expensive tool from a computational point of view and it usually approaches the minimum of F_{obj} in an asymptotic way, that is, quite slowly. Because of this, we decide to mix the two methodologies above explained in order to get to the desired level of accuracy. Precisely, it means that after up to 5 implementations of the optimal control algorithm we plug the corresponding solution into the multiple shooting method as initial guess and the trajectory we converge to is then set as initial seed for a last constrained optimization. If the refined trajectory needs control maneuvers that cannot be avoided, the multiple shooting approach is applied independently on the legs of the trajectory separated by such $\Delta\mathbf{v}$s. This method reveals to be very effective.

4.4.1 Lissajous Orbits

First of all, we consider the refinement of a Lissajous quasi-periodic orbit around the L_1 equilibrium point in the Sun – Earth system. We take a 44 years long one and we discretize it at intervals of about 40 days, obtaining 400 nodes. Such discretization is

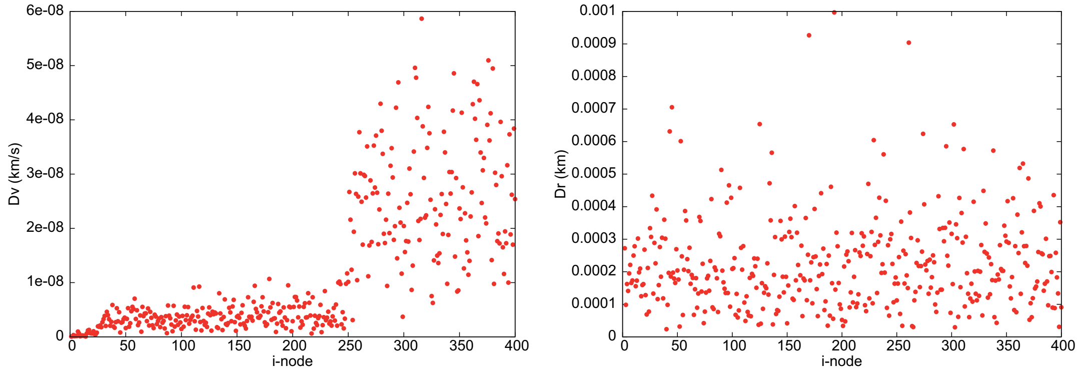

Figure 4.6: On the left, the discontinuities (km/s) in velocity obtained at each node for a L_1 Lissajous quasi-periodic orbit in the Sun – Earth system after the refinement procedure. On the right, the differences (km) in position between the refined trajectory requiring such small maneuvers and the orbit integrated numerically departing from the refined initial point.

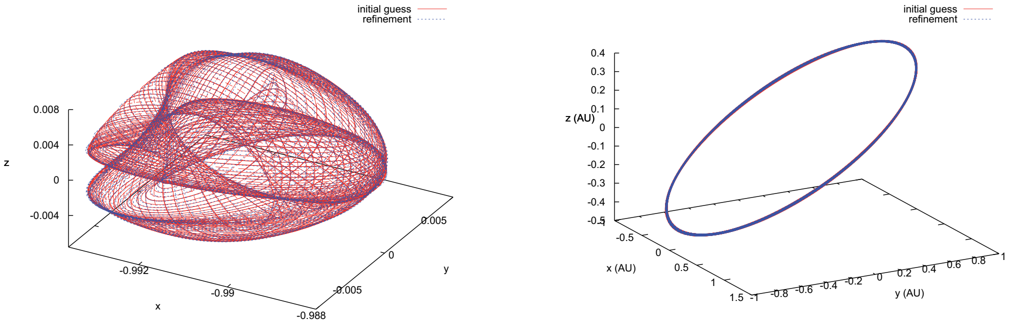

Figure 4.7: The refined L_1 Sun – Earth Lissajous quasi-periodic orbit (blue) and the initial guess (red) in the synodical (left) and inertial (right) reference systems.

chosen according to the target procedure, that is, the maximum arc length such that it can converge within an accuracy of 1 mm. As constraints, we impose the time associated with each node not to move from the initial guess and also $\Delta\mathbf{v}_i < 1$ mm/s ($i = 1, \ldots, 400$). As $\mathbf{v}_1^A$ and $\mathbf{v}_{400}^D$ we set the ones which characterize the initial seed. The RnBP, the vector field we want to move to, takes the origin at the Solar System barycenter and the initial epoch is set at JED 2451544.5 (January 1, 2000).

In Fig. 4.6 on the left, we show the maneuvers obtained at each node at the end of the whole procedure: they are all less than 1 mm/s. We can claim that the total cost to maintain the quasi-periodic orbit is less than the one resulting from standard station-keeping approaches, though our strategy is established on different hypotheses. The $\Delta\mathbf{v}_i$ ($i = 1, \ldots, 400$) found are likely too small to be performed in a real application, but if we integrate numerically the RnBP equations of motion taking as initial condition the initial point of the refined trajectory, we get a trajectory which is close to the one requiring such small maneuvers, the differences in position between them being always less than 1 m, as shown in Fig. 4.6 on the right.

In Fig. 4.7 we display the trajectory we adopt as initial guess for the optimal control approach and the one refined, in the synodical and in the inertial reference system.

Furthermore, we apply the refinement to a Lissajous quasi-periodic orbit around the L_1 equilibrium point in the Earth – Moon system. In this case, we take a 4 years long trajectory split in 4 days long legs, obtaining 400 nodes as before. Now, the RnBP is centered at the Earth. The above considerations hold, as we can see from Figs. 4.8 and 4.9.

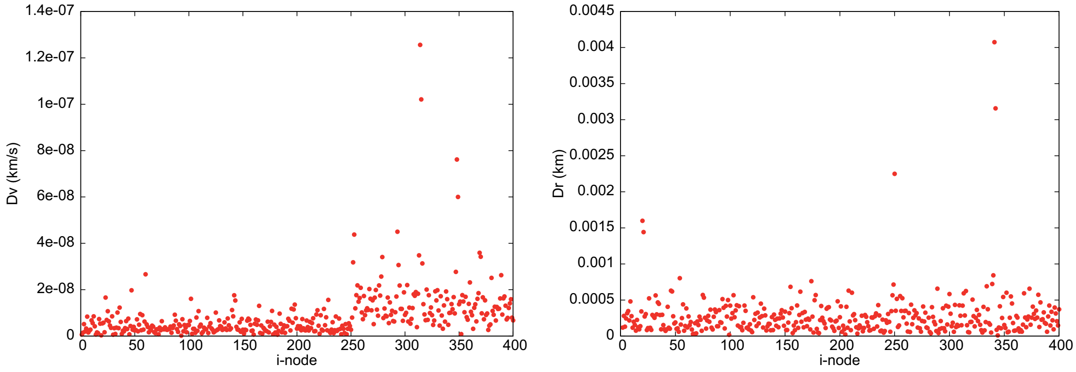

Figure 4.8: On the left, the discontinuities (km/s) in velocity obtained at each node for a L_1 Lissajous quasi-periodic orbit in the Earth – Moon system after the refinement procedure. On the right, the differences (km) in position between the refined trajectory requiring such small maneuvers and the orbit integrated numerically departing from the refined initial point.

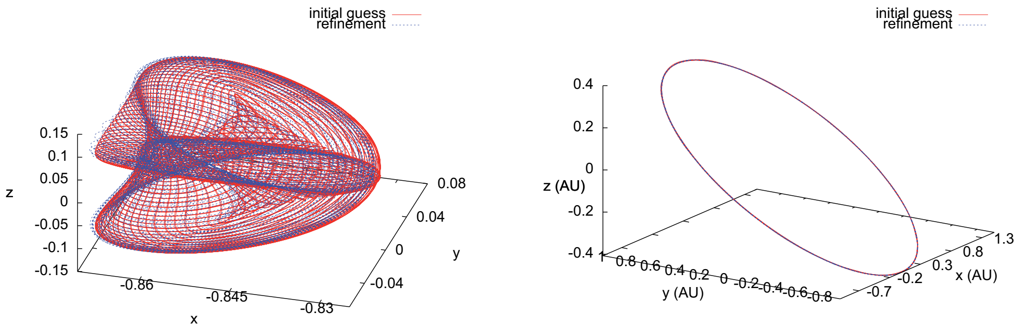

Figure 4.9: The refined L_1 Earth – Moon Lissajous quasi-periodic orbit (blue) and the initial guess (red) in the synodical (left) and inertial (right) reference systems.

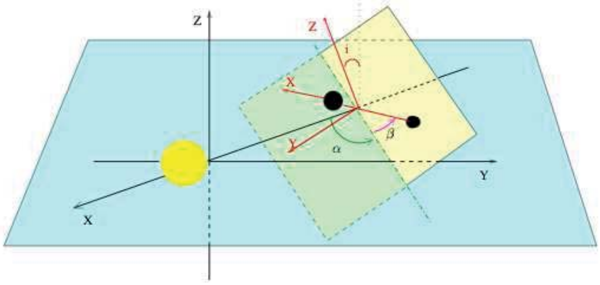

Figure 4.10: Relative configuration between Sun – Earth and Earth – Moon coupled CR3BP defined by Canalias (2007) to compute initial seeds for heteroclinic connections.

4.4.2 Heteroclinic Connections

The second example we present regards the refinement of heteroclinic connections between two coupled Sun – Earth and Earth – Moon CR3BP. The trajectories considered depart from a nominal Lissajous quasi-periodic orbit around the L_2 equilibrium point in the Earth – Moon system and arrive to a given Lissajous quasi-periodic orbit around the L_2 equilibrium point in the Sun – Earth system. The connections are accomplished by matching the unstable invariant manifold associated with the Earth – Moon L_2 Lissajous orbit with the stable invariant manifold corresponding to the Sun – Earth L_2 nominal orbit. Such transfers can require a maneuver at the intersection point.

As initial guess for our procedure, we take the data provided by Canalias (2007). We notice that apart from developing a technique aimed at the computation of such trajectories within the CR3BP approximation, she applied a modified version of the multiple shooting method (Section 4.2) to refine some of them into the RnBP. In some sense, the optimal control strategy implemented here was born from those attempts in order to have at our disposal a more flexible and working tool.

A determinant aspect to refine this kind of transfers is the relative configuration assumed for the two CR3BP. In particular, three angles define the coupling (see Fig. 4.10):

1. the inclination of the Earth – Moon orbital plane with respect to the ecliptic ($i = 5°14'$);
2. the angle α from the axis joining the Sun and the Earth – Moon barycenter to the line of nodes of the lunar orbit, measured on the ecliptic plane;
3. the angle β from the line of nodes to the position of the Moon, measured on the plane of motion of the Moon around the Earth, or the plane of relative motion of the Earth and the Moon.

Because of this, it is very important to set properly the epoch at which the connection takes place, as we want the Earth, Moon and Sun configuration to be close to the values adopted for α and β.

In the examples analyzed, the Lissajous orbit winds around the Earth – Moon L_2 equilibrium point for about 2 months, the one around the Sun – Earth L_2 for about 1 year. In the discretization adopted, we have 1 day long arcs in the Earth – Moon part, and 10 days long arcs for the Sun – Earth part.

The constraints set ask all the variables to move less then 1 hour in time and less than 100 km in position from the initial guess. Moreover, we require any discontinuity in velocity to be smaller than 1 mm/s.

It turns out that we can refine heteroclinic connections at zero-cost into the RnBP, whose origin is fixed at the Solar System barycenter, if the matching maneuver computed with the coupled CR3BP approximation is not greater than 250 m/s.

The main drawback, we are not able to avoid in some cases, is the modification of the size of the Earth – Moon Lissajous orbit: it very often becomes twice as big as the nominal one.

In Figs. 4.11, 4.12, 4.13 and 4.14, we show some results in the Sun – Earth and Earth – Moon reference systems together with the maneuvers required at each node.

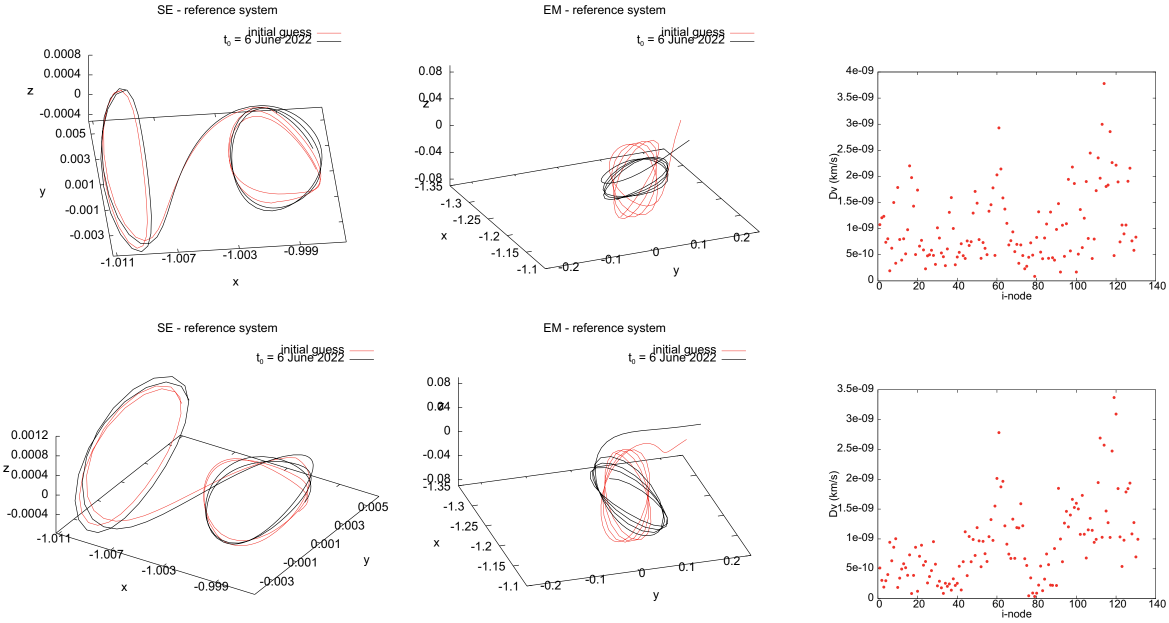

Figure 4.11: The refinement obtained for several heteroclinic connections between Sun – Earth and Earth – Moon coupled systems (black) together with the initial guess (red). On the left, in the Sun – Earth synodical reference system; on the middle, the Earth – Moon leg. On the right, the maneuvers (km/s) required. The vertical amplitude of the Sun – Earth Lissajous orbit is the greatest possible, that is, about 550000 km.

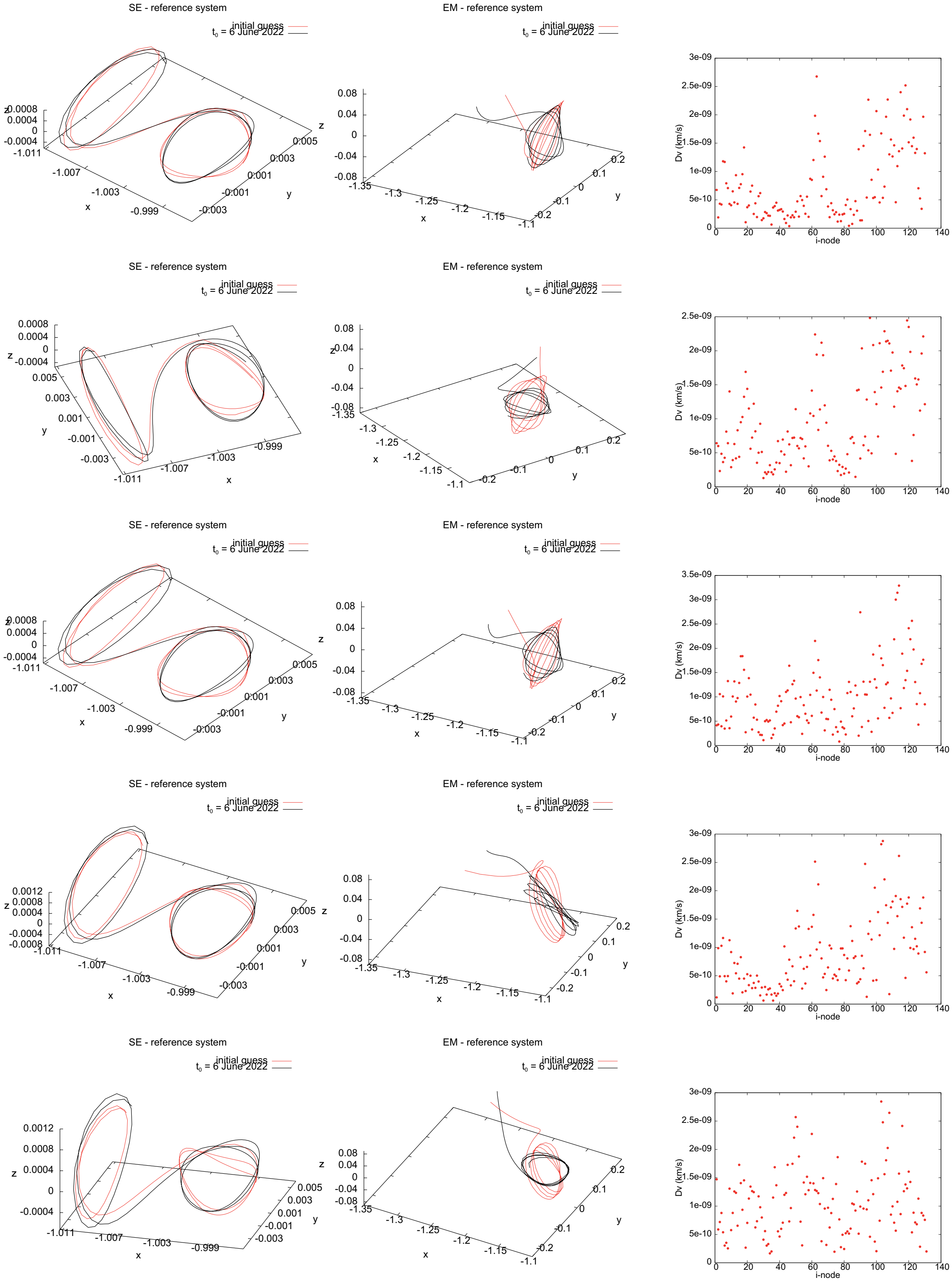

Figure 4.12: The refinement obtained for several heteroclinic connections between Sun – Earth and Earth – Moon coupled systems (black) together with the initial guess (red). On the left, in the Sun – Earth synodical reference system; on the middle, the Earth – Moon leg. On the right, the maneuvers (km/s) required. The vertical amplitude of the Sun – Earth Lissajous orbit is the greatest possible, that is, about 550000 km.

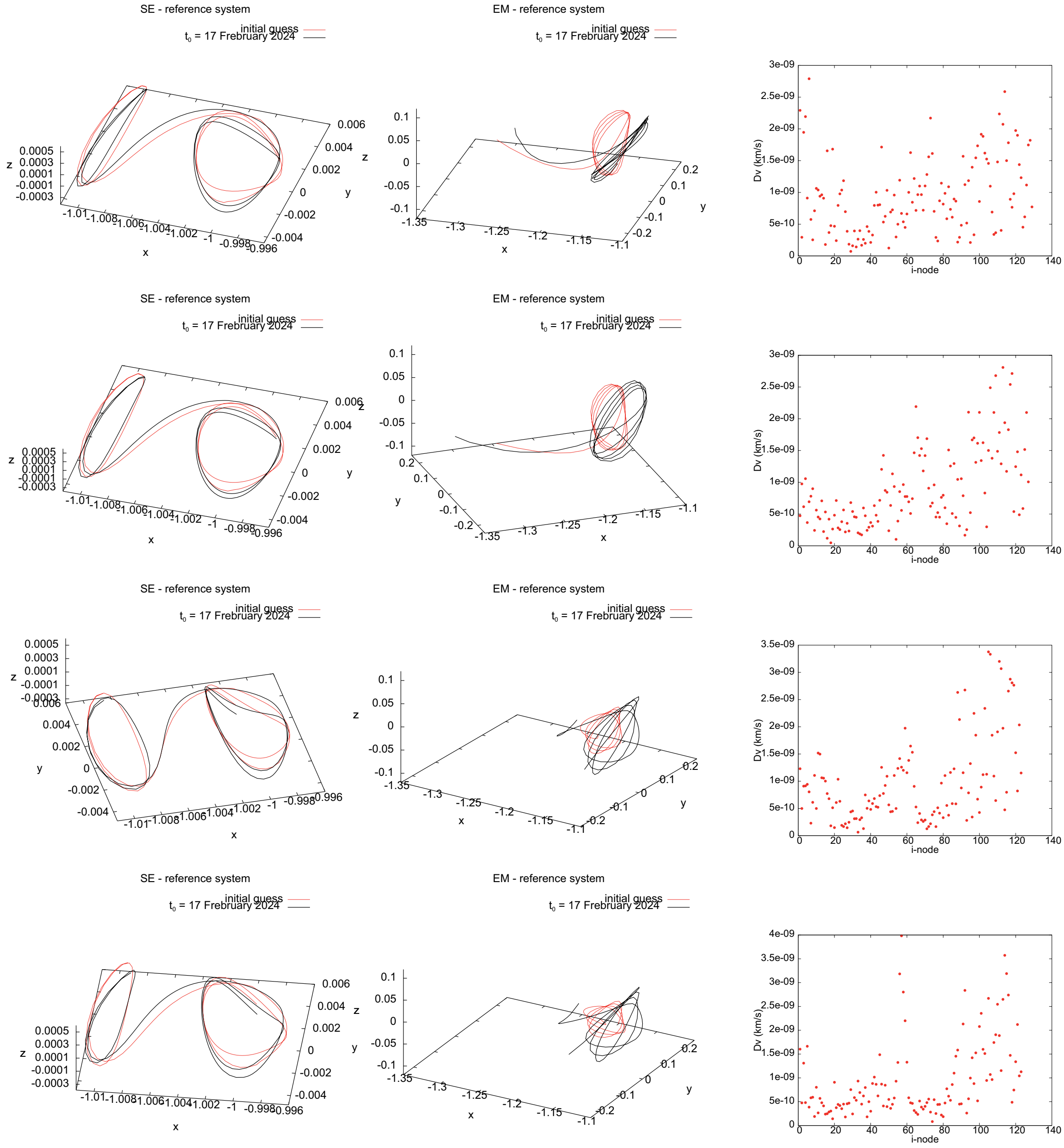

Figure 4.13: The refinement obtained for several heteroclinic connections between Sun – Earth and Earth – Moon coupled systems (black) together with the initial guess (red). On the left, in the Sun – Earth synodical reference system; on the middle, the Earth – Moon leg. On the right, the maneuvers (km/s) required. The vertical amplitude of the Sun – Earth Lissajous orbit is the smallest possible, that is, about 15000 km.

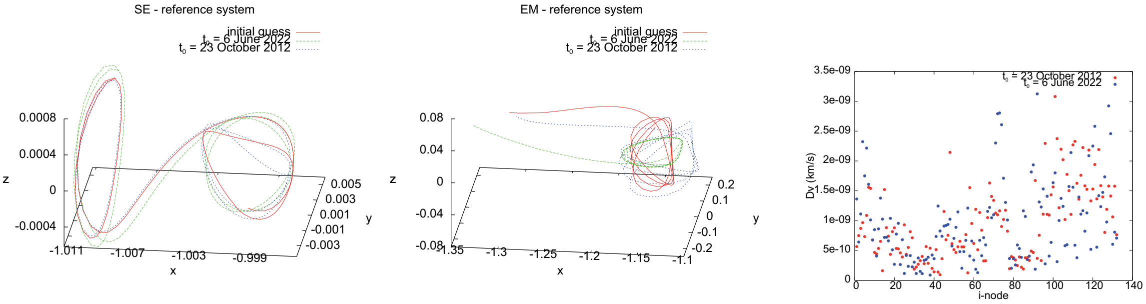

Figure 4.14: The refinement obtained for a heteroclinic connection between Sun – Earth and Earth – Moon coupled systems for two different epochs (blue and green) together with the initial guess (red). On the left, in the Sun – Earth synodical reference system; on the middle, the Earth – Moon leg. On the right, the maneuvers (km/s) required.

4.4.3 LEO – LPO Transfers

Finally, the most challenging refinement regards LEO – LPO transfers (see Chapter 3). In this case, we make use of equations (1.17) and we must add some extra custom constraints to the optimal control algorithm. They are:

1. the distance between the first node and the center of the Earth to be the one desired (for instance 6378.14+360 km);
2. $\mathbf{v}_1^A \cdot \mathbf{r}_1 = 0$.

In particular, condition 2 implies the definition of $\mathbf{v}_1^A$ as

$$\mathbf{v}_1^A := \sqrt{\frac{Gm_E}{||\mathbf{r}_1||^3}}\ \frac{1}{||\mathbf{r}_1 \times \mathbf{r}_2||}\ (\mathbf{r}_1 \times \mathbf{r}_2) \times \mathbf{r}_1. \tag{4.13}$$

Apart from that, we require all the maneuvers to be less than 1 mm/s except for $\Delta\mathbf{v}_1$ and the one needed to insert into the stable invariant manifold.

Perigee

model	Δv_1 (km/s)	Δv_2 (km/s)
CR3BP	1.53	2.89
RnBP	1.51	2.91

Apogee

model	Δv_1 (km/s)	Δv_2 (km/s)
CR3BP	0.65	3.04
RnBP	0.66	3.05

Table 4.1: Cost of the two maneuvers required to perform a transfer from a LEO to a LPO within the framework of the CR3BP Earth – Moon system and the RnBP. The corresponding orbits are displayed in Fig. 4.15.

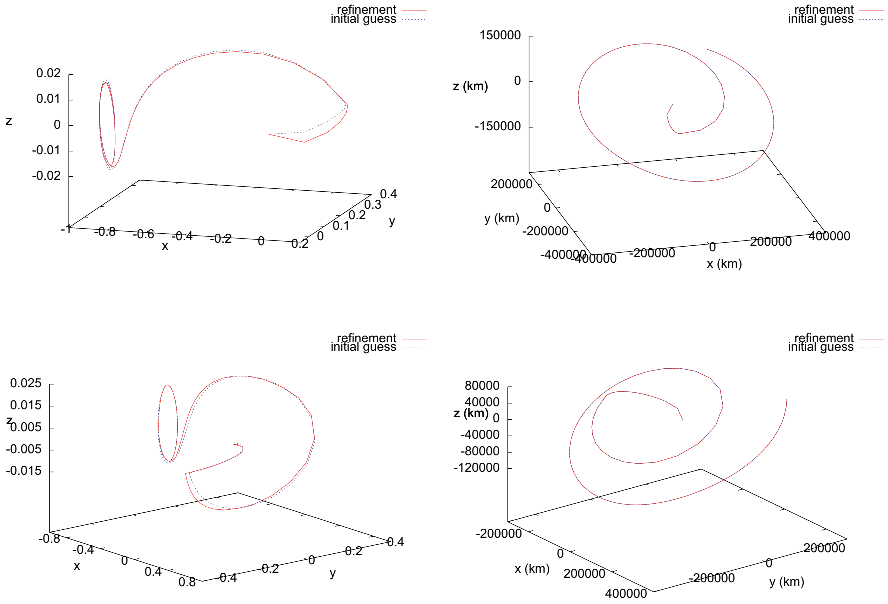

Figure 4.15: Two refinements of LEO – LPO transfers in the synodical Earth – Moon (left) and in the inertial (left) systems. On the top, the case of insertion into a perigee of the stable invariant manifold; on the bottom into one apogee. See Chapter 3.

It turns out that we can maintain the same shape of the transfer on condition that we also keep the two maneuvers. In Fig. 4.15 we show two examples, in Tab. 4.1 the corresponding costs. In both cases, the initial epoch is set at JED 2451544.5.

4.5 Comments and Possible Developments

The purpose of this chapter is the analysis and implementation of two methodologies devoted to refine trajectories obtained by means of a simplified model of forces to a more complex one. In particular, we aim at making realistic transfers and reference orbits that can be designed within the CR3BP framework.

The multiple shooting procedure is built in such a way that any discontinuity either in position and velocity is reduced up to a tolerance that depends on the problem considered. It represents a good approach whenever we do not get close to a massive body nor we deal with paths that require either specific maneuvers or properties.

The optimal control technique is more flexible, as it allows to define any constraint and boundary condition we eventually need. However, it is like a black box which gets to the refined trajectory quite slowly and it can become computationally very expensive.

In both cases, an accurate initial guess is strongly recommended.

We provide some examples in which the desired result is found by combining the two approaches. This is done in order to take advantage of the best capabilities of both and skip their characteristic drawbacks. In all the cases, we are able to reproduce and even improve the trajectories provided by the CR3BP. As it was already known, it is a good framework to start a mission design.

More examples have to be treated, not only for the types of transfer and equations of motion studied here, but also for low-thrust trajectories and vector fields including effects, which are not purely gravitational.

ASTRONOMICAL APPLICATION

LOW-ENERGY IMPACTS ON THE SURFACE OF THE MOON

5

5.1 Introduction

In the second part of this work, we show how the dynamics induced by the invariant objects of the CR3BP can help in the comprehension of Solar System natural transport phenomena. Bodies such as comets and asteroids could be able to follow trajectories lying on or inside the hyperbolic invariant manifolds associated with periodic and quasi-periodic orbits around the collinear libration points. This kind of approach has already been adopted in the past, for example to explain the behavior of comets that are temporarily captured by Jupiter (Koon et al., 2001) or the origin of well-defined galactic structures (Romero–Gómez et al., 2006).

Here, we deal with asteroidal motions that caused the formation of lunar craters. It is known that the minor bodies belonging to the Main Asteroid Belt can reach the Inner Solar System as a consequence of different types of resonance (Bottke et al., 2002): whenever they encounter a rocky planet (or satellite) they imprint its surface with information which is relevant for several branches of science.

First of all, the flux of impacts offers information on the Solar System minor bodies population. Moreover, by comparing densities of craters on different surfaces it is possible to derive the relative age of the corresponding terrains (see, for instance, Neukum, Ivanov, Hartmann (2001); Stoffler, Ryder (2001); Marchi et al. (2009)). Roughly speaking, the higher the density the older the surface. Thanks also to the space missions that provide radiometric age estimates for different regions, the geological chronology of the terrestrial planets is now becoming more and more accurate. This is especially true if we take as reference case the Moon, for which a great amount of data is now available. From investigations of this kind, a new insight on the Solar System evolution can be obtained.

The main problem in such studies lies on the fact that the crater's formation is a phenomenon not fully understood yet. There does not exist a predictive, quantitative model of crater formation, that is, a reliable methodology that can be applied to all situations. The size of the crater that forms at the end of the excavation stage depends on the asteroid's size, speed and composition, on the collision angle, on the material and structure of the surface in which the crater forms and on the surface gravity of the target (Melosh, 1999). The problem in the determination of the crater's dimension concerns with the poorness of the experimental or observational data. This difficulty is usually overcome by extrapolating beyond experimental knowledge through scaling laws.

The objective of this chapter is the analysis of some paths that impacting asteroids might have followed, but the geological background is important in order to understand which craters actually correspond to the orbits we simulate.

To be more precise, we deal with low-energy trajectories, first derived in the CR3BP framework applied to the Earth – Moon system and then analyzed accounting also for the Sun gravitational attraction by means of the BR4BP. We assume the minor bodies to have already left the Main Asteroid Belt and we consider as main entrance to the Earth – Moon neighborhood the stable invariant manifold associated with the central invariant manifold corresponding to the L_2 equilibrium point $\mathcal{W}^s(\mathcal{W}^c_{L_2})$. We look for the distribution of impacts that such orbits can create, paying attention to the fact that the Moon is locked in a 1:1 spin-orbit resonance. In particular, we wonder if, for the range of energy under consideration, the Moon acts as a shield for the Earth or if the greatest concentration of collisions still takes place on the leading side of the surface, as other authors have pointed out with different approaches. See, for example, Horedt, Neukum (1984); Morota, Furumoto (2003); Le Feuvre, Wieczorek (2005).

In our analysis, we consider different selections of initial conditions, in particular distributions which are uniform either inside the stable invariant tube or in a given level of energy.

Under the hypotheses of the CR3BP we also make an endeavor to discover any other gate (apart from $\mathcal{W}^s(\mathcal{W}^c_{L_2})$) that can produce a lunar impact within low-energy regimes. In this way, we get some evidence that low-energy ejecta originated from high-energy impacts are also responsible of the phenomenon we are considering.

We recall that while for the terrestrial planets the impact cratering epoch occurred between 4.5 and 3.85 Gy ago, for the Moon it is generally accepted the hypothesis of the Late Heavy Bombardment (LHB) or Lunar Cataclysm: the intense bombardment took place between 4 and 3.8 Gy ago and at the present day the meteoroidal flux is about 10^3 lower (Hartmann, 1986) than in those days.

In turn, to determine the role of low-energy orbits in the cratering process, we have to look upon which craters may arise from low-velocity collision; the craters we are able to observe on the Moon and the position of the Moon at the epoch of LHB. In particular, due to the small energy values we consider, the impacts can yield craters with a diameter at most 60 km wide. This value has been computed by applying the scaling laws of Melosh (1999) to the Moon's surface with an impact velocity corresponding to the escape lunar velocity (about 2.375 km/s).

5.2 Moon's Surface Features

The surface of the Moon (Bussey, Spudis, 2004; Carbognani, 2006) consists of two major types of terrain: the bright highlands, called *terrae*, and the darker, smoother plains, called *maria*. The terrae are characterized by an 'infinite' sequence of overlapping craters, created by the impact of solid bodies. As just mentioned, between 4 and 3.8 billions years ago the top few kilometers of the lunar crust have been broken up, crushed and repeatedly mixed by the force of these collisions. The maria cover roughly 16% of the surface and they are mostly situated in the hemisphere facing the Earth. They are the result of volcanic outflows and thus their dark color depends on the high iron concentration. Because of their significantly younger age (from 3.8 to 3.1 billions years), the maria have accumulated fewer craters.

As suggested by this rough analysis, the surface of the Moon was formed through a diverse set of processes. In general, the surface of celestial bodies can be shaped by four types of phenomena: external impacts, volcanic activity, tectonic activity or atmospheric degradation. On the Moon the most important effect is the first one, while the last one is essentially not present. For sake of completeness, we give a short description of all them.

5.2.1 Impact Craters

The impact craters originated from the collision of asteroids with the lunar surface.

We can identify different phases in the formation mechanism. At the beginning, we have the so-called *contact and compression* phase. Upon striking the Moon, the kinetic energy of the bolide is transferred to a shock wave which both goes down into the Moon's surface and rearward into the bolide itself. The shock wave is so powerful that most of the bolide vaporizes. The effect on the Moon is to vaporize a fraction of the external part of the surface, to melt the layers of rock below it and to fracture the surface deeper yet. The *excavation* phase begins with a release wave that develops at the edges of the impact and forms a route of escape for some of the rock involved. This escape of material produces the crater itself and the material that escapes forms the ejecta that goes outward onto the Moon's surface. At the end, in the *modification* phase the liquid material on the crater's sidewall and semi-stable rim materials slip down to the floor of the crater.

The initial crater is a circular, bowl-shaped cavity with a depth-diameter ratio between 1:4 and 1:3. This form is independent of its diameter, of the impact velocity, impact angle, gravitational acceleration and of other properties of the projectile and of the target. On the other hand, the final crater morphology is sensitive to all these conditions. The entire process of modification as a result of gravitational instability and collapse is not fully understood yet, because it is not still completely known how rocks respond to sudden rocks.

There exit different types of impact craters, whose morphological diversity is not a direct result of the crater excavation process but develops only after most of the material has been expelled from the crater. The first classification that can be done distinguishes between simple and complex craters. Simple craters (see Fig. 5.1) are circular, bowl-shaped depressions with raised rims and approximately parabolic interiors profiles. The rim–to–floor depth of them is about 1:5 of the rim–to–rim diameter. A simple crater forms by the relatively straightforward collapse of the rim of the transient crater immediately after it forms. Complex craters (see Fig. 5.2) may possess single or multiple central peaks, flat inner floors and terraced rims. Their depth increases with increasing diameter, but much more slowly than the depth of simple craters. Moreover, the central peak may break up and form an inner ring of mountains. The transition between simple and

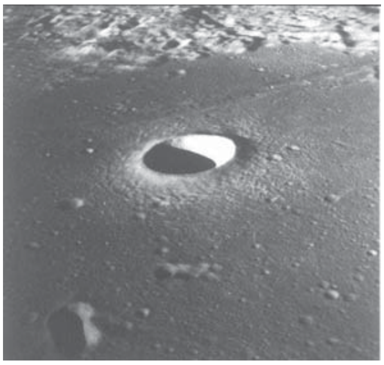

Figure 5.1: An example of simple crater: Crater Moltke.

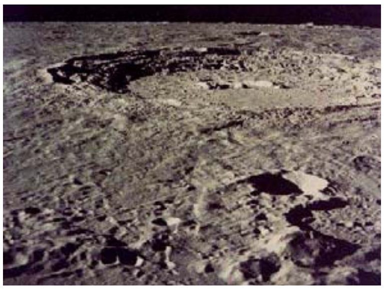

Figure 5.2: An example of complex crater: Crater Copernicus.

Figure 5.3: Mare Orientale: a multi-ring impact basin.

complex craters occurs over a narrow diameter range and seems to scale as the inverse power of the surface gravity. On the Moon this transition is determined at about 15 km. The very largest impact craters have many rings and therefore they are said multi-ring basins (see Fig. 5.3). They apparently formed by a type of collapse qualitatively different from the collapse that yields complex central peak or peak ring craters.

As a final note, some craters may be elliptical instead of circular only if a grazing impact has taken place, this is, the asteroid has collided almost tangentially with the lunar surface.

Crater's Diameter

Since our aim is to construct trajectories that have quite likely led to the formation of impact craters on the Moon, we need to know the parameters that affect the size of the craters in order to compare the craters which would originate from our computations with the craters that really exist on the Moon's surface. Thus, we provide a description of the physical properties of the known asteroids and we clarify how the final crater's diameter is usually estimated.

Asteroids are metallic, rocky bodies whose size ranges from 1000 km to that of a small stone. Most of them are concentrated in the so-called Main Asteroid Belt, a region between Mars and Jupiter from about 2 to 3.3 AU with respect to the Sun. They follow slightly elliptical orbits, revolving in the same direction as the Earth and taking from three to six years to complete a full revolution. The Near Earth Asteroids (NEAs) have orbits with a perihelion distance less than 1.3 AU and appear to be representative of most asteroid types found in the Main Asteroid Belt.

There are three main categories of asteroids according to their albedo, which is a measurement of how well the object reflects light. A white, perfectly reflecting surface has an albedo of 1; a black, perfectly absorbing surface has an albedo of 0. The first class contains the carbonaceous or C–type asteroids, which represent the 75% of all asteroids detected. They are most commonly found in the outer regions of the Main Asteroid Belt and they are very dark objects with albedos of 0.03 to 0.09. These asteroids have approximately the same chemical composition as the Sun, but lack hydrogen, helium, and other volatiles. The second class includes the silicaceous or S–type asteroids, which represent about the 17% of the known asteroids. They have fairly bright albedos ranging from 0.10 to 0.22. Moving in orbits within the inner regions of the Main Asteroid Belt, S–type asteroids are composed of rocky materials plus a small amount of nickel and iron. Finally, the metallic or M–type asteroids are mid-region Main Belt objects relatively bright, with albedos ranging from 0.10 to 0.18. M–type asteroids are mainly composed of nickel and iron.

With respect to the size of the crater, we have mentioned that it can be computed by means of scaling laws and that it depends on the asteroid's size, speed and composition, on the collision angle, on the material and structure of the surface in which the crater forms and on the surface gravity of the target. To determine the diameters we are concerned with, we use the program written by Melosh (1999). It is based on the equations of the hydrodynamics, which roughly speaking are the mass conservation equation, the

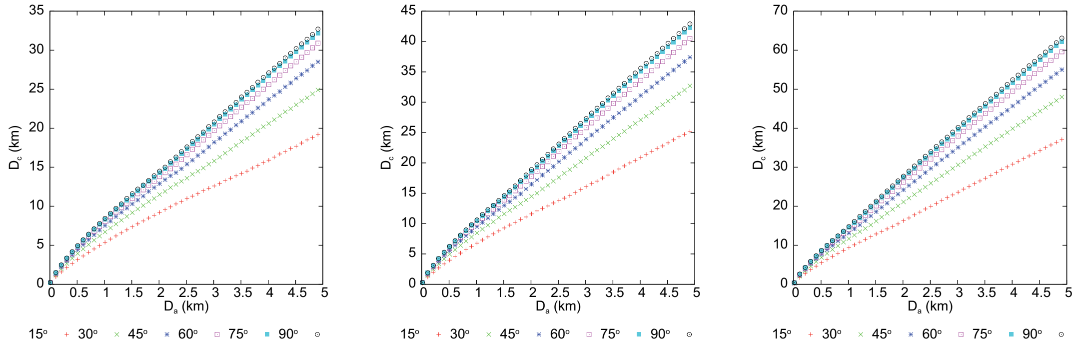

Figure 5.4: Diameter of the craters which may have formed on the surface of the Moon by low-energy impacts. On the $x-$axis the size of the bolid (km); on the $y-$axis the size of the craters (km). The three pictures refer to the three densities assumed for the bolid. Different curves refer to different impact angles.

momentum conservation equation and the energy conservation equation.

Taking the Moon as target, the characteristic parameters are the density ρ_t =3340 kg/m^3 and the surface gravity g =1.62 m/s^2. We vary the impact angle between 15° and 90° at step of 15° and the projectile's diameter between 10 and 4910 m at step of 100 m, provided the fact that most of the Main Belt Asteroids do not exceed a km in the largest direction. Moreover, hyperbolic invariant manifold trajectories guarantee the velocity of impact to be the smallest possible. Thus, we set v =2.375 km/s. Because of the above considerations on the composition of the asteroids, we perform these computations for three values of density ρ_p, that is, 1500 kg/m^3, 3000 kg/m^3 and 8000 kg/m^3, which correspond, respectively, to porous rock, dense rock and iron.

The results associated with the final crater are displayed in Fig. 5.4. It turns out that a big metallic asteroid striking the lunar surface in an almost orthogonal way can generate a crater of about 60 km in diameter, which is the largest possible in our energy level.

Catalogue of Moon's Craters

We conclude this analysis with some considerations on the craters we can see nowadays on the Moon. Ideally we would like to know the position and size of all of them, in order to have a comparison criterion for the low-energy dynamics.

There exists an official catalogue of lunar craters (Andersson, Whitaker, 1982), containing the ones which have been 'baptized' (all the features of the Moon are classified according to their name). It provides information on longitude, latitude and diameter (ranging from hundreds of m to hundreds of km) of 8649 craters. Unfortunately, this list is quite incomplete as they appear only the objects with an assigned name.

The most complete source is still represented by the images furnished by the lunar missions, such as the Clementine one (Bussey, Spudis, 2004), but it seems a hard task to obtain a comprehensive characterization of the craters formed during the LHB from

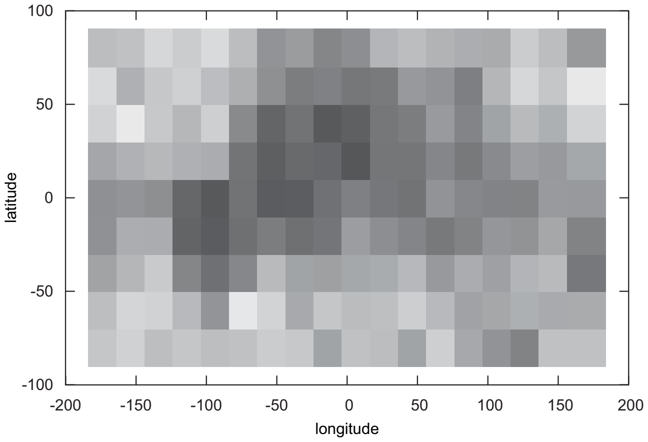

Figure 5.5: Number of craters with diameter up to 60 km per unit of area element. For this computation, we analyze the images offered by Bussey, Spudis (2004) and we discretize the Moon in elements of $20° \times 20°$ in terms of longitude and latitude. A darker shade of gray refers to a lower value of density.

them. This is due to their resolution, which is not as good as we would need on the whole Moon's surface and also due to later soil modifications. At the present day several probes (Chang'e 1, Chandrayaan-1 and SELENE) have just terminated their observations around the Moon, while LRO is still orbiting and getting valuable information. Soon we are expecting fresh high-quality data, in particular from the Japanese and the American projects.

Nevertheless we make an attempt and we analyze the pictures offered by Bussey, Spudis (2004), trying to obtain a distribution of impacts (see Fig. 5.5). To this end, first we discretize the surface of the Moon, considered as a rectangle of dimensions $[-180°, 180°] \times [-90°, 90°]$, in small squares of 20° of side. Next, in each of these squares, we compute the number of craters with diameter belonging to the desired range. Finally, this number is divided by the total number of craters belonging to the selected range and by the area of the spherical square considered. We stress that this computation has been done by hand.

We have already remarked that several authors devoted their effort to provide different types of size – frequency distributions of lunar craters (Arvidson et al., 1978; Neukum, Ivanov, Hartmann, 2001; Stoffler et al., 2006; Marchi et al., 2009). This kind of work helps to reconstruct the chronology of the Moon and the characteristics of the impactors, if the absolute age of a specific lunar region is available together with the scaling laws above introduced. Unfortunately, such wide literature is not very useful to our purpose. Instead, an analysis such that the ones performed by Morota, Furumoto (2003) and Le

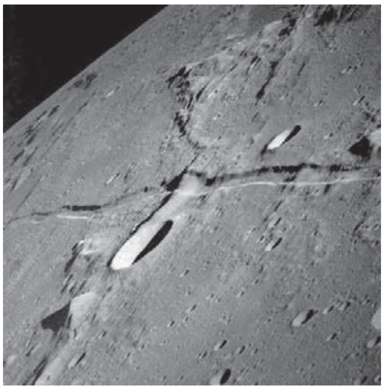

Figure 5.6: An example of graben: Rima Ariadaeus.

Feuvre (2008) could be of interest: they supply a distribution of craters as a function of the angular distance from the apex of the lunar orbital motion. The main idea behind this approach is that the motion of the satellite against the random impactors causes a relative flow of the impactors. The leading side of the satellite intercepts more impactors than the trailing side.

5.2.2 Other Processes

The next major geologic force on the Moon is the volcanism, that can be summarized as follows. Radioactive elements reheated areas of the lower crust and upper mantle, creating a series of partial melts. These melts were less dense than the surrounding rock and therefore began rising toward the surface. The eruption of lava preferentially took place in basins and it sometimes flowed long distances before finding a final position. The process of flooding resulted in large, flat lava sheets that covered the basins.

The volcanic structures on the Moon are well observable on the maria because of their lower rate of craterization. These plains are thought to be formed from the fluid material oozed out from the Moon's interior, after impacts caused by asteroids. The *Dark-Halo Craters* (DHC) are small, irregular craters, surrounded by a dark halo. They probably have a volcanic origin and they can be found on the lines of fracture characterizing several big craters on the Moon. Moreover, there exist the *Dark-Halo Impact Craters* (DHIC), impact craters characterized by a diameter of 1-3 km and surrounded by dark ejecta. This dark material came from an underlying deposit of lava. If the emission of lava took long time and the viscosity was high, the lunar volcano assumed the shape of a *dome*.

Another phenomenon that can deform the lunar surface is the tectonic activity. On the Moon the geological processes are quite easier than the terrestrial ones. We can distinguish phenomena of compression and phenomena of relaxation of the lunar crust: the *dorsals* are due to the compression, the *faults* to the extension. A pair of faults, moving in parallel directions and characterized by a lower height with respect to the surrounding area, is called *graben* (see Fig. 5.6). The dorsals are usually located in the

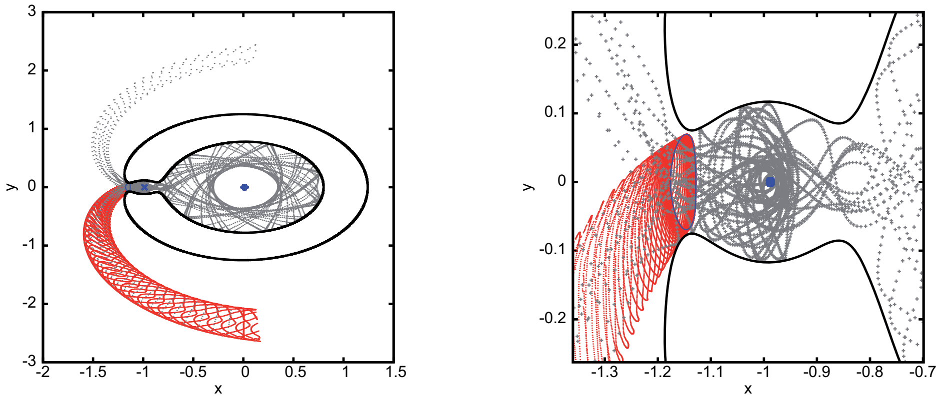

Figure 5.7: The red tube is $\mathcal{W}^s(PL_{L_2})$, the gray trajectories inside it are transit orbits, in blue we display the planar Lyapunov periodic orbit, Moon and Earth. On the right, we show a closer view of the dynamics around the Moon.

inner part of the lunar maria, while the graben are on the edges. This can be explained thinking that a mare is formed by the lava that fills the impact basin and that the weight to be supported is greater toward the center of the basin, where, as a consequence, the ground tends to fall in. On the edges the surface tends to dilate.

Finally, the lunar atmosphere is very tenuous, because of the Moon's low gravity. Light atoms escape in just a few hours, thanks to the kinetic energy obtained via solar heating. Heavier atoms are lost in few months, after being ionized by the Sun's radiation, and then carried away by the solar wind.

5.3 $\mathcal{W}^s(\mathcal{W}^c_{L_2})$ as Impact Gate

To study the role that low-energy orbits might have in the formation of lunar impact craters, we assume as main channel to get to the Moon the stable invariant manifold associated with the central invariant manifold around the L_2 point. This hypothesis is based on the fact that we admit as energy levels only those belonging to the third regime depicted in Fig. 1.3. Indeed, under either the first or the second regime, there does not exist the possibility that a particle coming from the Outer Solar System collides with the Moon. On the other side, by discarding the more energetic configurations we force the asteroids to approach the Moon before arriving to the Earth.

More precisely, we focus on the behavior of transit trajectories belonging to $\mathcal{W}^s(\mathcal{W}^c_{L_2})$ for $C_3 < C < C_2$, that is, $C \in (3.024150, 3.184163)$. In Fig. 5.7, we show the Hill's region this energy range corresponds to, the boundary of $\mathcal{W}^s(\mathcal{W}^c_{L_2})$ in red and some transit trajectories in gray. We want to figure out if there exists a specific distribution of impact brought by this kind of dynamics, without forgetting that the relative distance between Earth and Moon, say d_{EM}, could affect the total outcome, as well as the distribution of initial conditions.

First, we have to consider that the more intense lunar bombardment happened some billions years ago and that the Moon is receding from the Earth. As the rate of recession has not been constant in the past and it did not behave linearly either (see, for example, Tomasella, Marzari, Vanzani (1996); Mazumder, Arima (2005); Gordon (2008)), we take 4 values for d_{EM}: 232400, 270400, 308400, 384400 km, respectively. According to Le Feuvre (2008), they correspond approximately to 4., 3.4, 2.5 and 0 Gy ago.

With respect to the initial conditions, the computations are carried out following the considerations of Section 1.2.3, this is, for a given C we approximate $\mathcal{W}^s(\mathcal{W}^c_{L_2})$ as the product $\mathcal{W}^s(PL_{L_2}) \times \mathcal{W}^s(VL_{L_2})$. Inside such dynamical tube, we pick up initial states in 4 different ways (see below) in order to highlight any consequence that a given choice could induce.

Starting from such initial conditions we integrate the equations of motion of the CR3BP forwards in time up to a maximum allowed time for impacting onto the surface of the Moon of 60 years, provided the assumption of a no longer life in the region under consideration. If a trajectory collides with the Moon we calculate the longitude and latitude corresponding to the site of impact, together with the velocity and the angle of arrival.

The minor bodies can either:

- collide with the Moon without overcoming the L_1 border;
- collide with the Moon after overcoming the L_1 border and thus performing several loops around the Earth;
- keep wandering around the Earth inside the area delimited by the zero-velocity surface;
- escape from the Earth – Moon neighborhood just after jumping on the L_2 gate;
- exit from the Earth – Moon neighborhood after wandering for a certain interval of time around the Earth.

Note that just the first two cases cause the formation of craters of impact onto the surface of the Moon.

5.3.1 Homoclinic Connections as Re-fostering Channels

The mechanism of escaping is displayed in Fig. 5.8 and is produced by $\mathcal{W}^u(\mathcal{W}^c_{L_2})$. In this sense, it is interesting to analyze how the impact phenomena are fostered by homoclinic connections associated with L_2. They represent cycling paths, which bring the particle in and out the region demarcated by the zero-velocity surface.

Because of the procedure we adopt to determine $\mathcal{W}^s(\mathcal{W}^c_{L_2})$ and $\mathcal{W}^u(\mathcal{W}^c_{L_2})$, a homoclinic connection in a well-defined energy level is constructed by finding succeeding intersections between the stable and the unstable manifold associated with the planar Lyapunov periodic orbit and simultaneously between the stable and the unstable manifold associated with the vertical Lyapunov one.

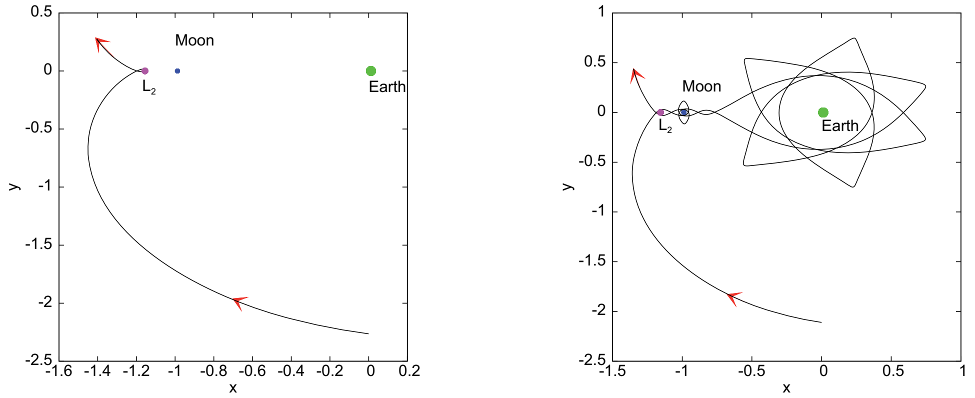

Figure 5.8: The two ways in which a particle can escape from the Earth – Moon neighborhood. On the left, the asteroid jumps on the L_2 gate; on the right, it performs some loops around the Earth and then joins $\mathcal{W}^u(\mathcal{W}^c_{L_2})$ to escape.

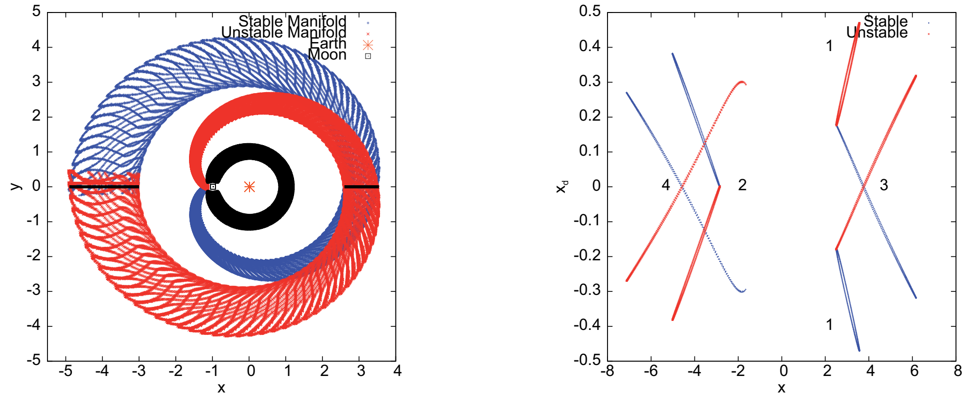

Figure 5.9: On the left, the behavior of the stable (blue) and unstable (red) invariant manifolds associated with the planar Lyapunov periodic orbit existing around L_2 for $C = 3.167456$. On the right, the projections on the $(x, \dot{x})$ plane of 4 crossings of such manifolds with $\{|x| > 1; y = 0\}$.

To find these intersections we propagate the hyperbolic invariant manifolds up to the Poincaré section $\{|x| > 1; y = 0\}$. Let $k - \mathcal{C}^{(s/u)}_{x\dot{x}}$ and $k - \mathcal{C}^{(s/u)}_{z\dot{z}}$ denote, respectively, the projection on the $(x, \dot{x})$ plane and on the $(z, \dot{z})$ plane of the $k-$intersection of the stable/unstable manifold with the Poincaré section: $k - \mathcal{C}^{(s/u)}_{x\dot{x}}$ are obtained from the hyperbolic invariant manifolds of the planar Lyapunov orbit, $k - \mathcal{C}^{(s/u)}_{z\dot{z}}$ from those of the vertical Lyapunov orbit. We say that an orbit follows a $(k, j)-$homoclinic connection if at $\{y = 0\}$ the $x - \dot{x}$ coordinates belong to the interior of $k - \mathcal{C}^{(s)}_{x\dot{x}}$ and to the interior of $j - \mathcal{C}^{(u)}_{x\dot{x}}$ and, at the same time, the $z - \dot{z}$ coordinates belong to the interior of $k - \mathcal{C}^{(s)}_{z\dot{z}}$

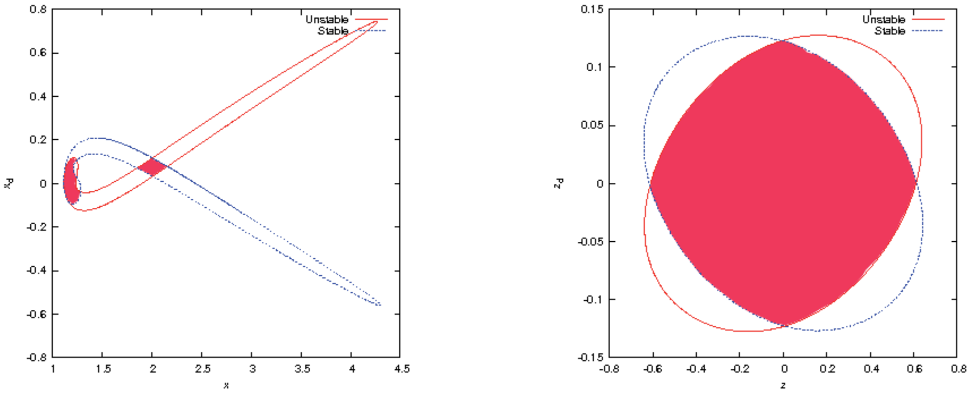

Figure 5.10: For $C = 3.050057$, the region an $(1, 1)-$homoclinic point must belong to. Left: $(x, \dot{x})$ projection. Right: $(z, \dot{z})$ projection.

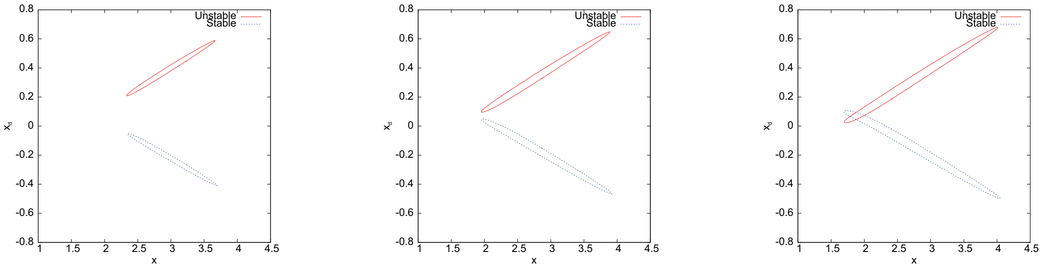

C=3.158042 C=3.131135 C=3.110873

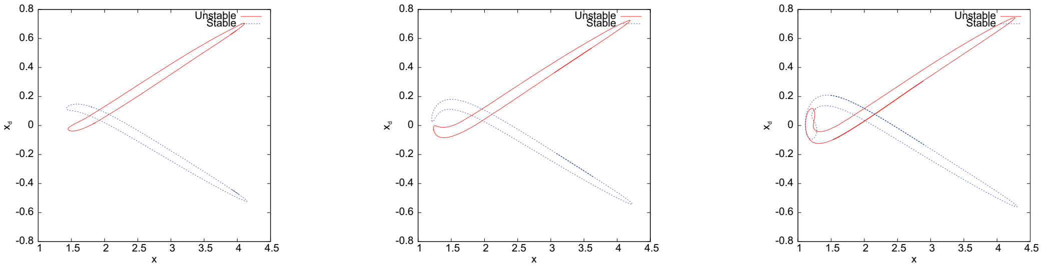

C=3.090502 C=3.070641 C=3.050057

Figure 5.11: Behavior of $1 - \mathcal{C}^{(s/u)}_{x\dot{x}}$ as a function of C. The intersection can be lost.

and to the interior of $j - \mathcal{C}^{(u)}_{z\dot{z}}$. We stress that k and j are positive integers, that can be different from each other.

In Fig. 5.9 on the left, we display the first two intersections between the stable and the unstable manifolds associated with the planar Lyapunov periodic orbit around the L_2 point at $C = 3.167456$. On the right, the 8 curves supplied in the $(x, \dot{x})$ plane by 4 crossings of such manifolds. In Fig. 5.10, the region in the $(x, \dot{x})$ and $(z, \dot{z})$ planes an

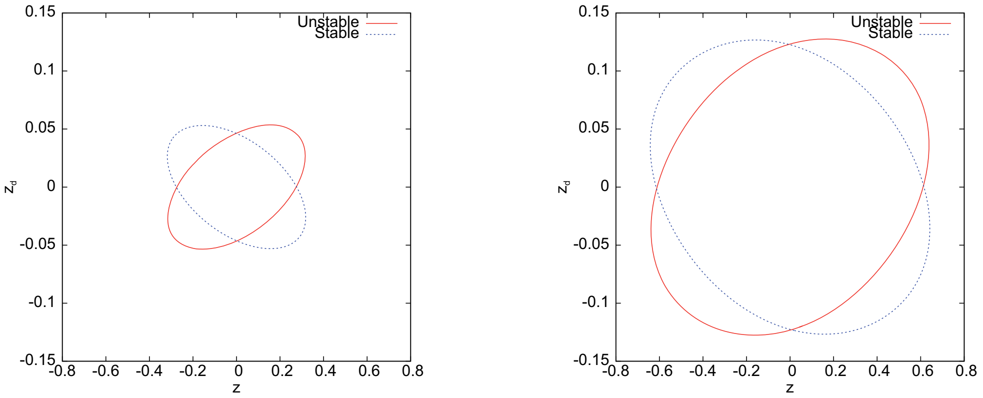

C=3.158042 C=3.050057

Figure 5.12: Behavior of $1 - \mathcal{C}_{z\dot{z}}^{(s/u)}$ for two values of C. Their interiors always overlap, the only difference between two levels of energy consisting in the size of the area covered.

$(1,1)-$homoclinic point must belong to, for $C = 3.050057$.

We notice that, while $k - \mathcal{C}_{z\dot{z}}^{(s)}$ and $j - \mathcal{C}_{z\dot{z}}^{(u)}$ always have a common interior, $k - \mathcal{C}_{x\dot{x}}^{(s)}$ and $j - \mathcal{C}_{x\dot{x}}^{(u)}$ can lose the intersection depending on the value of C. See Figs. 5.11 and 5.12.

5.4 Distributions of Initial Conditions inside $\mathcal{W}^s(\mathcal{W}^c_{L_2})$

As already explained, in a given level of energy the dynamics corresponding to $\mathcal{W}^s(\mathcal{W}^c_{L_2})$ is determined starting from the invariant stable manifolds of the planar and vertical Lyapunov periodic orbits existing around L_2. In particular, we propagate these manifolds backwards in time until they cross a given section for the first time. We consider the branch which moves away from the Moon and the plane of intersection is chosen in such a way that we can assume the asteroids to have already left the Main Asteroid Belt and to move in the Earth – Moon neighborhood.

The transit trajectories are generated by taking initial positions and velocities inside the two closed curves obtained in this way (see Figs. 1.13 and 1.14). The trajectories corresponding to such initial conditions are driven by the stable component of $\mathcal{W}^c(L_2)$, without lying on $\mathcal{W}^s(\mathcal{W}^c_{L_2})$ but staying inside this dynamical tube.

In what follows, we describe how the points at $t = 0$ are taken using four different strategies and the corresponding results we obtain. All the random variables needed are derived by means of a Knuth shuffle algorithm (Knuth, 1997) (see Appendix B). We consider 20 equally spaced energy levels C in the range $C_3 < C < C_2$. We notice that the smaller the value of C, the larger the two curves.

We devote a special effort in investigating the dynamics provided by an uniform distribution of initial conditions inside $\mathcal{W}^s(\mathcal{W}^c_{L_2})$. This means that for such transit orbits we consider the 4 different values of d_{EM} and also the possibility of homoclinic connections.

For the other three choices of initial conditions, we take $d_{EM} = 384400$ km and we do not analyze the re-fostering loops.

In all the cases, the distributions of impact on the Moon is represented by discretizing the lunar spherical surface in squares of $15^\circ \times 15^\circ$ in terms of longitude and latitude. According to the number of collisions per unit of area, normalized with respect to the total number of impacts obtained, each square can assume a different shade of gray: in the figures we show the lighter it is the greater the density of impact.

In general, we notice that to assume 60 years as maximum allowed time to impact is not a restrictive condition. In this time interval the most of the asteroids escapes from the region we are interested in and it looks like just few of them are able to go back to the Earth – Moon neighborhood later. It is reasonable to think that they remain in the Inner Solar System and occasionally are pushed towards the Earth again.

Concerning the velocity of arrival, it holds the remark done in Section 2.3.1, that is, it almost coincides with the velocity of escape of the Moon. The angle of impact can assume all the values between 0° and 90°.

5.4.1 To Be Uniform in $\mathcal{W}^s(\mathcal{W}^c_{L_2})$

The first selection of initial states we study is uniformly distributed inside each curve produced by $\mathcal{W}^s(PL_{L_2})$ and $\mathcal{W}^s(VL_{L_2})$ on the Poincaré section. This means that we want any transit trajectory inside the tube to be as probable as any other.

For each given value of C we fix $\{x = 0\}$ as the section to move from and we generate one pair of random numbers in $(y, \dot{y})$ and one in $(z, \dot{z})$; if at the same time they belong to the interior of the $(y, \dot{y})$ and $(z, \dot{z})$ curve, respectively, then we complete the set of initial conditions setting $x = 0$ and determining $\dot{x}$ from the Jacobi first integral.

For each energy level we analyze the behavior of 10^6 initial conditions.

Numerical Results

We can point out the following outcomes:

- the percentage of impacting orbits over all the initial conditions launched is at least 13%;
- the smaller d_{EM}, the higher the above percentage, see Tab. 5.1;
- the amount of particles that still wanders around the Earth inside the zone bounded by the zero-velocity surface after 60 years is 0.1%;
- most of the impacts take place within 20 years, though in the first 10 years we observe the greatest number;
- the heaviest probability of impact takes place at the apex of the lunar surface $(90^\circ W, 0^\circ)$.

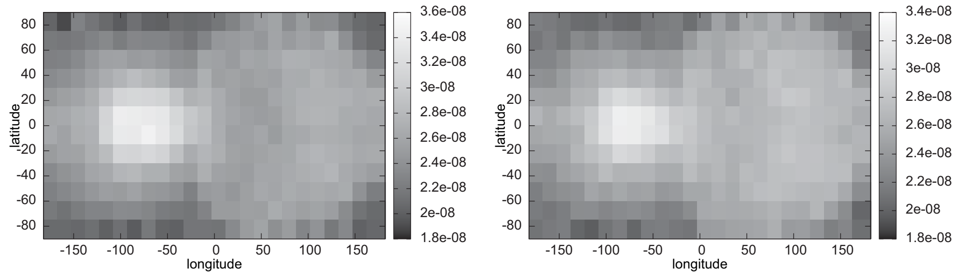

$d_{EM} = 232400$ km $d_{EM} = 270400$ km

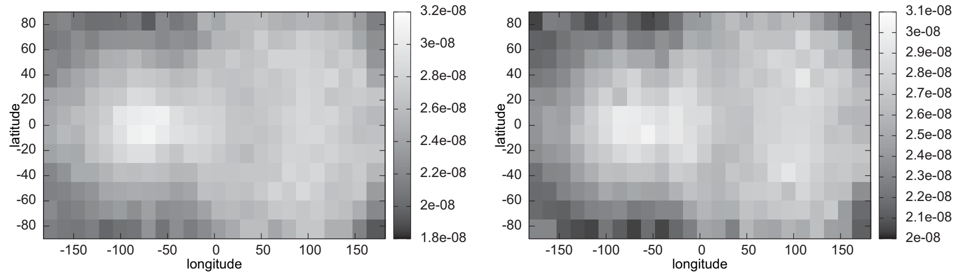

$d_{EM} = 308400$ km $d_{EM} = 384400$ km

Figure 5.13: Density of impact (number of impacts per unit of area normalized with respect to the total number of impacts obtained) computed by exploiting the CR3BP equations of motion and initial conditions uniformly distributed inside $\mathcal{W}^s(\mathcal{W}^c_{L_2})$. The surface of the Moon is discretized in squares of $15^\circ \times 15^\circ$ in terms of longitude and latitude and 4 different values for the Earth – Moon distance are considered. The color bar indicates that the lighter the shade of gray the greater the impact density.

In Fig. 5.13, we show the density of impact found for the 4 values of d_{EM} introduced previously. We remark that to consider another discretization of the lunar surface would not bring any relevant difference from a qualitatively point of view. Compare Figs. 5.13 and 5.14.

Furthermore, we compute the orbital elements associated with the osculating ellipses at $t = 0$, corresponding to colliding initial conditions. This means that every set $(x, y, z, \dot{x}, \dot{y}, \dot{z})$ producing a collision with the Moon is transformed into an inertial reference system whose origin is set at the Earth and reference plane is the Earth – Moon orbital one. Such coordinates are then turned into orbital elements (Bate, Mueller, White, 1971). In particular, we get the semi-major axis a, the eccentricity e, the inclination i, the longitude of the ascending node Ω, the argument of perigee ω and the true anomaly ν. We notice that the initial conditions are taken far enough (at least about 500000 km if we assume $d_{EM} = 384400$ km) from the Moon to be allowed to assume a

$\mathbf{d_{EM}}(km)$	**% Moon impacts**
232400	17.9
270400	15.6
308400	14.3
384400	13.2

Table 5.1: For different values of Earth – Moon distance d_{EM} the percentage of impact onto the Moon adopting the CR3BP approximation and initial states uniformly distributed inside $\mathcal{W}^s(\mathcal{W}^c_{L_2})$.

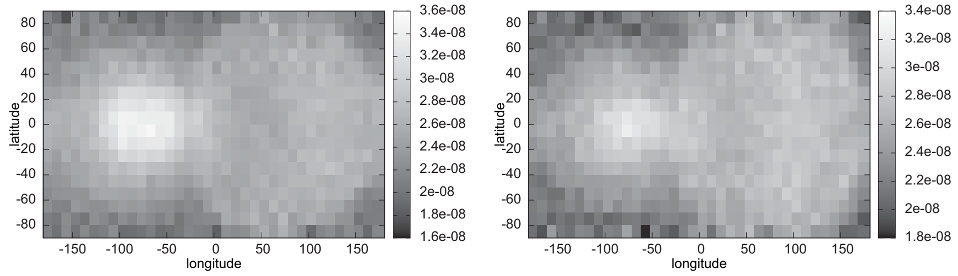

$d_{EM} = 232400$ km $d_{EM} = 308400$ km

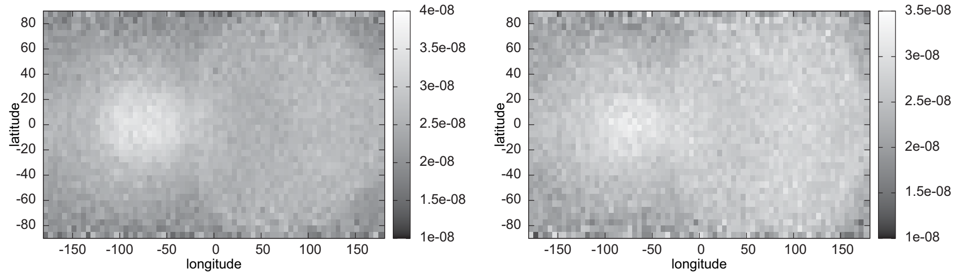

$d_{EM} = 232400$ km $d_{EM} = 308400$ km

Figure 5.14: Density of impact (number of impacts per unit of area normalized with respect to the total number of impacts obtained) computed by exploiting the CR3BP equations of motion and initial conditions uniformly distributed inside $\mathcal{W}^s(\mathcal{W}^c_{L_2})$. The surface of the Moon is discretized in squares of $10° \times 10°$ (top) and of $5° \times 5°$ (bottom) in terms of longitude and latitude. The color bar indicates that the lighter the shade of gray the greater the impact density.

2BP approximation and perform this analysis.

a (d_{EM})	**e**	**i**
$[1.5 : 3]$	$[0.4 : 0.7]$	$[1.5° : 3.5°]$

Table 5.2: For each initial condition belonging to $\mathcal{W}^s(\mathcal{W}^c_{L_2})$ and colliding with the lunar surface, we compute the orbital elements corresponding to the osculating ellipse at $t = 0$. The impact is more likely if the semi-major axis a, the eccentricity e and the inclination i with respect to the Earth – Moon orbital plane lie in the range shown here.

From these computations, it turns out that the impact is more likely if (a, e, i) belong to the intervals showed in Tab. 5.2. In Fig. 5.15, we display such probabilities for the case $d_{EM} = 384400$ km. As before, the lighter the shade of gray associated with a given $(i, a)/(i, e)$ square, the greater the probability that such orbital elements would correspond to a colliding trajectory. The probability is normalized with respect to the total number of impacts obtained.

Finally, we set $d_{EM} = 384400$ km and we propagate the transit trajectories up to 150 years, taking into account also the impacts deriving from $(1, 1)-$homoclinic connections. It turns out that the most of the particles can live inside the region bounded by the zero-velocity surface until about 100 years in the very limit situation. If they do not impact onto the Moon, they escape, but only a 0.4% of the total initial amount is able to collide with the Moon at the second entrance. In this case, they need at most 5 years more to produce a crater.

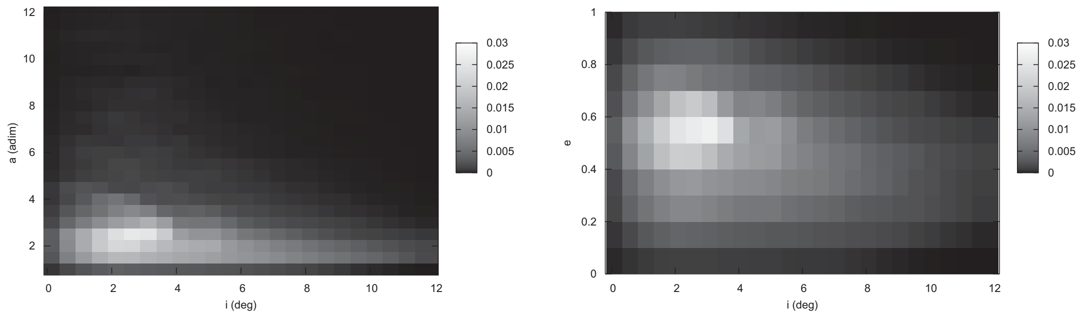

Figure 5.15: Number of impacts over the total number found considering as variables the inclination i with respect to the Earth – Moon orbital plane and the semi-major axis a; the one on the right takes as variables i and the eccentricity e. The lighter the shade of gray the greater the probability. Here, $d_{EM} = 384400$ km and the i and a ranges are discretized at steps of 0.5 degrees and d_{EM}, respectively. The e range is discretized at steps of 0.1.

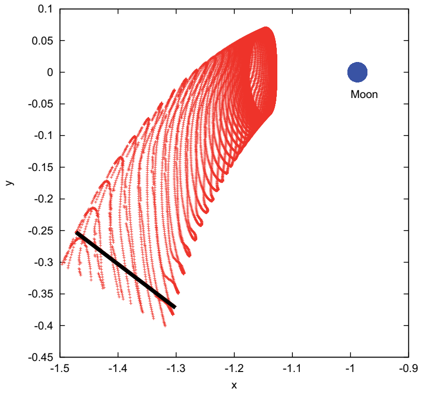

Figure 5.16: In red the branch containing the transit trajectories, in black the Poincaré section they move from, in blue the Moon.

5.4.2 To Belong to the Ecliptic

As explained in the previous section, to each initial condition we consider we can associate an orbital inclination, say i, with respect to the Earth – Moon orbital plane, provided the fact to be not too close to the Moon. First, we have to move to an inertial system of coordinates whose reference plane is the Earth – Moon orbital one and whose origin is set at the Earth (recall also Section 3.2.1) and then perform a classical transformation to orbital elements (see, for instance, Bate, Mueller, White (1971)).

We implement this procedure also to understand how orbits coming from the ecliptic can affect the distributions of impacts on the Moon. Therefore, the second set of initial conditions we propagate is selected according to i.

Now, the Poincaré section is defined as $y = 0.700207x + 1.281813$ (see Fig. 5.16) and random points are computed inside the $(x, \dot{x})$ and $(z, \dot{z})$ curves. They are accepted as initial conditions only if they correspond to a value of $i < 10°$. We recall that the ecliptic lies at about $5°14'$ with respect to the Moon's orbit.

In this case, we do not consider the same Poincaré section as in the previous section for two reasons:

- at $t = 0$ the transit orbit should lie close enough to the Earth to prevent i from changing meaningfully over the time span set;
- the initial condition should stay far enough from the Moon to permit the 2BP approximation to make sense.

Also in this exploration, for each energy level we analyze the behavior of 10^6 initial conditions.

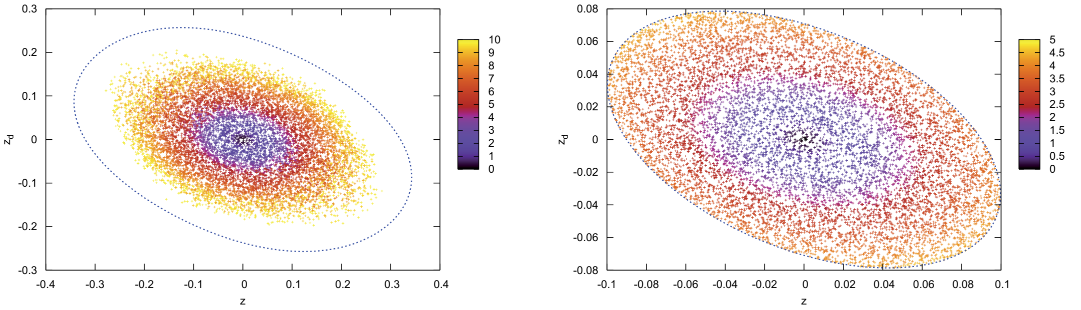

Figure 5.17: $(z, \dot{z})$ curve at the intersection with the chosen Poincaré section for $C = 3.043549$ (left) and $C = 3.171551$ (right). The points inside are initial conditions corresponding to $i \in [0°, 10°]$, as indicated by the color bar.

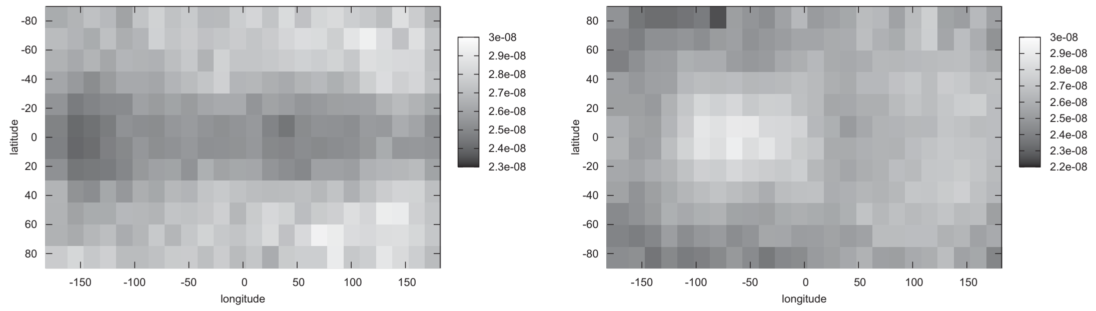

$i \in [3°, 7°]$ $i \in [0°, 10°]$

Figure 5.18: Density of impact produced by initial conditions selected according to the inclination i with respect to the Earth – Moon orbital plane of the associated osculating ellipse. The surface of the Moon is discretized in squares of $15° \times 15°$ in terms of longitude and latitude and $d_{EM} = 384400$ km. The color bar indicates that the lighter the shade of gray the greater the impact density.

Numerical Results

First of all, we notice that as long as C decreases, that is, the particle becomes more and more energetic, the range of possible i increases. In the $(z, \dot{z})$ curve, the closer the point to the center the lower the inclination (see Fig. 5.17). The choice of i results essentially in the area covered by the initial conditions inside the $(z, \dot{z})$ projection: to skip high

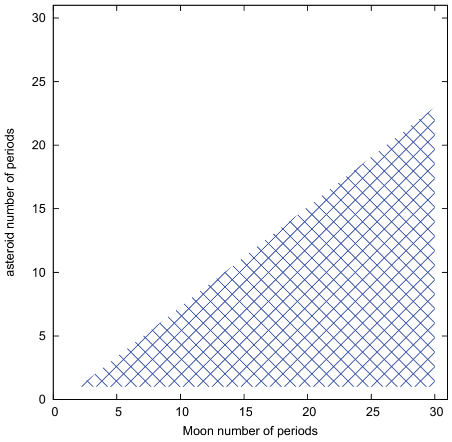

Figure 5.19: The resonances considered for the third set of initial conditions belongs to the blue triangle. As at $t = 0$ the asteroid is outside the orbit of the Moon with respect to the Earth, we always have $n_a > n_M$.

values of i means to neglect the neighborhood of the $(z, \dot{z})$ boundary, to avoid values of i close to 0° signifies to not sweep the center of the $(z, \dot{z})$ curve's interior.

As a consequence, the range of admitted i affects the distribution of lunar impacts. In Fig. 5.18, we show the density of impact obtained setting $i \in [3°, 7°]$ and $i \in [0°, 10°]$. We can notice that we obtain a lower density around 0° latitudes in the first case than in the other. Indeed, almost planar transit orbits yield impacts focused on the lunar equator. Moreover, the more comprehensive set of i maintains the apex concentration previously observed.

With respect to the percentage of impact, in both cases we obtain about 13% as before.

5.4.3 To Be in Resonance with the Moon

Another possibility we want to explore is the effect of a hypothetical resonance between the Moon and the asteroid. It is known that if two bodies experience close approaches repeatedly in time, the consequent gravitational perturbations accumulate, bringing the orbits to change drastically. On the contrary, if the resonance and the initial configuration are such that the two bodies will never encounter, then the system is somehow protected. In the Solar System, we can find several examples of both situations: just to mention some, the Kirkwood gaps, which very likely are one of the causes of the Near Earth Objects, and Pluto and Neptune, whose orbits never cross thanks to the resonance.

In our simulation, we fix the Poincaré section as above (see Fig. 5.16) and for the random points picked up inside the $(x, \dot{x})$ and $(z, \dot{z})$ curves we compute the corresponding orbital elements, as already explained. We say that an asteroid is in resonance with respect to the Moon at $t = 0$ if

$$n_a T_a = n_M T_M, \tag{5.1}$$

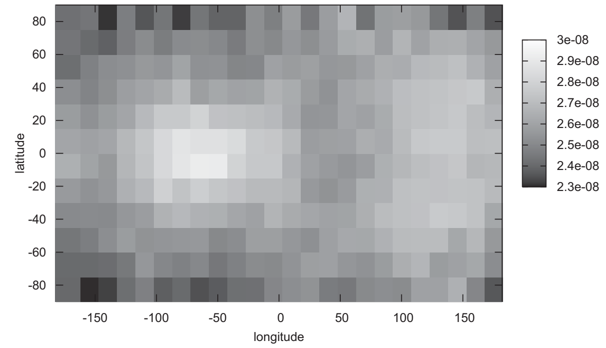

Figure 5.20: Density of impact produced by initial conditions which are in resonance with the Moon. The surface of the Moon is discretized in squares of $15^\circ \times 15^\circ$ in terms of longitude and latitude and $d_{EM} = 384400$ km. The color bar indicates that the lighter the shade of gray the greater the impact density.

where $n_a, n_M \in \mathbb{N}$ and T_a and T_M are the orbital periods of the asteroid and the Moon around the Earth. As $T_a = \sqrt{a^3 4\pi^2 \mu_2}$, where a is the semi-major axis and $\mu_2 = 1 - \mu$, we propagate forwards in time only the initial conditions which satisfy

$$a = (\mu_2)^{1/3} \Big(\frac{n_M}{n_a}\Big)^{2/3}. \qquad (5.2)$$

We notice that we always have $n_a > n_M$, as the asteroids are assumed to move outside the orbit of the Moon at least at $t = 0$. In Fig. 5.19, we show the values of n_a and n_M explored.

For this simulation, we take 10^6 initial conditions for each energy value.

Numerical Results

In the case of transit orbits which are in resonance with the Moon at $t = 0$, we get a distribution of impacts very similar to the ones found above. In Fig. 5.20, we can see it. This means that a relative Moon – asteroid configuration which repeats in time does not influence the possibility of collision, when the stable component of the central invariant manifold of a given equilibrium point controls the dynamics. We note that we take into account a quite diverse series of initial resonances and that in most of the cases they break up quite soon and transform into different ones such that $n_a < n_M$. In Fig. 5.21, we display some behaviors detected in the inertial and synodical reference systems.

With respect to the percentage of impact, also now we obtain about 13%.

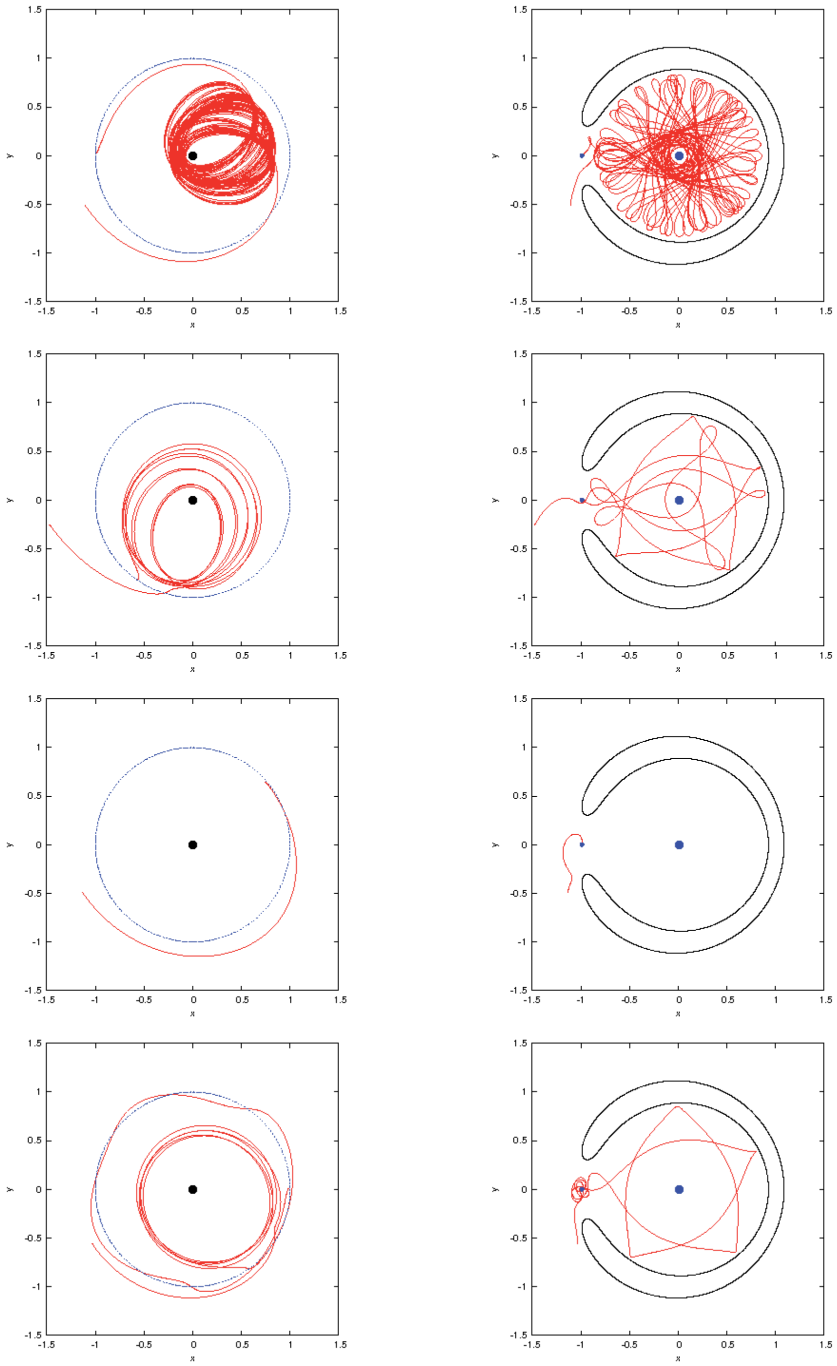

Figure 5.21: Some behaviors detected for transit orbits which are in resonance with the Moon at $t = 0$. Left: inertial reference system (in blue the Moon's orbit). Right: synodical reference system.

5.4.4 To Be Uniform in C

The fourth distribution of initial conditions is uniform in a given level of energy. Due to the existence of the Jacobi first integral of motion, there exists a 5−dimensional surface, say $\mathcal{M}$, embedded in the 6−dimensional Euclidean space we deal with.

For any well-defined C the embedding of $\mathcal{M}$ is given by the map $J : \mathbb{R}^5 \to \mathbb{R}^6$ defined as

$$\begin{aligned}
J_1(x, y, z, \dot{y}, \dot{z}) &= x, \\
J_2(x, y, z, \dot{y}, \dot{z}) &= y, \\
J_3(x, y, z, \dot{y}, \dot{z}) &= z, \\
J_4(x, y, z, \dot{y}, \dot{z}) &= x^2 + y^2 + 2\frac{1-\mu}{r_1} + 2\frac{\mu}{r_2} + \mu(1-\mu) - \dot{y}^2 - \dot{z}^2 - C, \qquad (5.3) \\
J_5(x, y, z, \dot{y}, \dot{z}) &= \dot{y}, \\
J_6(x, y, z, \dot{y}, \dot{z}) &= \dot{z}.
\end{aligned}$$

Our purpose is to set the same number of initial conditions per unit of element of volume on $\mathcal{M}$. This is,

$$\frac{\#\quad points}{element \quad of \quad volume} = constant. \qquad (5.4)$$

The constant above, say χ, is fixed and the element of volume is computed by means of the basis of vectors which generates the tangent space of $\mathcal{M}$, say $\mathcal{T}_C\mathcal{M}$.

Actually we have to calculate a 4−dimensional element of volume, because of the choice of the Poincaré section, which determines the value of x. Let $u \equiv (x, y, z, \dot{y}, \dot{z})$, then the

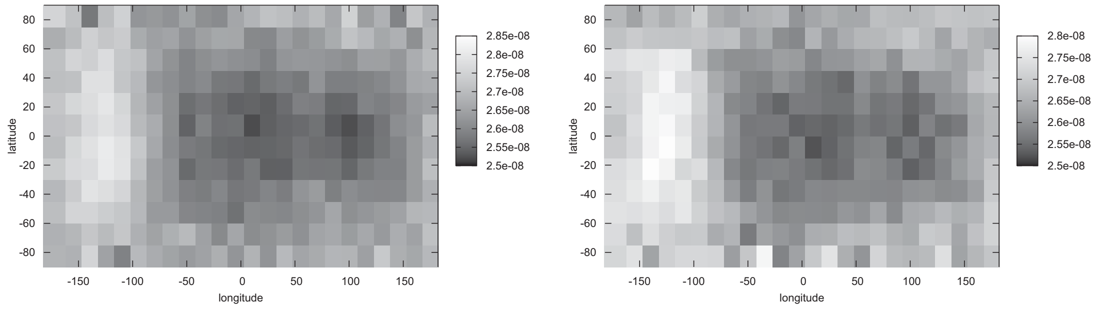

Figure 5.22: Density of impact produced by initial conditions which are uniformly distributed in a given level of energy. The two plots refer to two different meshes taken inside the $(y, \dot{y})$ and $(z, \dot{z})$ curves at $t = 0$. The surface of the Moon is discretized in squares of $15° \times 15°$ in terms of longitude and latitude and $d_{EM} = 384400$ km. The color bar indicates that the lighter the shade of gray the greater the impact density.

basis of $\mathcal{T}_C\mathcal{M}$ is given by $(\frac{\partial J_k}{\partial u_i})$, where $k = 1, \dots, 6$ and $i = 2, \dots, 5$. For a given u^*, the element of volume is the square root of the determinant of the matrix $V = [g_{ij}]$, where

$$g_{ij} = \sum_{k=1}^{6} \frac{\partial J_k}{\partial u_i} \frac{\partial J_k}{\partial u_j}(u^*), \qquad i, j = 2, \dots, 5. \tag{5.5}$$

For further details, see Do Carmo (1992).

In turn, we define the Poincaré section to be $\{x = 0\}$ and we discretize the interior of the corresponding $(y, \dot{y})$ and $(z, \dot{z})$ curves by some mesh. For each rectangle constituting the grid, we evaluate $\sqrt{det(V)}$ at the central point and we take as many initial conditions as many $\sqrt{det(V)}$ and χ suggest.

We notice that the mesh should be fine enough to allow this kind of approximation. Also, we use the same χ for each energy level considered, which means that we do not deal with the same number of initial conditions for every C, as the area to be covered by the mesh is not the same. For 20 equally spaced values of C, we consider different meshes and different values of χ in order to ensure the results to be consistent.

Numerical Results

The last type of initial conditions reserves a sort of surprise, as they do not provide the same density of impact encountered with all the previous explorations.

As said, now the total number of transit orbits simulated depends on the mesh set inside the $(y, \dot{y})$ and $(z, \dot{z})$ curves at $t = 0$. We fix as χ either 10^8 and 10^9 and we discretize the interiors of the $(y, \dot{y})$ and $(z, \dot{z})$ curves in order to have at least 10^5 initial conditions for every value of C. This means that for the smallest C considered, namely $C = 3.043549$, we performed at least 10^7 numerical integrations.

The percentage of impact oscillates between 4% and 7%, depending on the discretization considered and the collisions distribution always looks like in Fig. 5.22. It seems that the apex focusing is now shifted westward around $(130°W, 0°)$ and that many collisions on the lunar trailing side are lost.

5.5 Uniform Density of Lunar Impacts: Possible Paths

The previous investigation reveals that $\mathcal{W}^s(\mathcal{W}^c_{L_2})$ provides a non-uniform density of impact onto the surface of the Moon. The question that naturally arises is where minor bodies producing an uniform distribution of low-energy collisions would come from.

Having this purpose in mind, we start from a set of initial conditions uniformly spread out on the lunar surface, which is discretized as before in squares of 15° × 15° in terms of longitude and latitude. We notice that not only the position coordinates have to be well distributed, but also the velocity ones.

With respect to the position, if $\gamma \in [-\pi, \pi]$ is a random value of latitude, $\psi \in [0, 2\pi]$ a random value of longitude and $\rho_M = 1737.53/d_{EM}$ the adimensional radius of the Moon, then at $t = 0$ we compute

$$x = \rho_M \cos(\gamma)\cos(\psi) + \mu - 1, \qquad y = \rho_M \cos(\gamma)\sin(\psi), \qquad z = \rho_M \sin(\gamma).$$

Concerning $(\dot{x}, \dot{y}, \dot{z})$ at $t = 0$, our aim is to fulfill a constraint of uniform distribution on a semi-sphere of velocities. If $\mathbf{g} \equiv (g_x, g_y, g_z) = (x - \mu + 1, y, z)$ is the vector which is normal to the lunar surface at (x, y, z) and w and h are random values in $[0, 1]$, we implement three approaches that can be sketched as follows. In all the cases, $(\dot{x}, \dot{y}, \dot{z})$ are normalized in order to obtain the modulus of the velocity as the one satisfying the chosen C.

(1) Let $\beta \in [-\pi, \pi]$ and $\lambda \in [0, \pi]$ be random values. Then

$$\dot{x} = g_x \cos(\lambda)\cos(\beta), \qquad \dot{y} = g_y \cos(\lambda)\sin(\beta), \qquad \dot{z} = -g_z \sin(\lambda).$$

(2) Let β be a random value belonging to the interval $[-\pi, \pi]$ and $\lambda = \cos^{-1}(1 - 2w) \in [0, \pi]$. Then

$$\dot{x} = g_x \cos(\lambda)\cos(\beta), \qquad \dot{y} = g_y \cos(\lambda)\sin(\beta), \qquad \dot{z} = -g_z \sin(\lambda).$$

(3) Let γ and ψ as above, $\xi = 2w - 1$ and $\eta = 2h - 1$ such that $-1 < \xi, \eta < 1$ and $\xi^2 + \eta^2 < 1$. Then

$$\begin{aligned} \dot{x} &= (2\xi\sqrt{1 - \xi^2 - \eta^2})\cos(\gamma)\cos(\psi), \\ \dot{y} &= (2\eta\sqrt{1 - \xi^2 - \eta^2})\cos(\gamma)\sin(\psi), \\ \dot{z} &= -[1 - 2(\xi^2 + \eta^2)]\sin(\psi). \end{aligned}$$

We consider 10 values of $C_3 < C < C_2$ and we simulate the behavior of 758640 particles for each C, which means 7586400 particles in total. This value has been chosen to have an impact density of 2×10^{-2} km^{-2} for each 15° × 15° square considered on the surface of the Moon.

The numerical integration is performed backwards up to a maximum allowed time of 5 years and we pay attention on the trajectories which arrive from the $\{x = 0\}$ section mentioned before.

5.5.1 Numerical Results

The backwards simulation shows that there exist two main dynamical channels leading to a lunar collision, for the range of energy under study. In particular, uniform distributed impacts would come either from $\mathcal{W}^s(\mathcal{W}^c_{L_2})$ or from double collision orbits with the surface of the Moon.

In the former case, we note that all the orbits arriving to the Moon from $\{x = 0\}$ lie inside the $(y, \dot{y})$ and $(z, \dot{z})$ curves introduced in Section 1.2.3. This can be seen as a confirmation of the well-posed procedure adopted previously. In other words, the strategy defined to determine $\mathcal{W}^s(\mathcal{W}^c_{L_2})$ represents actually the dynamics we are looking

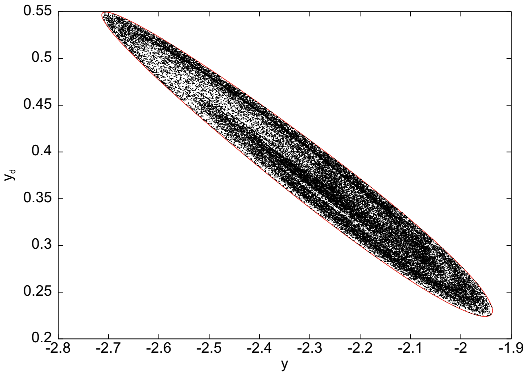

Figure 5.23: If the impact distribution on the surface of the Moon was uniform, initial conditions associated with this pattern inside the $(y, \dot{y})$ curve would collide with the Moon. We remark that the uniform distribution would not be due only to $\mathcal{W}^s(\mathcal{W}^c_{L_2})$, but also to other phenomena. See Figs. 5.24 and 5.25.

for and does not leave out any transit trajectory. The interesting point is that inside the $(y, \dot{y})$ curve we are able to note special patterns, that should be investigated with more detail (see Fig. 5.23).

The density of impact on the Moon's surface produced by $\mathcal{W}^s(\mathcal{W}^c_{L_2})$ is depicted in Fig. 5.24. The reader should be aware that we do not expect an apex concentration as before, due to the different collocation of points inside the $(y, \dot{y})$ and $(z, \dot{z})$ projections.

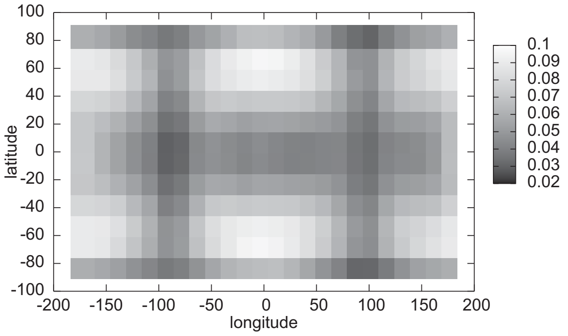

Figure 5.24: Density of impact caused by the dynamics associated with $\mathcal{W}^s(\mathcal{W}^c_{L_2})$ if the lunar craters distribution was uniform. The surface of the Moon is discretized in squares of $15^\circ \times 15^\circ$ and that the color bar refers to the number of impacts per unit of area normalized with respect to the total number of impacts found. The lighter the shade of gray the greater the impact density. The Earth – Moon distance is $d_{EM} = 384400$ km.

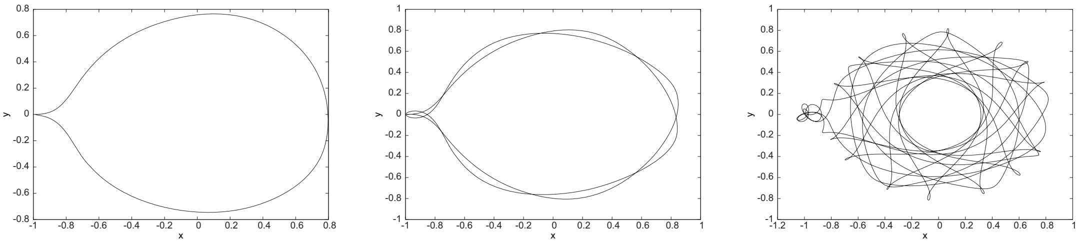

Figure 5.25: Three low-energy trajectories departing from the surface the Moon and returning there after revolving around the Earth. They have been derived assuming an uniform density of lunar impacts.

On the other hand, there exist orbits that depart from the Moon with about the lunar escape velocity and return there with the same speed (see Fig. 5.25). They can travel along different paths, turning around either the Earth or the Moon one or several times. As explanation, we can hypothesize ejecta deriving from high-energy collisions. Such effect has already been predicted by other authors (see, for instance, Gladman et al. (1996)).

5.6 On the Effect of the Sun

Now, our objective is to clarify the role of the Sun on the density of impact found previously. We focus on the most relevant concentration of impact on the leading side of the Moon obtained with uniformly distributed transit orbits and we apply the BR4BP equations of motion to the same initial conditions considered within the CR3BP framework.

Also in this case, we are able to attribute to d_{EM} some specific values, which account for the rate of recession of the Moon with respect to the Earth. We notice that a_S and ω change accordingly to d_{EM}, as we assume the adimensional set of units defined in Section 1.2.

The simulation is carried on as in Section 5.3, apart from the fact that now we have to explore the behavior corresponding to different θ_0 and that we have to take care of impacts on the surface of the Earth. Finally, the maximum time span we allow to give birth to a lunar collision is 5 years. This choice is essentially due to the increasing computational effort.

5.6.1 Numerical Results

The results can be summarized as follows:

- the percentage of impact depends on d_{EM} and on the initial phase of the Sun, θ_0: this is displayed in Tab. 5.3;

$\mathbf{d_{EM}}(km)$	θ_0	% **Moon impacts**	% **Earth impacts**
232400	36°	22.0	2.7
232400	108°	13.9	3.3
232400	180°	14.4	3.0
232400	252°	21.7	2.6
232400	324°	10.5	4.9
270400	36°	20.0	2.8
270400	108°	10.1	3.7
270400	180°	10.5	2.9
270400	252°	20.1	2.2
270400	324°	6.8	4.2
308400	36°	17.0	2.4
308400	108°	7.3	3.7
308400	180°	8.1	2.1
308400	252°	18.7	2.0
308400	324°	4.2	2.7
384400	36°	13.3	2.2
384400	108°	3.2	2.9
384400	180°	3.9	1.3
384400	252°	14.8	2.1
384400	324°	1.2	1.1

Table 5.3: Percentages of impact onto the Moon and the Earth, for different values of Earth – Moon distance d_{EM} and initial phase of the Sun θ_0.

- some trajectories collide with the Earth, the corresponding percentage is also shown in Tab. 5.3;
- looking to Tab. 5.3, it is clear that there exist values of θ_0 more favorable to yield impacts with the Moon;
- the region of highest density of impact oscillates in longitude in the range $[50°W, 100°W]$ depending on θ_0;
- it looks like the relative Earth – Moon and Earth – Moon – Sun distances, as well as the adimensional diameter of the Moon, play a significant role in what concerns with the region of heaviest lunar impact. In particular, the leading side collision concentration becomes more and more evident as d_{EM} decreases.

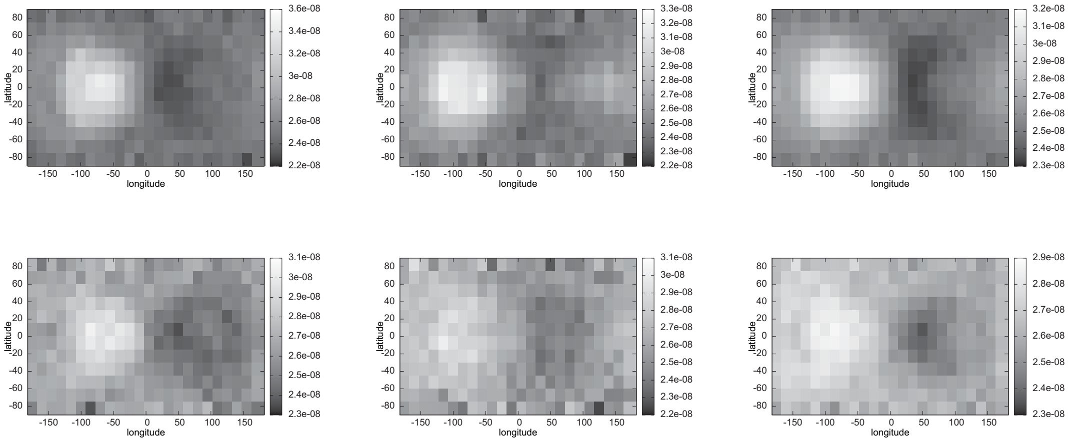

Figure 5.26: Density of impact (number of impacts per unit of area normalized with respect to the total number of impacts obtained) computed with the BR4BP equations of motion. The surface of the Moon is discretized in squares of $15° \times 15°$. The color bar indicates that the lighter the shade of gray of the square the greater the impact density. On the left, $\theta_0 = 36°$; on the middle, $\theta_0 = 180°$ and on the right we display the distribution due to all the five values (see Tab. 5.3) of θ_0 considered. On the top, $d_{EM} = 232400$ km; on the bottom, $d_{EM} = 308400$ km.

- If we compare Figs. 5.13 and 5.26 we note that the effect of the Sun reduces the number of impacts on the trailing side of the Moon, which is quite high when only Earth and Moon are considered.

In Fig. 5.26, we show the density of impact obtained when $d_{EM} = 232400$ and $d_{EM} = 308400$ km, respectively. For these plots, we consider $\theta_0 = 36°$, $\theta_0 = 180°$ and the distribution deriving from all the values of θ_0 evaluated.

To be sure the time span set is not restrictive, we perform a more extensive numerical simulation up to 60 years setting $d_{EM} = 270400$ km. The corresponding percentages of impact are displayed in Tab. 5.4: we see that they increase but not in a meaningful way.

Moreover, in order to understand how the percentage varies according to the initial phase of the Sun, we consider $d_{EM} = 270400$ km and analyze the behavior of the impacts every 12° starting from $\theta_0 = 6°$ within a time interval of 5 years. It turns out that the percentage of impact follows a periodic pattern (see Fig. 5.27), which can be recovered by a sinusoidal function.

If we plot the trajectories resulting from different values of θ_0, we can notice that the minima detected in Fig. 5.27 are the consequence of a thinning phenomenon that the dynamical tube undergoes in the proximity of the Moon. Refer to Fig. 5.28. It looks like the Sun, depending on θ_0, can be able to prevent the particle from entering into the region that is delimitated by the zero-velocity surface in the CR3BP approximation. If this happens, the asteroid keeps wandering around the Earth – Moon system, but never

t($year$)	$\theta_\mathbf{0}$	**% Moon impacts**	**% Earth impacts**
5	36°	20.0	2.8
60	36°	21.2	3.4
5	108°	10.1	3.7
60	108°	10.7	4.1
5	180°	10.5	2.9
60	180°	11.3	3.6
5	252°	20.1	2.2
60	252°	21.1	2.7
5	324°	6.8	4.2
60	324°	7.9	4.7

Table 5.4: Percentages of impact onto the Moon and the Earth, for different values of maximum time integration and initial phase of the Sun θ_0. Here $d_{EM} = 270400$ km.

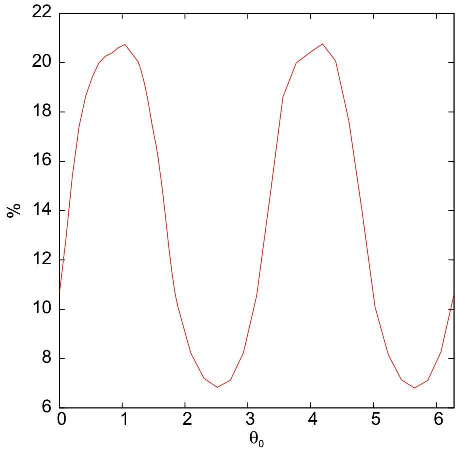

Figure 5.27: Percentage of impact as a function of θ_0, for $d_{EM} = 270400$ km.

gets into it.

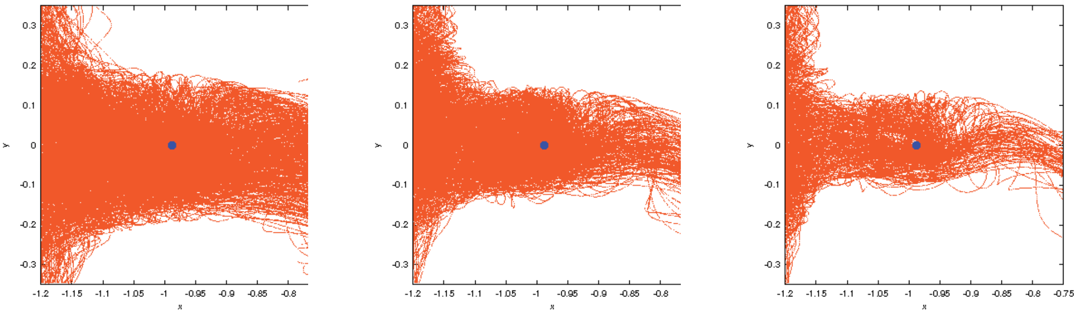

$\theta_0 = 60°$ $\theta_0 = 105°$ $\theta_0 = 150°$

Figure 5.28: Behavior of the trajectories resulting from different values of θ_0 setting $d_{EM} = 270400$ km. It looks like the width of the dynamical tube can reduce.

5.7 Comments and Possible Developments

The main purpose of this chapter is to establish a relationship between low-energy trajectories in the Earth – Moon system and lunar impact craters. This is actually a quite wide and challenging topic, which involves knowledge related to mathematics, astronomy and geology. The investigation carried out is promising from many points of view, as it indicates future developments that are worth to be considered. Several outcomes can be highlighted, even if they have to be seen as patterns that require a more robust proof: further calculations with different dynamical and astronomical models are under consideration.

To resume, we make use of the Earth – Moon dynamics pushing a massless particle under low-energy regimes and we exploit invariant objects that exist within the Circular Restricted Three – Body Problem context, in particular transit trajectories lying inside the stable invariant manifold associated with the central invariant manifold of the L_2 equilibrium point. We implement a method that allows to reproduce the behavior associated with the unstable component of any central orbit and does not need to distinguish between them. This fits with our investigation, because we are interested in minor bodies collisions that take advantage of the channels represented by the whole hyperbolic manifolds. With this approach, we perform extensive numerical simulations to determine both the lunar region of heaviest impact and the sources of a potential uniform craters distribution, taking into account diverse sets of initial conditions and values for the Earth – Moon distance.

If we analyze transit orbits which are uniformly distributed inside $\mathcal{W}^s(\mathcal{W}^c_{L_2})$, we get a confirmation that the neighborhood of the apex of the surface of the Moon is the region where most collisions take place. The phenomenon is analogous to a car running against the rain: depending on the speed, it is possible that the back window does not intercept any drop. In our case, still many collisions occur on the trailing side, although not as many as around $(90° W, 0°)$. We remark that the impact trajectories simulated reach the surface of the Moon with the lowest possible velocity: this point does not corrupt the apex concentration that other authors discovered without this restriction, neither do different values of d_{EM}. The only parameter that in reality influences the density of impact obtained is the initial inclination with respect to the Earth – Moon orbital plane of the orbits propagated.

On the other hand, if the impactors were uniformly distributed inside a specific range of energy, then a very low percentage of collisions would appear on the lunar trailing side and the major focusing would take place at a different value of longitude.

What is left regarding such simulations is to obtain a deeper understanding of the refostering cycles as a consequence of homoclinic connections and to find a link between our methodology and real observational data, concerning either the existing lunar craters and the orbital parameters at a certain epoch of a given set of Near Earth Objects. This information would affect especially the way we generate the initial conditions corresponding to transit orbits. So far, the distributions of impact derived from our explorations do not agree with the analysis carried out on the images of the Clementine mission nor with the alleged asymmetry between nearside and farside.

Apart from that, we realize that small craters can also be generated by the impact of dust arising from more energetic collisions than the ones investigated here. Such phenomenon is related to the existence of periodic orbits that cross the surface of the Moon, that is, double collision orbits. In the future, we would like to see how they are transformed by the perturbation of the Sun.

In the last part of the chapter, we look for the influence of the Sun on uniformly distributed transit orbits, by means of the Bicircular Restricted Four – Body Problem. The gravitational force exerted by the Sun seems to blur the leading side concentration experienced under the CR3BP. Changing the ratio between the Earth – Moon – Sun distance and the Earth – Moon one, we notice different patterns. Moreover, we get evidence that the position of the Sun at the initial epoch with respect to the Earth – Moon barycenter affects the distribution of impact. We notice that, according to θ_0, the percentage of impact changes in a periodic way and also the region of largest density swings in longitude.

A natural step would be to add the gravitational attractions of other planets to see their consequences on the orbits simulated. For instance, this could be done by means of a Restricted n – Body Problem, using position and velocity of the primaries given by the JPL ephemerides and taking several initial epochs to compare the whole outcome. To consider a more realistic framework is also important in order to account for the libration effects of the Moon, that can cause variations on the distribution of impact.

Finally, to apply the same kind of analysis to the terrestrial planets would be of large interest. Starting from the CR3BP approximation, we mean to study the density of impact provided by Sun – planet low-energy orbits and then to add further gravitational effects, trying to figure out the orbital elements and also the regions in the phase space which more likely lead to a collision.

Conclusions

In this dissertation, we have shown the pertinence of the Circular Restricted Three – Body Problem to the Earth – Moon system, by investigating transfers that can be accomplished either by a spacecraft and an asteroid or a comet.

The ratio between the masses of the primaries is one of the largest in the Solar System and thus it can be more reasonable than in other frameworks to take advantage of the dynamics which corresponds to the CR3BP. In particular, to account for both Earth and Moon is recommended to obtain accurate results, as we cannot neglect neither the lunar nor the terrestrial attraction on a small body moving inside the Earth gravitational sphere of influence. Also, the relevant lunar mass makes the dynamics to be very sensitive to the initial conditions.

As a first astrodynamical application, in Chapter 2 we have considered how a probe can move from the Moon to a libration point orbit either around L_1 or L_2 and vice versa. The hyperbolic invariant manifolds associated with the chosen LPO provide the whole connection, fuel is required only to depart from the lunar surface with a velocity equal to the lunar escape velocity.

Concerning the outcomes, we have identified the regions on the Moon matching with direct and non-direct transfers and characterized the lunar surface according to the number of opportunities of landing/take off. There exist different symmetries, which are proper of the CR3BP, that can be reckoned as they result into the Moon's accessible regions. In particular, between I and II class halo orbits, stable and unstable invariant manifolds and L_1 and L_2 LPOs. Besides, we have devoted a special emphasis in discovering where landing can take place tangentially and take off normally. The two situations overlap but very narrowly. If we are interested in reaching polar latitudes, we must design transfers established on a LPO with a quite high vertical amplitude. The main drawback of such lunar rescue orbits is the transfer time, at least 10 days.

As a further step, in Chapter 3 we have explained a methodology to move from a Low Earth Orbit to a L_1/L_2 Lissajous quasi-periodic orbit. In this case, the stable invariant manifold is not sufficient, but it has to be aided by an additional leg. Because of this, we deal with two maneuvers, one is needed to leave the LEO and the other to join the stable invariant manifold. The differential correction procedure implemented aims at minimizing the first Δv in such a way that it is performed on the same direction of the velocity of the circular orbit around the Earth. The magnitude of such maneuver depends on the altitude chosen for the LEO.

With respect to the second change in velocity, the results show that for a transfer to a L_1 LPO the most convenient situation takes place when the distance function between the Earth and the manifold reaches a maximum and for a L_2 transfer when we have traveled enough time on the stable invariant manifold. While in the former case the amplitude of the square Lissajous orbit affects the total cost, this does not happen for trajectories that go beyond the Moon. With our technique to move to L_2 is cheaper than to L_1, but the time of flight is too big to think to apply this kind of transfers to real situations.

In Chapter 4 we have described how trajectories computed within the CR3BP framework, such that the ones just mentioned, can be refined into a more comprehensive vector field. As a matter of fact, we have implemented a procedure established on an optimal control strategy combined with a multiple shooting method in order to attain the desired level of accuracy.

The refinement of a nominal trajectory has the objective of computing an orbit continuous both in position and velocity under well-defined equations of motion, but we can deal with situations where a natural trajectory does not exist or with transfers that require some maneuvers that can be only partially reduced. This is the main reason a multiple shooting method is not completely sufficient for our purposes and we have allowed some discontinuities in velocity for the refined trajectory under the optimal control approach.

In the examples analyzed, we have considered the Restricted n – Body Problem as new model of forces and we have described how additional requirements can be taken into account besides the difficulties we have dealt with. A more exhaustive exploitation is recommended, in particular we mean to use the whole procedure systematically for the refinement of heteroclinic connections between two coupled CR3BP to understand their role in the phase space associated with the full model. So far we have figured out that zero-cost transfers exist but with apparently strong limitations associated with the initial epoch and the cost of the matching obtained in the CR3BP context.

Moreover, we plan to cope with low-thrust transfers, for instance starting from a 2BP approximation and representing such kind of propulsion with as many as possible impulsive maneuvers in the refinement. The algorithm developed is quite general and should fit easily with different cases. Another application we might consider is a vector field with not only gravitational effects.

The last topic we have studied is the impact of minor bodies onto the surface of the Moon (Chapter 5). We are interested in low-energy trajectories computed within the approximation of the CR3BP and driven by the stable invariant manifold associated with the central invariant manifold of the L_2 equilibrium point, $\mathcal{W}^s(\mathcal{W}^c_{L_2})$. We have looked for the distribution of collisions that such dynamics provides, being aware of the complexity of the phenomenon under consideration. However, we have not faced the geological or astronomical related aspects.

We have taken into account different selections of initial conditions and values for the relative Earth – Moon distance d_{EM}, showing their consequences on the outcomes. We have seen that the heaviest probability of impact takes place at the apex of the lunar surface $(90°W, 0°)$ if the initial conditions are uniformly distributed inside $\mathcal{W}^s(\mathcal{W}^c_{L_2})$, but that the apex focusing is shifted westward around $(130°W, 0°)$ if the trajectories at the initial epoch are uniformly distributed in the level of energy considered. Also, the inclination at $t = 0$ with respect to the Earth – Moon orbital plane can cause a lost of collisions at equatorial latitudes. In general, 60 years are enough for characterizing impacts of objects in the Earth – Moon neighborhood.

The main issue to further investigate is how much homoclinic connections corresponding to L_2 represent re-fostering channels for a collision with the Moon and, consequently, the distribution of impact due to such longer trajectories.

Besides, we have added the influence of the Sun by means of the Bicircular Restricted Four – Body Problem, noting that the percentage of impact depends on d_{EM} and on the initial phase of the Sun θ_0. We have seen that the presence of the Sun is able to make the asteroid not to approach the Earth – Moon region, letting it to wander around indefinitely in time. Also, the leading side collision becomes more and more evident as d_{EM} decreases, the number of impacts on the lunar trailing side are reduced and the highest density of impact oscillates in longitude in the range $[50°W, 100°W]$ depending on θ_0.

The weakest point in such explorations concerns with the observational data, for the asteroids and the craters. In particular, the minor bodies approaching the Earth nowadays are characterized by a speed which is usually high and there is not evidence that in the past it was different. On the other hand, a realistic distribution of impact craters is very hard to obtain and thus we do not have comparative terms for our results.

However, the same procedure can be applied to different satellites with rocky surface, for instance in the Jupiter – Callisto framework. In this case, the low-energy constraint can be more probable. We plan to study this and other systems, such as Sun – Mercury, also to understand the role of the value of the mass parameter. We recall that Callisto is locked in a 1:1 spin-orbit resonance as the Moon, while Mercury in a 3:2 one.

Finally, we have simulated the lunar impacts starting from the surface of the Moon and propagating the equations of motion of the CR3BP backwards in time. We have discovered trajectories that come from the Moon itself. They can be explained in terms of ejecta deriving from high-energy collisions and they represent a more likely situation for the Earth – Moon system.

All the data associated with low-energy collisions have to be confirmed in the future by adopting as dynamical approximation the RnBP.

Variational Equations associated with the RnBP

A

If $\tilde{\mathbf{X}} \equiv (t, \mathbf{X})$, the variational equations corresponding to (4.2) can be written as

$$\dot{\Phi} = \frac{\partial f}{\partial \tilde{\mathbf{X}}} \Phi, \qquad \Phi_{t=0} = I, \tag{A.1}$$

where

$$\Phi = \begin{pmatrix} 1 & 0 & 0 & 0 & 0 & 0 & 0 \\ \frac{\partial \varphi_x}{\partial t} & \frac{\partial \varphi_x}{\partial x} & \frac{\partial \varphi_x}{\partial y} & \frac{\partial \varphi_x}{\partial x} & \frac{\partial \varphi_x}{\partial \dot{x}} & \frac{\partial \varphi_x}{\partial \dot{y}} & \frac{\partial \varphi_x}{\partial \dot{z}} \\ \frac{\partial \varphi_y}{\partial t} & \frac{\partial \varphi_y}{\partial x} & \frac{\partial \varphi_y}{\partial y} & \frac{\partial \varphi_y}{\partial x} & \frac{\partial \varphi_y}{\partial \dot{x}} & \frac{\partial \varphi_y}{\partial \dot{y}} & \frac{\partial \varphi_y}{\partial \dot{z}} \\ \frac{\partial \varphi_z}{\partial t} & \frac{\partial \varphi_z}{\partial x} & \frac{\partial \varphi_z}{\partial y} & \frac{\partial \varphi_z}{\partial x} & \frac{\partial \varphi_z}{\partial \dot{x}} & \frac{\partial \varphi_z}{\partial \dot{y}} & \frac{\partial \varphi_z}{\partial \dot{z}} \\ \frac{\partial \varphi_{\dot{x}}}{\partial t} & \frac{\partial \varphi_{\dot{x}}}{\partial x} & \frac{\partial \varphi_{\dot{x}}}{\partial y} & \frac{\partial \varphi_{\dot{x}}}{\partial x} & \frac{\partial \varphi_{\dot{x}}}{\partial \dot{x}} & \frac{\partial \varphi_{\dot{x}}}{\partial \dot{y}} & \frac{\partial \varphi_{\dot{x}}}{\partial \dot{z}} \\ \frac{\partial \varphi_{\dot{y}}}{\partial t} & \frac{\partial \varphi_{\dot{y}}}{\partial x} & \frac{\partial \varphi_{\dot{y}}}{\partial y} & \frac{\partial \varphi_{\dot{y}}}{\partial x} & \frac{\partial \varphi_{\dot{y}}}{\partial \dot{x}} & \frac{\partial \varphi_{\dot{y}}}{\partial \dot{y}} & \frac{\partial \varphi_{\dot{y}}}{\partial \dot{z}} \\ \frac{\partial \varphi_{\dot{z}}}{\partial t} & \frac{\partial \varphi_{\dot{z}}}{\partial x} & \frac{\partial \varphi_{\dot{z}}}{\partial y} & \frac{\partial \varphi_{\dot{z}}}{\partial x} & \frac{\partial \varphi_{\dot{z}}}{\partial \dot{x}} & \frac{\partial \varphi_{\dot{z}}}{\partial \dot{y}} & \frac{\partial \varphi_{\dot{z}}}{\partial \dot{z}} \end{pmatrix}, \tag{A.2}$$

and

$$\frac{\partial f}{\partial \tilde{\mathbf{X}}} = \begin{pmatrix} 0 & 0 & 0 & 0 & 0 & 0 & 0 \\ \frac{\partial f_x}{\partial t} & \frac{\partial f_x}{\partial x} & \frac{\partial f_x}{\partial y} & \frac{\partial f_x}{\partial x} & \frac{\partial f_x}{\partial \dot{x}} & \frac{\partial f_x}{\partial \dot{y}} & \frac{\partial f_x}{\partial \dot{z}} \\ \frac{\partial f_y}{\partial t} & \frac{\partial f_y}{\partial x} & \frac{\partial f_y}{\partial y} & \frac{\partial f_y}{\partial x} & \frac{\partial f_y}{\partial \dot{x}} & \frac{\partial f_y}{\partial \dot{y}} & \frac{\partial f_y}{\partial \dot{z}} \\ \frac{\partial f_z}{\partial t} & \frac{\partial f_z}{\partial x} & \frac{\partial f_z}{\partial y} & \frac{\partial f_z}{\partial x} & \frac{\partial f_z}{\partial \dot{x}} & \frac{\partial f_z}{\partial \dot{y}} & \frac{\partial f_z}{\partial \dot{z}} \\ \frac{\partial f_{\dot{x}}}{\partial t} & \frac{\partial f_{\dot{x}}}{\partial x} & \frac{\partial f_{\dot{x}}}{\partial y} & \frac{\partial f_{\dot{x}}}{\partial x} & \frac{\partial f_{\dot{x}}}{\partial \dot{x}} & \frac{\partial f_{\dot{x}}}{\partial \dot{y}} & \frac{\partial f_{\dot{x}}}{\partial \dot{z}} \\ \frac{\partial f_{\dot{y}}}{\partial t} & \frac{\partial f_{\dot{y}}}{\partial x} & \frac{\partial f_{\dot{y}}}{\partial y} & \frac{\partial f_{\dot{y}}}{\partial x} & \frac{\partial f_{\dot{y}}}{\partial \dot{x}} & \frac{\partial f_{\dot{y}}}{\partial \dot{y}} & \frac{\partial f_{\dot{y}}}{\partial \dot{z}} \\ \frac{\partial f_{\dot{z}}}{\partial t} & \frac{\partial f_{\dot{z}}}{\partial x} & \frac{\partial f_{\dot{z}}}{\partial y} & \frac{\partial f_{\dot{z}}}{\partial x} & \frac{\partial f_{\dot{z}}}{\partial \dot{x}} & \frac{\partial f_{\dot{z}}}{\partial \dot{y}} & \frac{\partial f_{\dot{z}}}{\partial \dot{z}} \end{pmatrix}.$$

As explained in Section 1.4, we adopt two different vector fields to refine transfers computed under the approximation of the CR3BP. They both describe the motion of a massless particle under the gravitational influence of Sun, Moon and the nine planets, and imply

$$\frac{\partial f}{\partial \tilde{\mathbf{X}}} = \begin{pmatrix} 0 & 0 & 0 & 0 & 0 & 0 & 0 \\ 0 & 0 & 0 & 0 & 1 & 0 & 0 \\ 0 & 0 & 0 & 0 & 0 & 1 & 0 \\ 0 & 0 & 0 & 0 & 0 & 0 & 1 \\ \frac{\partial f_{\dot{x}}}{\partial t} & \frac{\partial f_{\dot{x}}}{\partial x} & \frac{\partial f_{\dot{x}}}{\partial y} & \frac{\partial f_{\dot{x}}}{\partial z} & 0 & 0 & 0 \\ \frac{\partial f_{\dot{y}}}{\partial t} & \frac{\partial f_{\dot{y}}}{\partial x} & \frac{\partial f_{\dot{y}}}{\partial y} & \frac{\partial f_{\dot{y}}}{\partial z} & 0 & 0 & 0 \\ \frac{\partial f_{\dot{z}}}{\partial t} & \frac{\partial f_{\dot{z}}}{\partial x} & \frac{\partial f_{\dot{z}}}{\partial y} & \frac{\partial f_{\dot{z}}}{\partial z} & 0 & 0 & 0 \end{pmatrix}.$$

Therefore we have, for instance,

$$\begin{aligned} \frac{\partial \dot{\varphi}_x}{\partial t} &= \frac{\partial \varphi_{\dot{x}}}{\partial t}, \\ \frac{\partial \dot{\varphi}_x}{\partial x} &= \frac{\partial \varphi_{\dot{x}}}{\partial x}, \\ \frac{\partial \dot{\varphi}_{\dot{x}}}{\partial t} &= \frac{\partial f_{\dot{x}}}{\partial t} + \frac{\partial f_{\dot{x}}}{\partial x}\frac{\partial \varphi_x}{\partial t} + \frac{\partial f_{\dot{x}}}{\partial y}\frac{\partial \varphi_y}{\partial t} + \frac{\partial f_{\dot{x}}}{\partial z}\frac{\partial \varphi_z}{\partial t}, \\ \frac{\partial \dot{\varphi}_{\dot{x}}}{\partial x} &= \frac{\partial f_{\dot{x}}}{\partial x}\frac{\partial \varphi_x}{\partial x} + \frac{\partial f_{\dot{x}}}{\partial y}\frac{\partial \varphi_y}{\partial x} + \frac{\partial f_{\dot{x}}}{\partial z}\frac{\partial \varphi_z}{\partial x}. \end{aligned}$$

Concerning the vector field (1.15), the derivatives we look for are of the type:

$$\begin{aligned} \frac{\partial f_{\dot{x}}}{\partial t} &= \sum_{p=1}^{11} \frac{Gm_p}{r_{ip}^3}\Big(\dot{x}_p - 3(x_i - x_p)\frac{(x_i - x_p)\dot{x}_p + (y_i - y_p)\dot{y}_p + (z_i - z_p)\dot{z}_p}{r_{ip}^2}\Big), \\ \frac{\partial f_{\dot{x}}}{\partial x} &= -\sum_{p=1}^{11} \frac{Gm_p}{r_{ip}^3} + \sum_{p=1}^{11} \frac{3Gm_p(x_i - x_p)^2}{r_{ip}^5}, \\ \frac{\partial f_{\dot{x}}}{\partial y} &= \sum_{p=1}^{11} \frac{3Gm_p(x_i - x_p)(y_i - y_p)}{r_{ip}^5}, \\ \frac{\partial f_{\dot{x}}}{\partial x} &= \sum_{p=1}^{11} \frac{3Gm_p(x_i - x_p)(z_i - z_p)}{r_{ip}^5}. \end{aligned}$$

For the variational equations associated with (1.17) the only difference is that now the time-dependent terms are those corresponding to the position of each body p and also to the position and acceleration of the Earth. For instance, we have

$$\begin{aligned} \frac{\partial f_{\dot{\xi}}}{\partial t} = {} & \sum_{p=1}^{11} \frac{Gm_p}{r_{iEp}^3}\Big(\dot{x}_p - \dot{x}_E - 3(x_E - x_p + \xi_i) \\ & \frac{(x_E - x_p + \xi_i)(\dot{x}_p - \dot{x}_E) + (y_E - y_p + \eta_i)(\dot{y}_p - \dot{y}_E) + (z_E - z_p + \zeta_i)(\dot{z}_p - \dot{z}_E)}{r_{iEp}^2}\Big) \\ & -\frac{d\ddot{x}_E}{dt}. \end{aligned}$$

KNUTH SHUFFLE ALGORITHM B

In this work, to obtain a sequence of random real numbers uniformly distributed between 0 and 1 $\langle U_n \rangle$, we exploit the following linear congruential method. Let $m = 2^{31} - 1 = 2147483647$, $a = 7^5 = 16807$, $q = 127773$ and $r = 2836$, then

$$\begin{aligned} T_k &= a(X_k \text{mod } q) - r[X_k/q], \\ aX_k \text{mod } m &= \begin{cases} T_k & \text{if} \quad T_k \geq 0 \\ T_k + m & \text{if} \quad T_k < 0 \end{cases}, \\ X_{k+1} &= aX_k \text{mod } m, \\ U_{k+1} &= X_{k+1}/m. \end{aligned}$$

As a shuffle algorithm, we mean a procedure which aims at reordering a given sequence $\langle U_n \rangle$ to improve its quality. We adopt this approach:

1. we initialize an auxiliary sequence $\langle V_0, V_1, \ldots, V_p \rangle$ with the first p values of the $X-$sequence;
2. we define $Y = X_{p+1}$;
3. $j = \lfloor pY/m \rfloor$;
4. $Y = V_j$;
5. $V_j = X_{p+1}$;
6. the final output is represented by Y.

For further details, please refer to Knuth (1997).

Bibliography

Alessi E.M., Gómez G., Masdemont J.J., ‘Leaving the Moon by means of invariant manifolds of libration point orbits’, Communications in Nonlinear Science and Numerical Simulation, 14, 4153–4167, 2009.

Alessi E.M., Gómez G., Masdemont J.J., ‘Two-manoeuvres transfers between LEOs and Lissajous orbits in the Earth–Moon system’, Advances in Space Research, 45, 1276–1291, 2010a.

Alessi E.M., Gómez G., Masdemont J.J., ‘A Motivating Exploration on Lunar Craters and Low-Energy Dynamics in the Earth–Moon System’, Celestial Mechanics and Dynamical Astronomy, 107, 187–207, 2010b.

Andersson L.E., Whitaker E.A., ‘NASA Catalogue of Lunar Nomenclature’, NASA Reference Publication 1097, University of Arizona, Tucson, Arizona, 1982.

Arvidson R., Boyce J., Chapman C., Cintala M., Fulchignoni M., Moore H., Neukum G., Schultz P., Soderblom L., Strom R., Woronow A., Young R., ‘Standard Techniques for Presentation and Analysis of Crater Size-Frequency Data’, NASA Technical Memorandum 79730, 1978.

Baoyin H., McInnes C.R., ‘Trajectories to and from the Lagrange Points and the Primary Body Surfaces’, Journal of Guidance, Control, and Dynamics, 29, 998–1003, 2006.

Bate R.R., Mueller D.D., White J.E., ‘Fundamental of Astrodynamics’, Dover Publications, Inc., New York, 1971.

Bottke W.F., Morbidelli A., Jedicke R., Petit J.M., Levison H.F., Michel P., Metcalfe T.S., ‘Debiased Orbital and Absolute Magnitude Distribution of the Near-Earth Objects’, Icarus, 156, 399–433, 2002.

Bryson A.E., Ho Y.C., ‘Applied Optimal Control’, Taylor & Francis, New York, 1975.

Bussey B., Spudis P., ‘The Clementine Atlas of the Moon’, University Press, Cambridge, 2004.

Canalias E., Cobos J., Masdemont J.J., ‘Impulsive transfers between Lissajous libration point orbits’, The Journal of the Astronautical Sciences, 51, 361–390, 2003.

Canalias E., Masdemont J.J., 'Homoclinic and heteroclinic transfer trajectories between planar Lyapunov orbits in the Sun-Earth and Earth-Moon systems', Discrete and Continuous Dynamical Systems, 14, 261–279, 2006.

Canalias E., 'Contributions to Libration Orbit Mission Design using Hyperbolic Invariant Manifolds', Ph.D. Thesis, Universitat Politècnica de Catalunya, 2007.

Carbognani A., 'I crateri della Luna', Rotolito Lombarda, Milano, 2006.

Carpenter R.J., Folta D.C., Moreau M.C., Quinn D.A., 'Libration Point Navigation Concepts Supporting the Vision for Space Exploration', AIAA/AAS Astrodynamics Specialist Conference, Providence, Rhode Island, August 2004, AIAA paper 2004–4747.

Colombo G., 'The Stabilization of an Artificial Satellite at the Inferior Conjunction Point of the Earth- Moon System', Smithsonian Astrophysical Observatory Special Report, 80, 1961.

Conley C., 'Low energy transit orbits in the restricted three-body problem', SIAM Journal on Applied Mathematics, 16, 732–746, 1968.

Cronin J., Richards P.B., Russell L.H., 'Some periodic solutions of a four-body problem', Icarus, 3, 423–428, 1964.

Delshams A., Masdemont J.J., Roldán P., 'Computing the Scattering Map in the Spatial Hill's Problem', Discrete and Continuous Dynamical Systems – Series B, 10, 455–483, 2008.

Do Carmo M.P., 'Riemannian Geometry', Birkhäuser, Boston, 1992.

Farquhar R.W., 'Station-Keeping in the Vicinity of Collinear Libration Points with an Application to a Lunar Communications Problem', AAS Science and Technology Series: Space Flight Mechanics Specialist Symposium, 11, 519–535, 1966.

Gabern Guilera F., 'On the dynamics of the Trojan asteroids', Ph.D. Thesis, Universitat de Barcelona, 2003.

Gladman B.J., Burns J.A., Duncan M., Lee P., Levison H.F., 'The Exchange of Impact Ejecta Between Terrestrial Planets', Science, 271, 1387–1392, 1996.

Goldreich P., 'History of the Lunar Orbit', Reviews of Geophysics, 4, 411–439, 1966.

Gómez G., Jorba À., Masdemont J., Simó C., 'Study of the Transfer from the Earth to a Halo Orbit Around the Equilibrium Point L_1', Celestial Mechanics and Dynamical Astronomy, 56, 541–562, 1993.

Gómez G., Masdemont J., Simó C., 'Quasihalo Orbits Associated with Libration Points', The Journal of the Astronautical Sciences, 46, 135–176, 1998.

Gómez G., Llibre J., Martínez R., Simó C., 'Dynamics and Mission Design Near Libration Point Orbits – Volume 1: Fundamentals: The Case of Collinear Libration Points', World Scientific, Singapore, 2000a.

Gómez G., Jorba À., Masdemont J., Simó C., 'Dynamics and Mission Design Near Libration Point Orbits – Volume 3: Advanced Methods for Collinear Points', World Scientific, Singapore, 2000b.

Gómez G., Mondelo J.M., 'The dynamics around the collinear equilibrium points of the RTBP', Physica D, 157, 283–321, 2001.

Gómez G., Koon W.S., Lo M.W., Marsden J.E., Masdemont J., Ross S., 'Connecting Orbits and Invariant Manifolds in the Spatial Restricted Three–Body Problem', Nonlinearity, 17, 1571–1606, 2004.

Gordon D.P., 'Transfers to Earth-Moon L_2 halo orbits using lunar proximity and invariant manifold', Master of Science Thesis, Purdue University, West Lafayette, Indiana, 2008.

Hartmann W.K., 'Moon Origin: The Impact-Trigger Hypothesis' in Origin of the Moon, Ed. W.K. Hartmann - R.J. Phillips - G.J. Taylor, 579–608, 1986.

Hill K., Parker J.S., Born G.H., Lo M.W., 'Low-Cost Lunar Communication and Navigation', CCAR White Paper, 5 May 2006.

Horedt G.P., Neukum G., 'Cratering Rate over the Surface of a Synchronous Satellite', Icarus, 60, 710–717, 1984.

Howell K., Ozimek M., 'Low-Thrust Transfers in the Earth-Moon System Including Applications to Libration Point Orbits', AAS/AIAA Astrodynamics Specialists Conference, Mackinac Island, Michigan, August 2007, AAS Paper 07–343.

Jorba À., Villanueva J., 'On the Persistence of Lower Dimensional Invariant Tori under Quasiperiodic Perturbations', Journal of Nonlinear Science, 7, 427–473, 1997.

Jorba À., Ollé M., 'Invariant curves near Hamiltonian–Hopf bifurcations of four–dimensional symplectic maps', Nonlinearity, 17, 691–710, 2004.

Knuth D.E., 'The Art of Computer Programming – Volume 1', Addison – Wesley, Reading, Massachusetts, 1997.

Koon W.S., Lo M.W., Marsden J.E., Ross S.D., 'Resonance and Capture of Jupiter Comets', Celestial Mechanics and Dynamical Astronomy, 81, 27–38, 2001.

Laird C., Wäcter A., 'Introduction to Ipopt: A tutorial for downloading, installing, and using Ipopt', 2006.

Le Feuvre M., Wieczorek M.A., 'The Asymmetric Cratering History of the Moon', Lunar and Planetary Science Conference XXXVI, 2005.

Le Feuvre M., 'Modéliser le bombardement des planètes et des lunes. Application à la datation par comptage des cratères.', Ph.D. Thesis, Institut de Physique du Globe de Paris, 2008.

Llibre J., Martínez R., Simó C., 'Transversality of the Invariant Manifolds associated to the Lyapunov Family of Periodic Orbits near L_2 in the Restricted Three Body – Problem', Journal of Differential Equations, 58, 104–156, 1985.

Lo M.W., Ross S.D., 'The Lunar L_1 Gateway: Portal to the Stars and Beyond', AIAA Space Conference, Albuquerque, New Messico, USA, August 28–30, 2001.

Marchi S., Mottola S., Cremonese G., Massironi M., Martellato E., 'A new chronology for the Moon and Mercury', The Astronomical Journal, 137, 4936–4948, 2009.

Masdemont J.J., 'High Order Expansions of Invariant Manifolds of Libration Point Orbits with Applications to Mission Design', Dynamical Systems: An International Journal, 20, 59–113, 2005.

Mazumder R., Arima M., 'Tidal rhytmites and their implications', Earth-Science Reviews, 69, 79–95, 2005.

Melosh H.J., 'Impact Cratering', Oxford University Press, New York, 1999.

Morota T., Furumoto M., 'Asymmetrical Distribution of Rayed Craters on the Moon', Earth and Planetary Science Letters, 206, 315–323, 2003.

Neukum G., Ivanov B.A., Hartmann W.K., 'Cratering Records in the Inner Solar System in relation to the Lunar Reference System', Chronology and Evolution of Mars, 96, 55–86, 2001.

Parker J.S., 'Low-Energy Ballistic Lunar Transfers', Ph.D. Thesis, University of Colorado, Boulder, Colorado, 2007.

Rausch R.R., 'Earth to Halo Orbit Transfer Trajectories', Master of Science Thesis, Purdue University, Indiana, 2005.

Renk F., Hechler M., 'Exploration Missions in the Sun-Earth-Moon system: A Detailed View on Selected Transfer Problems', IAC-08-A5.3.5, 2008.

Renk F., 'Mission Analysis for Exploration Missions Utilizing Near-Earth Libration Points', Ph.D. Thesis, Institute of Space System, Universität Stuttgart, 2009.

Richardson D.L., 'A Note on Lagrangian Formulation for Motion About the Collinear Points', Celestial Mechanics and Dynamical Astronomy, 22, 231–236, 1980.

Romero–Gómez M., Masdemont J.J., Athanassoula E., García–Gómez C., 'The origin of rR_1 ring structures in barred galaxies', Astronomy & Astrophysics, 453, 39–45, 2006.

Siegel C.L., Moser J.K., 'Lectures on Celestial Mechanics', Springer–Verlag, 1971.

Simó C., 'Solución del Problema de Lambert mediante Regularización', Collectanea Matemática, XXIV, 231–247, 1973.

Simó C.,'Effective Computations in Celestial Mechanics and Astrodynamics', Ed. V.V. Rumyantsev and A.V. Karapetyan, Modern Methods of Analytical Mechanics and their Applications, CISM Courses and Lectures, Springer, 1998.

Standish E.M., Williams J.G., 'Orbital Ephemerides of the Sun, Moon, and Planets', available at `http://iau-comm4.jpl.nasa.gov/XSChap8.pdf`.

Stoffler D., Ryder G., 'Stratigraphy and Isotope Ages of Lunar Geologic Units: Chronological Standard for the Inner Solar System', Space Science Reviews, 96, 9–54, 2001.

Stoffler D., Ryder G., Ivanov B.A., Artemieva N.A., Cintala M.J., Grieve R.A., 'Cratering History and Lunar Chronology', Reviews in Mineralogy, Geochemistry, 60, 519–596, 2006.

Szebehely V., 'Theory of orbits', Academic Press, New York, 1967.

Tomasella L., Marzari F., Vanzani V., 'Evolution of the Earth obliquity after the tidal expansion of the Moon orbit', Planetary and Space Science, 44, 427–430, 1996.

Wäcter A., Biegler L., 'On the Implementation of an Interior-Point Filter Line-Search Algorithm for Large-Scale Nonlinear Programming', 2004.